Plastic deformation of self-affine rough metal surfaces under contact loading
A green's function dislocation dynamics analysis

Parayil Venugopalan, Syam

Important note
To cite this publication, please use the final published version (if applicable).
Please check the document version above.

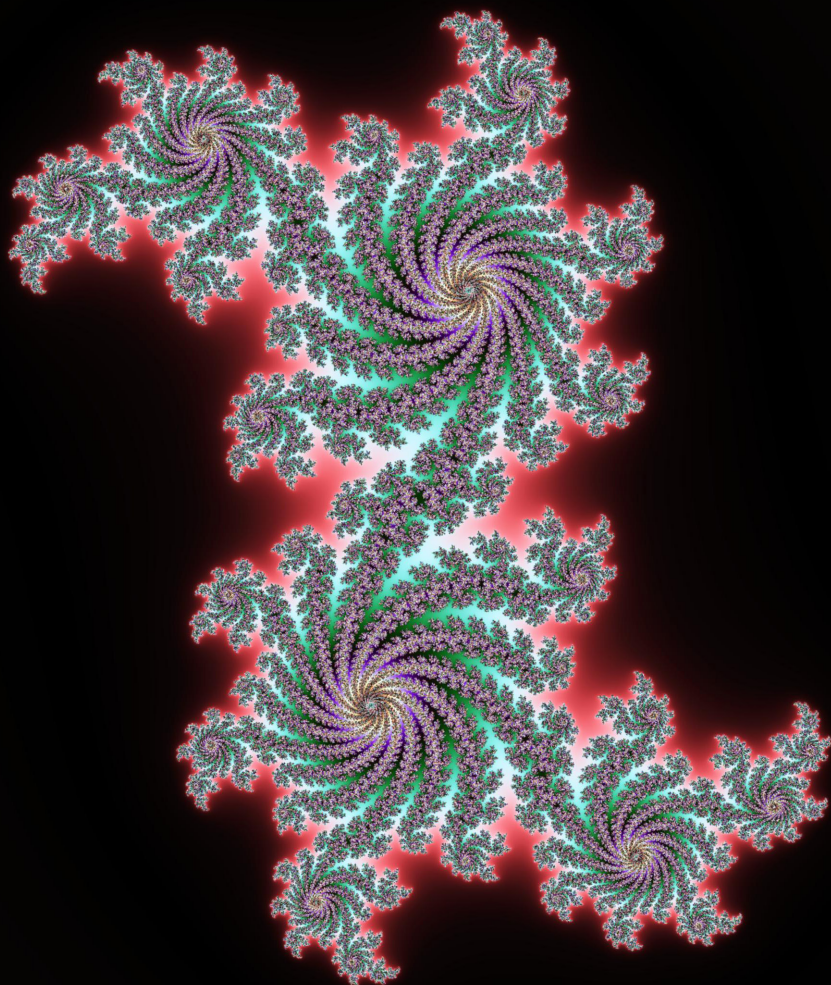# PLASTIC DEFORMATION OF SELF-AFFINE ROUGH METAL SURFACES UNDER CONTACT LOADING

Syam Parayil Venugopalan

PLASTIC DEFORMATION OF SELF-AFFINE ROUGH METAL SURFACES UNDER CONTACT LOADING

A GREEN'S FUNCTION DISLOCATION DYNAMICS ANALYSIS

PLASTIC DEFORMATION OF SELF-AFFINE ROUGH METAL SURFACES UNDER CONTACT LOADING

A GREEN'S FUNCTION DISLOCATION DYNAMICS ANALYSIS

Dissertation

for the purpose of obtaining the degree of doctor
at Delft University of Technology
by the authority of the Rector Magnificus, Prof. dr. ir. T.H.J.J. van der Hagen,
chair of the Board for Doctorates,
to be defended publicly on
Tuesday, 30 April 2019 at 12:30 hours

by

Syam PARAYIL VENUGOPALAN

Master of Mechanical Engineering,
Indian Institute of Science, Bangalore, India
born in Palakkad, Kerala, India

This dissertation has been approved by the

promotor: Prof. dr. ir. L. Nicola

Composition of the doctoral committee:

Rector Magnificus	chairperson
Prof. dr. ir. L. Nicola	Delft University of Technology

Independent members:

Prof. dr. ir. J. Sietsma	Delft University of Technology
Prof. dr. A. Almqvist	Luleå University of Technology, Sweden
Prof. dr. M. Fivel	Université Grenoble Alpes, France
Prof. dr. ir. I. M. Richardson	Delft University of Technology
Dr. ir. C. Ayas	Delft University of Technology

An electronic version of this dissertation is available at
http://repository.tudelft.nl/.

അനേക സംശയൊച്ഛേദി പരോക്ഷാർത്ഥസ്യ ദർശകം |
സർവസ്യ ലോചനം ശാസ്ത്രം യസ്യ നാസ്ത്യന്ധ ഏവ സഃ ||

अनेकसंशयोच्छेदि परोक्षार्थस्य दर्शकम्।
सर्वस्य लोचनम् शास्त्रम् यस्य नास्त्यन्ध एव सः।।

It shatters numerous uncertainties, sheds light on what is not immediately obvious |
Science is the eye of mankind; the lack of it makes one blind ||

Hitopadesham

CONTENTS

1

INTRODUCTION

1.1. GENERAL INTRODUCTION

The contact mechanics of solid bodies with rough surfaces is a topic of great practical importance in tribology, the science of friction. Energy is inevitably dissipated in the form of friction between any two surfaces that slide relatively to each other. There are several instances in daily life when friction is advantageous; for instance, the author of this thesis would be unable to type the document in the absence of friction between his fingertips and the keyboard. At the same time, friction is detrimental in several applications; for instance, in passenger cars, one-third of the fuel energy is spent to overcome friction in the engine, transmission, tires, and brakes. The direct frictional losses, excluding braking friction, are 28% of the fuel energy. According to a study by Holmberg *et. al.* (Holmberg et al., 2012), reductions in frictional losses will lead to a threefold improvement in fuel economy, as it will also reduce both the exhaust and cooling losses by the same ratio. By taking advantage of new technology for friction reduction, frictional losses could be reduced by 61% in the long term. This would amount to a worldwide economic savings of 576,000 million euros, and CO_2 emission reduction of 960 million tonnes.

With the inception of nano-technology in the 1980s, there has been a substantial interest in researching the tribological problems at the micro- and nano-scale. However, despite the success achieved in understanding and regulating the friction of macro-scale mechanical systems, there is still much room for improvement in understanding the underlying mechanism of friction for micro- and nano-scale systems. Tribological studies at these scales become important, since with diminishing system size, the surface area to volume ratio increases and hence the surface forces such as adhesion and friction become dominant over the inertial and gravitational forces (Bhushan, 2003, 2010, 2012; de Boer and Mayer, 2001; Komvopoulos, 2003; Mastrangelo, 1998; Tang and Lee, 2001; Tas et al., 1996). It is already established that the fundamental laws of friction by Amontons and Coulomb ceases to hold true at the micro- and nano-scales; studies have shown that the tribological properties such as coefficient of friction and wear rates can be different at micro- and nano-scales from macro-scales (Bhushan et al., 1995; Bhushan and Kulkarni, 1996).

One of the promising areas where tribological solutions can be of great influence is that of the Micro-Electro Mechanical Systems (MEMS) that have many micro-scale me-

chanical components such as gears, cantilevers, combs and joints. Due to relatively high surface forces interacting at the interfaces of these components, it is of great importance to clearly understand the underlying tribological mechanisms to predict and control phenomena such as friction and wear for increased durability of MEMS devices. Furthermore, specific applications where micro- and nano- scale tribological solutions are of great impact include surface micro-machining, chemical-mechanical polishing, probe-based data storage devices, nano-lithography and semiconductor processing equipment. Understanding the tribological phenomena at these length scales will ensure enhanced performance and increased durability and reliability across all spectra of micro- and nano-scale systems.

It has been observed that most man-made or natural metallic surfaces have roughness spanning several length scales, including micro- and nano- scales, and are self-affine in nature (Majumdar and Tien, 1990; Mandelbrot et al., 1984; Persson et al., 2004; Plouraboué and Boehm, 1999). If a self-affine fractal surface is magnified, with different magnifications in the perpendicular direction to the surface as compared with the parallel (in plane) direction, it looks the same; also, the statistical properties remain invariant under this scale transformation (see figure 1.1). Given the multi-scale nature of the rough metal surfaces, the true contact area is only a fraction of the apparent contact area (Bowden and Tabor, 2001). Being able to predict the size of the resulting contact spots, the true contact pressure, and the true area of contact would make it possible to control phenomena such as friction, wear, adhesion, fretting and contact fatigue. Although it is critical to keep track of the deforming asperities and the true contact area for better insight into the friction phenomenon, the contact is currently inaccessible via extant characterization techniques. This explains the wide body of analytical and numerical work on contact mechanics.
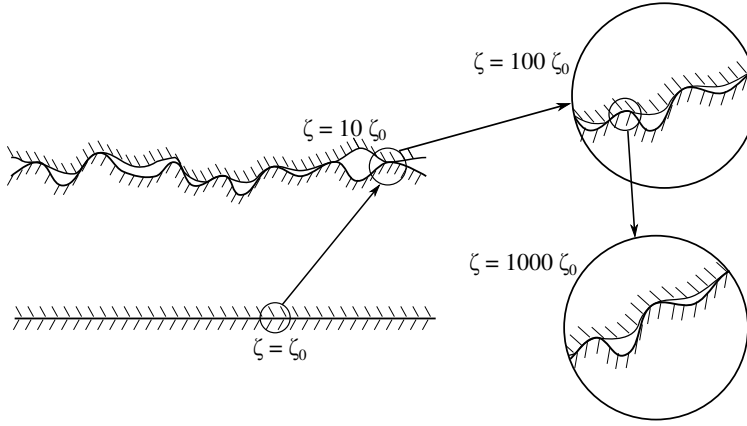
Figure 1.1: Self-affine surface: When a contact region is magnified by ζ, the smaller length scale roughness is seen and the surface appears to be "invariant".

Earlier studies of rough surfaces in contact involved qualitative description of rough surface using an ensemble of spherical bumps (Archard, 1957; Greenwood and Williamson, 1966). In the recent past, various approaches have been proposed that include analytical theories such as (Bush et al., 1975; Majumdar and Bhushan, 1991; Persson, 2001), adaptations of the Greenwood and Williamson's method to fractal surfaces (Ciavarella et al., 2000; Majumdar and Bhushan, 1991), and direct simulation of experimentally measured topographies (Hyun et al., 2004; Pei et al., 2005; Polonsky and Keer, 2000; Yastrebov et al., 2011). Out of all these methods Persson's theory stands out for its ability to predict elastic contact stress distribution in full contact and approximate the same in partial contact using a correction factor (Persson, 2006, 2001, 2008).

Numerical calculations of contact between rough surfaces have been made possible through several methods. Of particular interest are the biconjugate-gradient stabilized method (Wu, 2006), the boundary-element approach (Ilincic et al., 2011, 2009; Putignano et al., 2012a,b), the fast-Fourier-transform based boundary-value methods (FFT-BVM) (Polonsky and Keer, 2000; Stanley and Kato, 1997) and Green's function molecular dynamics (GFMD) (Campañá and Müser, 2007; Campañá et al., 2008; Dapp et al., 2014; Prodanov et al., 2014). These methods calculate the response of an elastic solid to an arbitrary boundary value problem by modeling only the surface. This makes these methods suitable for studying large systems where the surface roughness spans many orders of length scale. However, these methods are inappropriate for studying contact deformation of realistic metallic surfaces that easily undergo plastic deformation.

Friction between two self-affine metallic surfaces in contact involves energy dissipation in the form of near-surface plastic deformation (Bowden and Tabor, 1973). Even under small loads, local stresses in the contact regions easily exceed the elastic limit, and local plastic deformation takes place although nominal stresses may be within the elastic range (Dieterich and Kilgore, 1996; Dwyer-Joyce et al., 2001). Although there has been much progress in the numerical study of elasto-plastic contacts (Almqvist et al., 2007; Gao and Bower, 2006; Kogut and Etsion, 2002; Pei et al., 2005; Yastrebov et al., 2011), all these studies are based on continuum plasticity models and provide an appropriate description of contact between crystalline solids only if the contacts are larger than several micrometers.

In self-affine surfaces, the asperities span various length scales, and at the micro-scale their plastic response is size-dependent, with smaller-sized metal objects being harder to deform than large ones (Fleck et al., 1994; Greer et al., 2005; Ma and Clarke, 1995; Nicola et al., 2003, 2006; Volkert and Lilleodden, 2006). Size-dependent plasticity can be captured by discrete dislocation plasticity simulations (DDP) (van der Giessen and Needleman, 1995). The majority of discrete dislocation analyses of contact have been performed on indentation of a single crystal with a single indenter (Balint et al., 2006; Widjaja et al., 2007) or a periodic array of flat indenters (Nicola et al., 2007, 2008). This method has also been used for the analysis of self-affine surfaces in contact, accounting for multi-scale asperity interaction in semi-infinite bodies (Yin and Komvopoulos, 2012) where each micro-contact was assumed to be Hertzian. It has to be noted that, so far, only simulations for very simple surface geometries have been carried out using DDP (Song et al., 2017; Sun et al., 2012; Yin and Komvopoulos, 2012), and that the study of realistic surface geometries is limited due to the computational bottleneck of accurately modeling the roughness. Consequently, to date, no studies of rough surface contact appear to have been disseminated, in which (size-dependent) plasticity and long-range elasticity are both accurately modeled for the contact deformation of self-affine asperities.

The aim of this thesis is to develop a computationally efficient method of analyzing size-dependent plastic behavior during contact of self-affine surfaces. For contact involving micro-scale asperities, it is expected to display size-dependent behavior, but it is difficult to estimate apriori how this behavior will affect the evolution of contact pres-

sure, contact area and interfacial separation. These issues will be the focal point of this thesis. To this end, we introduce a new computationally efficient method that we name Green's function dislocation dynamics (GFDD) (Venugopalan et al., 2017a). It combines the accurate description of plasticity offered by the traditional discrete dislocation plasticity simulations (van der Giessen and Needleman, 1995) with the fast-converging elastic solution offered by Green's function molecular dynamics (Prodanov et al., 2014; Venugopalan et al., 2017b). GFDD will be used to study self-affine indentation of a plastic metal crystal keeping track of the contact area, contact pressure and hardness, gap profile and subsurface stresses, while the roughness of the indenter is changed. One of the immediate implication of studying self-affine indentation using GFDD is its ability to capture size-dependent yield stress. This quantity can be used as an input to the Persson's theory after few modifications to predict the surface observables at much reduced computational cost.

An improved understanding of the size-dependent plastic deformation of self-affine surfaces will pave the way to comprehending the contact and friction behavior of real surfaces.

1.2. OUTLINE OF THESIS

The thesis consists of a general introduction and four chapters, organized as follows:

In Chapter 2, the Green's function molecular dynamics (GFMD) method for the simulation of incompressible solids under normal loading is extended to apply to finite solids with generic Poisson's ratio and boundary conditions. Moreover, the body fields are computed analytically from the tractions and/or surface displacements. This extension allows the GFMD technique to provide the same information that can be obtained through the FEM, but with a significant reduction in the simulation time. An interesting application for the GFMD method, in virtue of the extensions presented in this chapter is the replacement of the finite element method in discrete dislocation plasticity simulations of contact. This succeeds to significantly increase the time efficiency of the discrete dislocation plasticity calculations by extending the applicability of such models to bodies of larger size, and with a realistic surface profile as will be explained in Chapter 3.

In Chapter 3, I present the new method named Green's function dislocation dynamics (GFDD). It combines the accurate description of plasticity offered by discrete disloca-

tion plasticity with the fast elastic solution obtained using the modified Green's function molecular dynamics. I demonstrate that my method captures plasticity quantitatively from single to many dislocations and that it scales more favorably with system size than conventional methods. I also derive the relevant Green's functions for elastic slabs of finite width, allowing arbitrary boundary conditions on the top and bottom surface to be simulated. The results obtained using GFDD are compared with conventional DDP for a benchmark problem: periodic indentation of a single crystal by flat punches. The new GFDD model is shown to have various advantages compared to classical DDP. First, it is faster and second, it opened up the possibility of studying realistic rough surfaces that requires surface discretizations of several orders higher. This is demonstrated in Chapter 4.

In Chapter 4, I exploit the power of Green's function dislocation dynamics to study the contact deformation of self-affine surfaces. GFDD is used to demonstrate the size-dependent plastic deformation of the self-affine asperities in contact, keeping track of the evolution of contact area, contact pressure, contact traction distribution, gap profile and subsurface stresses. Results indicate that plastic deformation is size dependent, and therefore scaling of observables should not be performed when studying contact between plastically deforming bodies. Also, contact hardness is much larger than in classical plasticity studies, is found to increase with decreasing fractal discretization. I also show that below a given threshold value for the small wavelength, hardness as well as nominal contact pressure saturate to a constant value with the fragmented contact patches acting as a 'super-contact' of constant length.

In Chaper 5, Persson's theory for self-affine elastic contacts is shown to have good agreement with GFMD simulations. The theory that has been extended for plastic contacts is also compared with GFDD simulations. Results show that the area-to-load curves obtained by theory and simulations are in good agreement when the indenter has a very small rms height. For larger rms heights, which are more realistic for metal surfaces, I show that the agreement is no longer good, unless one uses the yield strength obtained through the dislocation dynamics simulations, which is rms height and resolution dependent. I also show that a modification of this type, i.e. the use of a yield strength dependent on size, does however not lead to agreement between the probability distributions of contact stress, which are broader in the simulations than in the theory. A

possible reason is that the theory only accounts for elastically perfectly plastic bodies and therefore neglects strain hardening.

REFERENCES

Almqvist, A., Sahlin, F., Larsson, R., Glavatskih, S., 2007. On the dry elasto-plastic contact of nominally flat surfaces. Tribology International 40 (4), 574 – 579, nORDTRIB 2004.

Archard, J. F., 1957. Elastic deformation and the laws of friction. Proceedings of the Royal Society of London A: Mathematical, Physical and Engineering Sciences 243 (1233), 190–205.

Balint, D., Deshpande, V., Needleman, A., der Giessen, E. V., 2006. Discrete dislocation plasticity analysis of the wedge indentation of films. Journal of the Mechanics and Physics of Solids 54 (11), 2281 – 2303.

Bhushan, B., 2003. Adhesion and stiction: Mechanisms, measurement techniques, and methods for reduction. Journal of Vacuum Science & Technology B: Microelectronics and Nanometer Structures Processing, Measurement, and Phenomena 21 (6), 2262–2296.

Bhushan, B., 2010. Springer Handbook of Nanotechnology. Springer Berlin Heidelberg.

Bhushan, B., 2012. Tribology Issues and Opportunities in MEMS: Proceedings of the NSF/AFOSR/ASME Workshop on Tribology Issues and Opportunities in MEMS held in Columbus, Ohio, U.S.A., 9–11 November 1997. Springer Netherlands.

Bhushan, B., Israelachvili, J. N., Landman, U., 1995. Nanotribology: friction, wear and lubrication at the atomic scale. Nature 374, 607–616.

Bhushan, B., Kulkarni, A. V., 1996. Effect of normal load on microscale friction measurements. Thin Solid Films 278 (1), 49 – 56.

Bowden, F., Tabor, D., 1973. Friction: An Introduction to Tribology. Science study series. R.E. Krieger Publishing Company.

Bowden, F., Tabor, D., 2001. The Friction and Lubrication of Solids. No. v. 1 in Oxford Classic Texts in the Ph. Clarendon Press.

Bush, A., Gibson, R., Thomas, T., 1975. The elastic contact of a rough surface. Wear 35 (1), 87 – 111.

Campañá, C., Müser, M. H., 2007. Contact mechanics of real vs. randomly rough surfaces: A green's function molecular dynamics study. EPL (Europhysics Letters) 77 (3), 38005.

Campañá, C., Müser, M. H., Robbins, M. O., 2008. Elastic contact between self-affine surfaces: comparison of numerical stress and contact correlation functions with analytic predictions. Journal of Physics: Condensed Matter 20 (35), 354013.

Ciavarella, M., Demelio, G., Barber, J., Jang, Y. H., 2000. Linear elastic contact of the weierstrass profile. In: Proceedings of the Royal Society of London A: Mathematical, Physical and Engineering Sciences. Vol. 456. The Royal Society, pp. 387–405.

Dapp, W., Prodanov, N., Müser, M., 2014. Systematic analysis of persson's contact mechanics theory of randomly rough elasticsurfaces. Journal of Physics Condensed Matter 26 (35).

de Boer, M., Mayer, T., 2001. Tribology of mems. MRS Bulletin 26 (4), 302–304.

Dieterich, J., Kilgore, B., 1996. Imaging surface contacts: Power law contact distributions and contact stresses in quartz, calcite, glass and acrylic plastic. Tectonophysics 256 (1-4 SPEC. ISS.), 219–239.

Dwyer-Joyce, R., Drinkwater, B., Quinn, A., 2001. The use of ultrasound in the investigation of rough surface interfaces. Journal of Tribology 123 (1), 8–16.

Fleck, N., Muller, G., Ashby, M., Hutchinson, J., 1994. Strain gradient plasticity: Theory and experiment. Acta Metallurgica et Materialia 42 (2), 475 – 487.

Gao, Y.-F., Bower, A., 2006. Elastic–plastic contact of a rough surface with weierstrass profile. Proceedings of the Royal Society of London A: Mathematical, Physical and Engineering Sciences 462 (2065), 319–348.

Greenwood, J. A., Williamson, J. B. P., 1966. Contact of nominally flat surfaces. Proceedings of the Royal Society of London A: Mathematical, Physical and Engineering Sciences A295 (300).

Greer, J. R., Oliver, W. C., Nix, W. D., 2005. Size dependence of mechanical properties of gold at the micron scale in the absence of strain gradients. Acta Materialia 53 (6), 1821 – 1830.

Holmberg, K., Andersson, P., Erdemir, A., 2012. Global energy consumption due to friction in passenger cars. Tribology International 47 (Supplement C), 221 – 234.

Hyun, S., Pel, L., Molinari, J., Robbins, M., 2004. Finite-element analysis of contact between elastic self-affine surfaces. Physical Review E - Statistical, Nonlinear, and Soft Matter Physics 70 (2 2), 026117–1–026117–12.

Ilincic, S., Tungkunagorn, N., Vernes, A., Vorlaufer, G., Fotiu, P., Franek, F., 2011. Finite and boundary element method contact mechanics on rough, artificial hip joints. Proceedings of the Institution of Mechanical Engineers, Part J: Journal of Engineering Tribology 225 (11), 1081–1091.

Ilincic, S., Vorlaufer, G., Fotiu, P., Vernes, A., Franek, F., 2009. Combined finite element-boundary element method modelling of elastic multi-asperity contacts. Proceedings of the Institution of Mechanical Engineers, Part J: Journal of Engineering Tribology 223 (5), 767–776.

Kogut, L., Etsion, I., 2002. Elastic-plastic contact analysis of a sphere and a rigid flat. Journal of Applied Mechanics 69, 657.

Komvopoulos, K., 2003. Adhesion and friction forces in microelectromechanical systems: mechanisms, measurement, surface modification techniques, and adhesion theory. Journal of Adhesion Science and Technology 17 (4), 477–517.

Ma, Q., Clarke, D. R., Apr. 1995. Size dependent hardness of silver single crystals. Journal of Materials Research 10, 853–863.

Majumdar, A., Bhushan, B., 1991. Fractal model of elastic-plastic contact between rough surfaces. Journal of Tribology 113, 1–11.

Majumdar, A., Tien, C., 1990. Fractal characterization and simulation of rough surfaces. Wear 136 (2), 313–327.

Mandelbrot, B. B., Passoja, D. E., Paullay, A. J., 1984. Fractal character of fracture surfaces of metals. Nature Publishing Group.

Mastrangelo, C. H., 1998. Surface Force Induced Failures in Microelectromechanical Systems. Springer Netherlands, pp. 367–395.

Nicola, L., Bower, A., Kim, K.-S., Needleman, A., Van der Giessen, E., 2007. Surface versus bulk nucleation of dislocations during contact. Journal of the Mechanics and Physics of Solids 55 (6), 1120–1144.

Nicola, L., Bower, A., Kim, K.-S., Needleman, A., Van Der Giessen, E., 2008. Multi-asperity contact: A comparison between discrete dislocation and crystal plasticity predictions. Philosophical Magazine 88 (30-32), 3713–3729.

Nicola, L., der Giessen, E. V., Needleman, A., 2003. Discrete dislocation analysis of size effects in thin films. Journal of Applied Physics 93 (10), 5920–5928.

Nicola, L., Xiang, Y., Vlassak, J., der Giessen, E. V., Needleman, A., 2006. Plastic deformation of freestanding thin films: Experiments and modeling. Journal of the Mechanics and Physics of Solids 54 (10), 2089 – 2110.

Pei, L., Hyun, S., Molinari, J., Robbins, M. O., 2005. Finite element modeling of elastoplastic contact between rough surfaces. Journal of the Mechanics and Physics of Solids 53 (11), 2385 – 2409.

Persson, B., 2006. Contact mechanics for randomly rough surfaces. Surf. Sci. Rep. 61 (4), 201–227.

Persson, B., Albohr, O., Tartaglino, U., Volokitin, A., Tosatti, E., 2004. On the nature of surface roughness with application to contact mechanics, sealing, rubber friction and adhesion. Journal of Physics: Condensed Matter 17 (1), R1.

Persson, B. N., 2001. Theory of rubber friction and contact mechanics. The Journal of Chemical Physics 115 (8), 3840–3861.

Persson, B. N. J., 2008. On the elastic energy and stress correlation in the contact between elastic solids with randomly rough surfaces. Journal of Physics: Condensed Matter 20 (31), 312001.

Plouraboué, F., Boehm, M., 1999. Multi-scale roughness transfer in cold metal rolling. Tribology International 32 (1), 45 – 57.

Polonsky, I., Keer, L., 2000. Fast methods for solving rough contact problems: A comparative study. Journal of Tribology 122 (1), 36–41.

Prodanov, N., Dapp, W. B., Müser, M. H., Feb 2014. On the contact area and mean gap of rough, elastic contacts: Dimensional analysis, numerical corrections, and reference data. Tribology Letters 53 (2), 433–448.

Putignano, C., Afferrante, L., Carbone, G., Demelio, G., 2012a. The influence of the statistical properties of self-affine surfaces in elastic contacts: A numerical investigation. Journal of the Mechanics and Physics of Solids 60 (5), 973 – 982.

Putignano, C., Afferrante, L., Carbone, G., Demelio, G., 2012b. A new efficient numerical method for contact mechanics of rough surfaces. International Journal of Solids and Structures 49 (2), 338 – 343.

Song, H., Vakis, A., Liu, X., der Giessen, E. V., 2017. Statistical model of rough surface contact accounting for size-dependent plasticity and asperity interaction. Journal of the Mechanics and Physics of Solids 106 (Supplement C), 1 – 14.

Stanley, H., Kato, T., 1997. An fft-based method for rough surface contact. Journal of Tribology 119 (3), 481–485.

Sun, F., van der Giessen, E., Nicola, L., 2012. Plastic flattening of a sinusoidal metal surface: A discrete dislocation plasticity study. Wear 296, 672–680.

Tang, W. C., Lee, A. P., 2001. Defense applications of mems. MRS Bulletin 26 (4), 318–319.

Tas, N., Sonnenberg, T., Jansen, H., Legtenberg, R., Elwenspoek, M., 1996. Stiction in surface micromachining. Journal of Micromechanics and Microengineering 6 (4), 385.

van der Giessen, E., Needleman, A., 1995. Discrete dislocation plasticity: a simple planar model. Modelling and Simulation in Materials Science and Engineering 3 (5), 689.

Venugopalan, S. P., Müser, M. H., Nicola, L., 2017a. Green's function molecular dynamics meets discrete dislocation plasticity. Modelling and Simulation in Materials Science and Engineering 25 (6), 065018.

Venugopalan, S. P., Nicola, L., Müser, M. H., 2017b. Green's function molecular dynamics: including finite heights, shear, and body fields. Modelling and Simulation in Materials Science and Engineering 25 (3), 034001.

Volkert, C. A., Lilleodden, E. T., 2006. Size effects in the deformation of sub-micron au columns. Philosophical Magazine 86 (33-35), 5567–5579.

Widjaja, A., Van der Giessen, E., Deshpande, V., Needleman, A., 2007. Contact area and size effects in discrete dislocation modeling of wedge indentation. Journal of Materials Research 22 (3), 655–663.

Wu, J.-J., 2006. Numerical analyses on elliptical adhesive contact. Journal of Physics D: Applied Physics 39 (9), 1899–1907.

Yastrebov, V. A., Durand, J., Proudhon, H., Cailletaud, G., 2011. Rough surface contact analysis by means of the finite element method and of a new reduced model. Comptes Rendus Mécanique 339 (7), 473 – 490.

Yin, X., Komvopoulos, K., 2012. A discrete dislocation plasticity analysis of a single-crystal semi-infinite medium indented by a rigid surface exhibiting multi-scale roughness. Philosophical Magazine 92 (24), 2984–3005.

2

GREEN'S FUNCTION MOLECULAR DYNAMICS: INCLUDING FINITE HEIGHTS, SHEAR, AND BODY FIELDS

The Green's function molecular dynamics (GFMD) method for the simulation of incompressible solids under normal loading is extended in several ways: Shear is added to the GFMD continuum formulation and Poisson numbers as well as the heights of the deformed body can now be chosen at will. In addition, we give the full stress tensor inside the deformed body. We validate our generalizations by comparing our analytical and GFMD results to calculations based on the finite-element method (FEM) and full molecular dynamics simulations. For the investigated systems we observe a significant speed-up of GFMD compared to FEM. This result indicates that GFMD is a promising candidate to treat boundary conditions in discrete-dislocation-dynamics based descriptions of plasticity.

2.1. INTRODUCTION

Green's function molecular dynamics (GFMD) (Campañá and Müser, 2006; Karpov et al., 2004; Kong et al., 2009) is a boundary-value method allowing one to simulate the linear-elastic response of a solid to an external stress or, more generally, to a boundary condition. So far, GFMD has been used predominantly to describe either non-reflecting (Park et al., 2005; Pastewka et al., 2012) and thermalizing (Benassi et al., 2010; Kajita et al., 2012; Karpov et al., 2007) boundaries to which an atomistic region is coupled, or, as a tool to simulate the contact mechanics of solids with rough surfaces (Campañá and Müser, 2007; Pastewka et al., 2013; Prodanov et al., 2014). One advantage of GFMD is that it only necessitates knowledge of the displacements in the top layer of a solid and that effective interactions are block diagonal in Fourier space. Relatively large systems can therefore be simulated and be quickly relaxed. Typical system sizes in the context of contact mechanics range from $4,096 \times 4,096$ surface atoms on single CPUs (Campañá and Müser, 2007) to $O(10^5 \times 10^5)$ on supercomputers (Prodanov et al., 2014).

An additional, conceivable application consists in coupling GFMD to discrete dislocation dynamics (DDD) (van der Giessen and Needleman, 1995). The idea is to use GFMD, instead of the finite-element method, to compute the image fields of dislocations in DDD. Towards this end, we generalize the GFMD method in the following ways: First, we consider the elastic response of a cubic or an isotropic body with arbitrary Poisson number and allow for lateral displacements as well as for shear tractions in addition to normal tractions. Second, we deduce the internal stresses for a given surface boundary condition and do this for solids of arbitrary height. The approaches pursued so far were limited to either normal displacements and normal tractions in the continuum formulation (Akarapu et al., 2011; Prodanov et al., 2014) or to the full atomistic Green's functions (Campañá and Müser, 2006; Campañá and Müser, 2007), which do not relate directly to the continuum limit. While the finite-width elastic continuum problem with shear was solved by Carbone and Mangialardi (Carbone and Mangialardi, 2008), their work did not put us into the position to deduce directly the Green's function coefficients needed for a numerical implementation. In a later work, in particular appendix A of reference (Carbone et al., 2009), useful formulae for the GFMD simulations were stated, but unfortunately only for the frictionless case.

In this work, we present a solution for the Green's function of finite-height elastic

slabs having the following advantages: The only required mathematical tools are partial derivatives, Fourier transforms, and linear algebra, i.e., there is no need to solve Fredholm integral equations. All equations needed to implement the approach into computer code are given explicitly in compact form. Moreover, our approach can be readily modified in various ways. For example, it should be straightforward to extend our solution strategy to layered materials, to materials with gradient or square-gradient corrections to the elastic energy, or to non-isotropic crystals — as long as they remain homogeneous within each plane. In fact, the most important equations for non-isotropic crystals are given and tested in this work. Lastly, we validate our solution against numerical data and moreover consider various limiting cases including that of very small slab heights or that of a vanishing shear modulus characteristic for fluids.

2.2. Theoretical Considerations

2.2.1. General background

In this chapter, we are concerned with the quasi-static loading, in which case the precise dynamical response of the simulated layer does not play a role, see references (Carbone et al., 2009; Pastewka et al., 2012; Putignano et al., 2015) for generalizations from the static to the dynamic case. Moreover, we consider to load the surface of a body that is translationally invariant within the xy-plane, which, in principle, is allowed to be a gradient material as long as the gradients are normal to the xy surface plane. One can then write the linear stress-displacement relation $u[\sigma(\mathbf{r})]$ as

$$u_\alpha(\mathbf{r}) = \int d^2 r' \, G_{\alpha\beta}(\mathbf{r}') \, \sigma_{3\beta}(\mathbf{r} + \mathbf{r}'), \tag{2.1}$$

where $G_{\alpha\beta}(\mathbf{r}')$ is the Green's function tensor, $u_\alpha(\mathbf{r})$ is the α component of the displacement as a function of the (two-dimensional) in-plane coordinate $\mathbf{r}$, and $\sigma_{3\beta}$ is the traction in z-direction. In Fourier space, equation (2.1) reads

$$\tilde{u}_\alpha(\mathbf{q}) = \tilde{G}_{\alpha\beta}(\mathbf{q})\tilde{\sigma}_{3\beta}(\mathbf{q}). \tag{2.2}$$

In contact problems, one often knows the displacement of the bodies and wants to deduce the contact pressure, and thus, one usually does not need to evaluate the Green's

function (tensor) itself, but its inverse. Thus, force calculations in GFMD simulations require one to evaluate

$$\tilde{\sigma}_{3\alpha}(\mathbf{q}) = \left[\tilde{G}^{-1}(\mathbf{q}) \right]_{\alpha\beta} \tilde{u}_{\beta}(\mathbf{q}). \tag{2.3}$$

The precise functional form of the (inverse) Green's function tensor depends on the elastic properties of the deformed material including its height.

In its simplest form, usually used in the context of (continuum) contact mechanics (Persson, 2001), one is only interested in normal displacements induced by normal tractions applied to a semi-infinite, isotropic body. In this case, if the body is incompressible, $\nu = 0.5$, all quantities in equation (2.3) can be considered as scalars and the equation reduces to

$$\tilde{\sigma}(\mathbf{q}) = q E^* \tilde{u}(\mathbf{q})/2, \tag{2.4}$$

where $E^* = E/(1-\nu^2)$ is the contact modulus, E being the Young's modulus and ν the Poisson number. However, as mentioned in the introduction, we wish to generalize GFMD to give the elastic response of a body with generic Poisson's ratio, and therefore, we can no longer use a scalar to describe surface displacement. Moreover, we intend to consider problems where contact loading is not restricted to be in normal direction, i.e. tractions and/or displacement can be applied in normal or tangential directions, everywhere on the body surface. Therefore, we can no longer rely on equation (2.4) end need to find a form for the Green's function tensor in equation (2.3), which has to depend on the Poisson's ratio and on the height of the slab. Towards this end, we next calculate the analytical solutions for the displacement in linearly elastic slabs of finite height, from which the stresses can be deduced in a straightforward fashion. The stress distribution underneath the contact are of particular interest in problems as fretting fatigue, to determine whether a possible tensile loading underneath the contact would give rise to crack nucleation and propagation.

2.2.2. Analytical solutions for the displacement in finite-height, linearly elastic slabs

We consider a linearly elastic body of cubic or higher symmetry in a slab geometry with a fixed bottom, i.e., the displacement reads $\mathbf{u}(x, z = 0) = 0$ rather than $\mathbf{u}(x, z \to -\infty) \to 0$ as for semi-infinite solids. Moreover, we assume that no body forces are exerted, which

implies the usual equilibrium condition $\partial_\alpha \sigma_{\alpha\beta}(\mathbf{r}) = 0$, where $\sigma_{\alpha\beta}(\mathbf{r})$ is the stress at the point $\mathbf{r}$ inside the body and $\partial_\alpha \equiv \partial/\partial r_\alpha$. For isotropic bodies or cubic bodies with their (100) surface facing up often considered in DDD simulations (Nicola et al., 2004; Robertson and Fivel, 1999; van der Giessen and Needleman, 1995; Weygand et al., 2002) the equilibrium condition is given by

$$C_{11}\partial_1^2 u_1 + C_{44}\partial_3^2 u_1 + (C_{12} + C_{44})\partial_1\partial_3 u_3 \quad = \quad 0 \tag{2.5}$$

$$C_{11}\partial_3^2 u_3 + C_{44}\partial_1^2 u_3 + (C_{12} + C_{44})\partial_1\partial_3 u_1 \quad = \quad 0, \tag{2.6}$$

where we have restricted our attention to (1+1)-dimensional solids so that in-plane wavevectors are now scalars, and where the C_{ij}'s denote coefficients of the elastic tensor in Voigt notation.

Assuming an in-plane undulation of the top layer with the real-valued wavenumber q, equations (2.5) and (2.6) can be solved with the factorization

$$u_\alpha(x, z) = u_\alpha^0 \exp(iqx)\exp(ikz), \tag{2.7}$$

where k is a complex wavenumber satisfying

$$(k/q)^2 = -b \pm \sqrt{b^2 - 1} \tag{2.8}$$

with

$$b = \frac{C_{11}^2 + C_{44}^2 - (C_{12} + C_{44})^2}{2C_{11}C_{44}}. \tag{2.9}$$

Thus, we obtain solutions for the displacements either oscillating exponential functions for $b < 1$ or purely exponential functions for $b > 1$. The nature of the solution changes at $b = 1$, which automatically holds for isotropic media as these satisfy the isotropy condition $C_{44} = (C_{11} - C_{12})/2$. The solutions for $b = 1$ are proportional to $\exp(\pm qz)$, and, in addition, proportional to $z\exp(\pm qz)$, i.e., similar to those of critically damped harmonic oscillators. The decaying solutions can usually be ignored when the z-position of the top layer z_m satisfies $z_\mathrm{m} \gg 1/q$ but not for a finite-slab geometry.

In the remainder of this section, we focus on the isotropic case, because this is a common approximation made, for example, in DDD simulations. In the result section, we also consider the case of a cubic solid violating the isotropy condition to demonstrate

the correctness of our approach. At this point, it may suffice to state that metallic cubic crystals tend to have a relatively small shear modulus, in which case $b > 1$, while non-metals rather correspond to $b < 1$.

Due to the nature of the differential equations (2.5) and (2.6), the solutions of the in-plane cosine transform of the lateral u_1 displacement field couples to the in-plane sine transform of the normal u_3 displacement, and vice versa. Thus, we can write

$$
\begin{aligned}
u_1^c(x,z) &= \cos(qx)\tilde{u}_1^c(q,z) & (2.10) \\
u_3^s(x,z) &= \sin(qx)\tilde{u}_3^s(q,z). & (2.11)
\end{aligned}
$$

Solutions satisfying the boundary condition $\mathbf{u}(x,0) = 0$ and the differential equation for isotropic media are then obtained after some algebra to satisfy

$$
\begin{bmatrix} \tilde{u}_1^c(q,z) \\ \tilde{u}_3^s(q,z) \end{bmatrix} = \begin{bmatrix} f_1(qz) & -f_2(qz) \\ f_2(qz) & f_3(qz) \end{bmatrix} \begin{bmatrix} A_1 \\ A_2 \end{bmatrix} \tag{2.12}
$$

with

$$
f_1(qz) = \sinh(qz) + \frac{1-s}{1+s} qz \cosh(qz) \tag{2.13}
$$

$$
f_2(qz) = \frac{1-s}{1+s} qz \sinh(qz) \tag{2.14}
$$

$$
f_3(qz) = \sinh(qz) - \frac{1-s}{1+s} qz \cosh(qz), \tag{2.15}
$$

where $s \equiv C_{44}/C_{11}$. The latter ratio has allowed values of $0 < s < 1$ for stable, two-dimensional isotropic solids (Born and Huang, 1998). The coefficients $A_{1,2}$ follow from equation (2.12) once $\tilde{u}_1^c(q,z)$ and $\tilde{u}_3^s(q,z)$ are given at $z = z_m$, where z_m is the height of the undeformed solid. Lastly, the in-plane sine transform of u_1 and cosine transform of u_3 can be calculated in a similar fashion via:

$$
\begin{bmatrix} \tilde{u}_1^s(q,z) \\ \tilde{u}_3^c(q,z) \end{bmatrix} = \begin{bmatrix} f_1(qz) & f_2(qz) \\ -f_2(qz) & f_3(qz) \end{bmatrix} \begin{bmatrix} B_1 \\ B_2 \end{bmatrix}. \tag{2.16}
$$

In summary, for an arbitrary surface displacement field $\mathbf{u}(x,z_m)$, the in-plane Fourier transform is taken to yield $\tilde{\mathbf{u}}(q,z_m)$. The real and imaginary parts can be associated with left-hand sides of equations (2.12) and (2.16), which allow one to determine the perti-

nent coefficients $A_{1,2}$ and $B_{1,2}$ for each wavenumber q by evaluating them at $z = z_{\mathrm{m}}$. The knowledge of these coefficients then allows one to deduce the displacement inside the body.

2.2.3. FINITE-HEIGHT-SLAB STRAIN, STRESS, AND ENERGY DENSITY

Not only the displacement but also the strain and thus the stress field on the surface or inside the body can be deduced as soon as the coefficients $A_{1,2}$ and $B_{1,2}$ have been determined for a given surface topography, obtained by perturbation of an initially flat surface. For reasons of simplicity, we first restrict our attention to the case of a perturbation by a single wave number q and $B_{1,2} = 0$. The elements of the infinitesimal Cauchy's strain tensor (in Voigt notation) are then given by

$$
\begin{aligned}
\epsilon_1(x, z) &\equiv \partial_1 u_1(x, z) \\
&= -q \sin(qx) \tilde{u}_1^{\mathrm{c}}(q, z) \quad &(2.17)\\
\epsilon_3(x, z) &\equiv \partial_3 u_3(x, z) \\
&= \sin(qx) \partial_3 \tilde{u}_3^{\mathrm{s}}(q, z) \quad &(2.18)\\
\epsilon_5(x, z) &\equiv \partial_1 u_3(x, z) + \partial_3 u_1(x, z) \\
&= \cos(qx) \left\{ q \tilde{u}_3^{\mathrm{s}}(q, z) + \partial_3 \tilde{u}_1^{\mathrm{c}}(q, z) \right\} \quad &(2.19)
\end{aligned}
$$

These expressions can now be used to compute the stresses inside the body as well as on its surface with the usual stress-strain relations. Knowledge of the latter suffices to determine the work per unit area needed to deform the body – assuming small surface slopes and thus the surface normal to be approximately parallel to the z-axis – via

$$
\begin{aligned}
v_{\mathrm{el}} = \frac{1}{L} \int_0^L dx \Bigg[&\int_0^{u_1(x, z_{\mathrm{m}})} \sigma_{31}(x, z_{\mathrm{m}}) d u_1(x, z_{\mathrm{m}}) \\
&+ \int_0^{u_3(x, z_{\mathrm{m}})} \sigma_{33}(x, z_{\mathrm{m}}) d u_3(x, z_{\mathrm{m}}) \Bigg].
\end{aligned} \quad (2.20)
$$

This yields

$$
v_{\mathrm{el}} = \frac{C_{44}}{2} \tilde{\epsilon}_5^{\mathrm{c}}(q, z_{\mathrm{m}}) \tilde{u}_1^{\mathrm{c}}(q, z_{\mathrm{m}}) + \left\{ \frac{C_{11}}{2} \tilde{\epsilon}_3^{\mathrm{s}}(q, z_{\mathrm{m}}) + \frac{C_{12}}{2} \tilde{\epsilon}_1^{\mathrm{s}}(q, z_{\mathrm{m}}) \right\} \tilde{u}_3^{\mathrm{s}}(q, z_{\mathrm{m}}) \quad (2.21)
$$

with

$$\tilde{\epsilon}_1^{s}(q,z) = -q\tilde{u}_1^{c}(q,z) \tag{2.22}$$

$$\tilde{\epsilon}_3^{s}(q,z) = \partial_3\tilde{u}_3^{s}(q,z) \tag{2.23}$$

$$\tilde{\epsilon}_5^{c}(q,z) = \partial_3\tilde{u}_1^{c}(q,z) + q\tilde{u}_3^{s}(q,z). \tag{2.24}$$

Thus, for the surface layer

$$\tilde{\epsilon}_1^{s}(q,z_{m}) = -q\tilde{u}_1^{c}(q,z_{m}) \tag{2.25}$$

$$
\begin{aligned}
\tilde{\epsilon}_3^{s}(q,z_{m}) = \;& r\,\frac{\cosh^2(qz_{m}) - r(qz_{m})^2 - 1}{||f(z_{m})||}\,q\tilde{u}_1^{c}(q,z_{m}) \\
& + (1-r)\,\frac{\cosh(qz_{m})\sinh(qz_{m}) + rqz_{m}}{||f(z_{m})||}\,q\tilde{u}_3^{s}(q,z_{m})
\end{aligned} \tag{2.26}
$$

$$
\begin{aligned}
\tilde{\epsilon}_5^{c}(q,z_{m}) = \;& (1+r)\,\frac{\cosh(qz_{m})\sinh(qz_{m}) - rqz_{m}}{||f(z_{m})||}\,q\tilde{u}_1^{c}(q,z_{m}) \\
& + \frac{(1-r)\sinh^2(qz_{m}) - 2(rqz_{m})^2}{||f(z_{m})||}\,q\tilde{u}_3^{s}(q,z_{m})
\end{aligned} \tag{2.27}
$$

where

$$r \equiv \frac{1-s}{1+s} \tag{2.28}$$

and

$$
\begin{aligned}
||f(qz)|| &\equiv f_1(qz)f_3(qz) + f_2^2(qz) \\
&= \cosh^2(qz) - (rqz)^2 - 1.
\end{aligned} \tag{2.29}
$$

Gathering all expressions entering the elastic energy leads to

$$
\nu_{el} = \frac{q}{2}\left[\tilde{u}_1^{c}(q,z_{m}),\tilde{u}_3^{s}(q,z_{m})\right]
\begin{bmatrix} M_{11}(qz_{m}) & M_{13}(qz_{m}) \\ M_{13}(qz_{m}) & M_{33}(qz_{m}) \end{bmatrix}
\begin{bmatrix} \tilde{u}_1^{c}(q,z_{m}) \\ \tilde{u}_3^{s}(q,z_{m}) \end{bmatrix}
\tag{2.30}
$$

with

$$M_{11}(qz_{\mathrm{m}}) \;=\; (1-r)\,\frac{\cosh(qz_{\mathrm{m}})\sinh(qz_{\mathrm{m}}) - r q z_{\mathrm{m}}}{\|f(qz_{\mathrm{m}})\|}\,C_{11} \tag{2.31}$$

$$M_{13}(qz_{\mathrm{m}}) \;=\; \frac{1-r}{1+r}\,\frac{(1-r)\sinh^2(qz_{\mathrm{m}}) - 2(r q z_{\mathrm{m}})^2}{\|f(qz_{\mathrm{m}})\|}\,C_{11} \tag{2.32}$$

$$M_{33}(qz_{\mathrm{m}}) \;=\; (1-r)\,\frac{\cosh(qz_{\mathrm{m}})\sinh(qz_{\mathrm{m}}) + r q z_{\mathrm{m}}}{\|f(qz_{\mathrm{m}})\|}\,C_{11}, \tag{2.33}$$

which is a central result for GFMD simulations in which both normal and shear stresses are considered.

For reasons of completeness, we state the general elastic energy density

$$v_{\mathrm{el}} = \sum_{\mathbf{q}} \frac{q}{2}\left[\tilde{u}_1^*(\mathbf{q}), \tilde{u}_3^*(\mathbf{q})\right]
\begin{bmatrix} M_{11}(qz_{\mathrm{m}}) & -i M_{13}(qz_{\mathrm{m}}) \\ i M_{13}(qz_{\mathrm{m}}) & M_{33}(qz_{\mathrm{m}}) \end{bmatrix}
\begin{bmatrix} \tilde{u}_1(\mathbf{q}) \\ \tilde{u}_3(\mathbf{q}) \end{bmatrix}, \tag{2.34}$$

where $\tilde{u}(\mathbf{q})$ is now the complete, complex Fourier transform of the displacement of wavevector $\mathbf{q}$. For zero shear (normal) stress, the elastic energy is minimized with respect to the lateral (normal) displacement and thus becomes

$$v_{\mathrm{el}} \;=\; \frac{q}{2}\left\{ M_{11}(qz_{\mathrm{m}}) - \frac{M_{13}^2(qz_{\mathrm{m}})}{M_{33}(qz_{\mathrm{m}})} \right\} |\tilde{u}_1(\mathbf{q})|^2 \quad \text{(zero normal stress)} \tag{2.35}$$

$$v_{\mathrm{el}} \;=\; \frac{q}{2}\left\{ M_{33}(qz_{\mathrm{m}}) - \frac{M_{13}^2(qz_{\mathrm{m}})}{M_{11}(qz_{\mathrm{m}})} \right\} |\tilde{u}_3(\mathbf{q})|^2 \quad \text{(frictionless contact)}. \tag{2.36}$$

ASYMPTOTIC ANALYSIS

It is instructive to consider various limits. First, for large wavevectors, the problem reduces to that of a semi-infinite solid. In this case, the quotients in equations (2.31)-(2.33) with $\|f(qz_{\mathrm{m}})\|$ in the denominator can be set to one and the elastic energy is essentially q times an effective modulus times a squared displacement. More specifically, the $M_{ij}(qz_{\mathrm{m}})$ become

$$M_{11}(qz_{\mathrm{m}} \gg 1) \;=\; \frac{2}{1+s}\,C_{44} \tag{2.37}$$

$$M_{13}(qz_{\mathrm{m}} \gg 1) \;=\; \frac{2s}{1+s}\,C_{44} \tag{2.38}$$

$$M_{33}(qz_{\mathrm{m}} \gg 1) \;=\; \frac{2}{1+s}\,C_{44}. \tag{2.39}$$

In the second limit, i.e. that of short wavevectors, we find

$$qM_{11}(qz_{\mathrm{m}} \ll 1) \quad = \quad \frac{C_{44}}{z_{\mathrm{m}}} \tag{2.40}$$

$$qM_{13}(qz_{\mathrm{m}} \ll 1) \quad = 0 \tag{2.41}$$

$$qM_{33}(qz_{\mathrm{m}} \ll 1) \quad = \quad \frac{C_{11}}{z_{\mathrm{m}}} \tag{2.42}$$

so that we may write for center-of-mass displacements

$$v_{\mathrm{el}}(q=0) = \frac{C_{44}}{2z_{\mathrm{m}}}\tilde{u}_1^2(0) + \frac{C_{11}}{2z_{\mathrm{m}}}\tilde{u}_3^2(0). \tag{2.43}$$

This corresponds to the elastic energy — per unit area — of an isotropically deformed (and periodically repeated) solid being glued to a rigid substrate.

As a brief side aspect, let us also discuss the limiting case of $C_{44} = 0$ ($\Rightarrow r = 1$) which describes a compressible fluid. Given the prefactors in equations (2.31)-(2.33), one might have been tempted to set *all* $M_{ij}(qz_{\mathrm{m}})$ to zero. However, the just-presented asymptotic analysis reveals that this would not have lead to the correct result for $M_{33}(qz_{\mathrm{m}} \to 0)$, which remains finite even for a vanishingly small shear modulus. Thus, the only mode necessitating elastic energy when altering the shape of the "top layer" of a fluid is that which leads to a volume reduction, i.e., the $\tilde{u}_3(q=0)$ mode.

We conclude this section by making the link of our results to the contact modulus E^* introduced in equation (2.4). For semi-infinite solids, or large qz_{m}, the expression in the curly brackets in equation (2.36) reduces to $2(1-s)C_{44}$, which indeed can be shown to be half E^*. This implies that equation (2.36) is consistent with (2.4) in the limit of a frictionless semi-infinite contact.

2.3. NUMERICAL RESULTS

2.3.1. DISPLACEMENTS IN NON-ISOTROPIC SOLIDS

To model a non-isotropic solid, we consider a cubic crystal with its (100) surface facing up. To make the comparison of continuum theory to full molecular dynamics (MD) simulations as transparent as possible, we furthermore restrict ourselves to a simple cubic lattice in which each atom (which one may also see as a grid point) is connected to its nearest neighbors with a spring of stiffness k_1 and to next-nearest neighors with a

spring of stiffness $k_2 = k_1$. Mechanical equilibrium of the springs is assumed at a distance a_0 between nearest neighbors and $\sqrt{2}a_0$ for next-nearest neighbors. With these definitions, it is readily seen that the elastic tensor — fully defined by $C_{11} = (k_1 + k_2)/a_0$ and $C_{12} = C_{44} = k_2/a_0$ — violates the isotropy condition for the given choice of $k_1 = k_2$, since in this case $C_{44} > (C_{11} - C_{12})/2$. Here, the stiffness is divided by a_0 so that the elastic constants have the usual units.

In our example, we consider a slab of height $L_z = L_x/2$, where $L_x = 40a_0$ is the lateral length of the domain, which is repeated periodically along the $x-$direction. The just-defined system is solved with a self-written MD code, in which individual atoms are also coupled to damping linear in velocity. The mass of atoms is set to unity, the time step to 0.1 and damping to 0.25. Two cases of displacements in the top layer are treated: normal loading for which $u_1(x, z_m) = 0$, $u_3(x, z_m) = A_0 \cos(2\pi x/L_x)$ and shear loading for which $u_1(x, z_m) = A_0 \cos(2\pi x/L_x)$, $u_3(x, z_m) = 0$. To justify the assumption of linear elasticity, the maximum displacement amplitude is set to $A_0 = a_0/100$. Top and bottom layer are kept fixed. The system relaxes after a few thousand time steps.
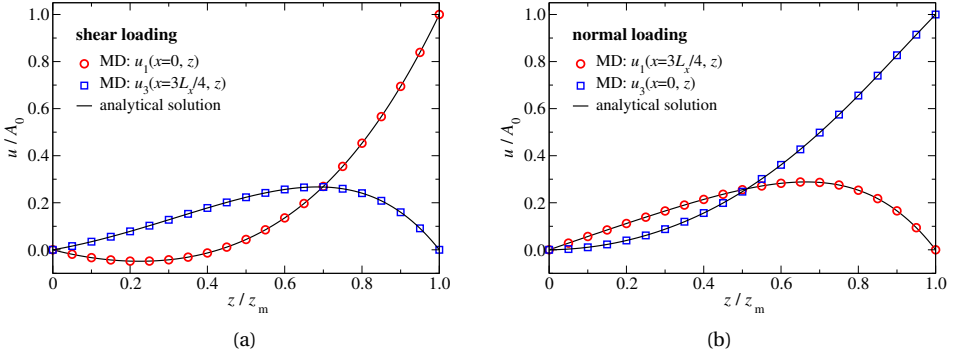
Figure 2.1: Lateral (red circles) and normal (blue squares) displacements $u_{1,3}$ at selected cross sections for shear (left) and normal (right) loading as obtained from MD simulations. The displacements are given in units of the maximum displacement A_0, which is valid at the top layer of the solids located at the normal coordinate $z = z_m = L_x/2$. The displacements are set to zero at the bottom layer ($z = 0$). Full lines represent the continuum solutions used to obtain internal stresses in GFMD simulations.

Agreement between full MD and the analytical expressions for the displacement fields is clearly revealed.

2.3.2. DISPLACEMENT AND STRESS FIELDS IN ISOTROPIC SOLIDS

As a benchmark problem to compare GFMD to FEM we here consider the indentation of an isotropic elastic two-dimensional slab by an array of flat rigid punches. Contact between punches and slab is taken to be fully sticking. The analysis is performed on a periodic unit cell with fixed bottom as shown schematically in figure 2.2(a).

(a)   (b)
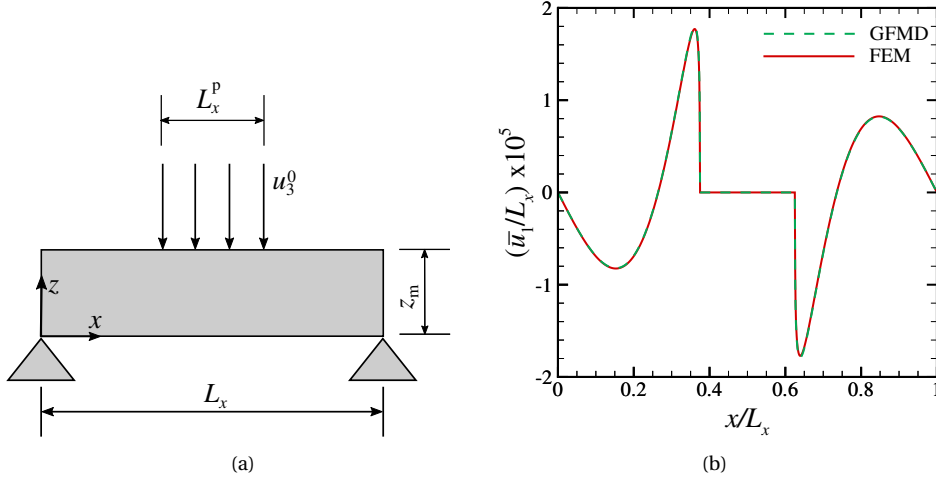
Figure 2.2: (a) Periodic unit cell of an isotropic slab indented by a flat rigid sticking punch. (b) The normalized tangential surface displacement $\bar{u}_1/L_x$ obtained using GFMD and FEM.

Normal displacement is prescribed at the contact of length L_x^{p}:

$$u_3(x, z_{\mathrm{m}}) = u_3^0 \qquad \text{for} \qquad \frac{L_x - L_x^{\mathrm{p}}}{2} < x < \frac{L_x + L_x^{\mathrm{p}}}{2}. \qquad (2.44)$$

The slab is indented to $u_3^0/L_x = 2.5 \times 10^{-4}$. Outside the contact region, the top surface is traction free. The aspect ratio of the slab, which is taken to have the elastic properties of aluminum, $C_{11} = 105$ GPa and $s = C_{44}/C_{11} = 0.25$, is $a = z_{\mathrm{m}}/L_x = 1/4$, and the rigid punch is $L_x^{\mathrm{p}}/L_x = 1/4$. For the finite-element analysis the slab is discretized using a uniform mesh of square elements. The number of degrees of freedom is $n_{\mathrm{dof}} = 2nnx \times nnz$, where nnx is the number of nodes in x–direction, and nnz the number of nodes in z–direction. For the GFMD simulation the surface is discretized using nx equispaced grid points, with $nx = nnx$. Contact between the rigid indenters and the slab is modeled through a hard-wall potential. The static solution is found in GFMD using damped dynamics as

described in (Prodanov et al., 2014). The damping factor η used in this simulations is

$$\eta_x = \eta_z = \eta_0 \frac{1}{\tau \sqrt{nx}}, \tag{2.45}$$

where η_0 is the damping prefactor and τ is the time step. The damping prefactor is selected such that the slowest mode is slightly under-damped in z-direction. The number of MD iterations used to reach convergence scales as $n_{it} \sim O(\sqrt{nx})$ and the time step is τ=0.25. The normalized lateral surface displacement $\bar{u}_1/L_x$ obtained by the two methods is shown for $nnx = nx = 1024$ in figure 2.2(b). The over bar indicates the value of the variable at the surface. No differences can be seen by the naked eye.

The displacement and stress fields inside the body for the GFMD simulations are calculated using equations (12-16) and (25-27). For a better comparison with FEM, the fields are evaluated at all locations inside the body corresponding to the nodes in the FEM calculation. The body fields hence obtained are compared with those obtained using FEM in figures 2.3 and 2.4.
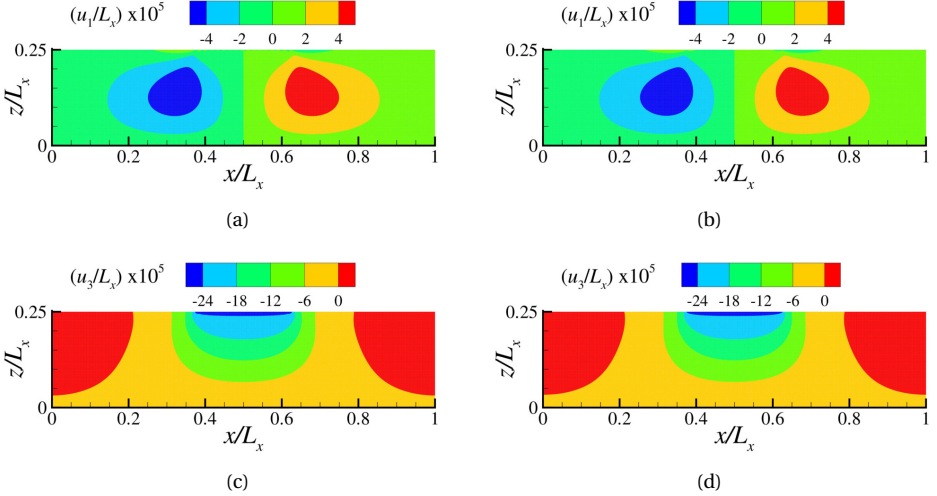
Figure 2.3: Displacement fields obtained using: (a), (c) GFMD and analytical solution; (b), (d) and FEM.
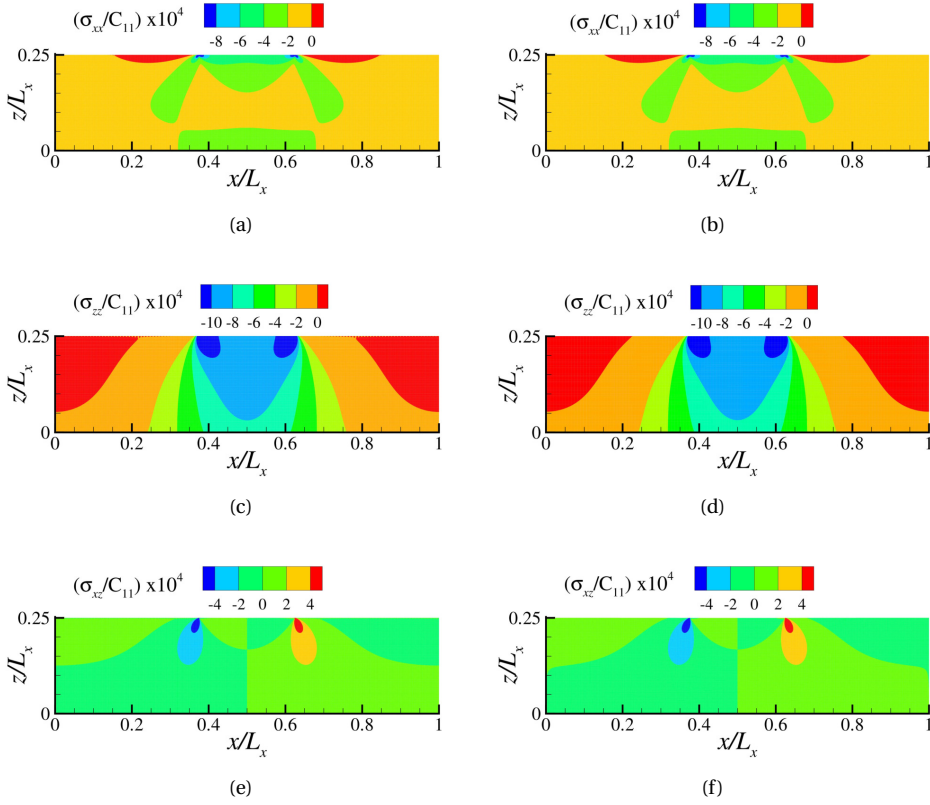
Figure 2.4: Stress fields obtained using: (a), (c), (e) GFMD and analytical solution; (b), (d), (f) and FEM.

2.3.3. CONVERGENCE RATE AND SIMULATION TIME

The convergence rate is studied considering the calculation of the L_2 norm of the surface displacement,

$$\|\bar{u}_1\|_{L_2} = \sqrt{\sum_{i=1}^{nx} u_1(x_i, z_{\mathrm{m}})^2}. \tag{2.46}$$

Following (Szabo and Babuška, 1991), the error in the norm obtained using FEM as a function of the degrees of freedom in the simulation can be written as:

$$\|(\bar{u}_1/L_x)\|_{L_2}^{\mathrm{FEM}} - \|(\bar{u}_1/L_x)\|_{L_2}^{\mathrm{exact}} \approx \frac{\kappa}{n_{\mathrm{dof}}^{\beta}}. \tag{2.47}$$

The exact solution, the asymptotic rate of convergence β, and the prefactor κ, are obtained by linearly fitting three data points corresponding to nnx = 256, 512, 1024. As expected (Szabo and Babuška, 1991), given that the mesh refinement is uniform and the order of the interpolating polynomial for the shape functions is one, the asymptotic rate of convergence is found to be 0.5:

$$\|(\bar{u}_1/L_x)\|_{L_2} = \left(0.692 - \frac{2.552}{n_{\text{dof}}^{0.5}}\right) \times 10^{-5}. \tag{2.48}$$

Since the finite-element mesh has square elements, it follows that

$$\frac{1}{nnx} = \left(\frac{2a}{n_{\text{dof}}}\right)^{0.5}. \tag{2.49}$$

We can therefore rewrite the L_2 norm as

$$\|(\bar{u}_1/L_x)\|_{L_2} = \left(0.692 - \frac{2.552}{(2a)^{0.5}} \frac{1}{nnx}\right) \times 10^{-5}, \tag{2.50}$$

which allows for direct comparison with GFMD (see figure 2.5(a)). The order of convergence with respect to the discretization of the two methods is found to be the same, while the prefactors are favorable for GFMD, i.e. $\kappa/L_x = -3.609 \times 10^{-5}$ for FEM while $\kappa/L_x = -1.653 \times 10^{-5}$ for GFMD. Figure 2.5(b) shows the simulation time as a function of the surface discretization. The results are all obtained on a single Intel Xeon(R) 3.10 GHz processor with 31.3 Gbytes of RAM. The GFMD simulations are found to be faster than FEM, and the computational advantage increases with increasing system size. In addition to this, a smaller number of grid points are needed in GFMD to obtain the same results as in FEM. For the simulation reported here, if we decide to tolerate an error $e = 0.005$ in the L_2 norm of lateral surface displacement, the GFMD simulations require nx =128 grid points while the FEM simulations need nnx =1024 surface nodes. This results in a GFMD simulation being 1650 times faster than FEM.

It is to be noted here that: (1) we have not searched for the optimal meshing scheme to solve the finite-element problem, simply used a mesh with squared elements for ease of comparison with the equi-spaced surface grid points used in GFMD; (2) the speed of the finite-element simulation depends heavily on the solver used. Here we have used a direct sparse solver with skyline storage, where the time consuming step is the fac-
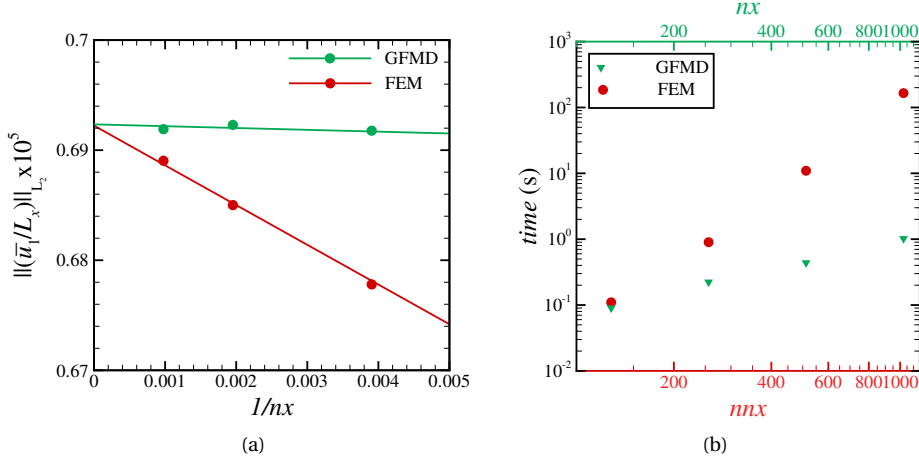
Figure 2.5: (a) The L_2 norm of tangential surface displacement obtained using GFMD and FEM are plotted as a function of $1/nx$ (b) Simulation time for GFMD compared with FEM.

torization of the skymatrix. The order of factorization in a skyline solver is generally $O((nnx\,B)^2)$ (Synn and Fulton, 1995) where B is the mean bandwidth, which cannot exceed nnx. We are aware that for large systems, an iterative solver would be much more cost-effective. In GFMD, the computational complexity scales with $O(nx\sqrt{nx}\log nx)$, (3) the speed of the GFMD simulation depends on the choice of the damping factors, which in general are different in the x and z-direction. The optimal damping factor to obtain critical damping of the system depends on the loading, the height of the slab and the elastic constants. We here simply considered a single damping factor that would critically damp the modes in z-direction, and thus under-damp the modes in x-direction.

2.4. CONCLUSIONS

Green's function molecular dynamics, a fastly converging boundary value method used to compute contact pressures and surface displacements of incompressible continuum semi-infinite solids, is here extended to apply to finite solids with generic Poisson's ratio. Moreover, the body fields can now be computed analytically from generic tractions and/or surface displacements. This extension allows the GFMD technique to provide the same information that can be obtained through the FEM, but with a significant gain in simulation time. An additional advantage of GFMD is that for typical contact problems,

where the contact area evolves during the simulation, the contact can be easily captured and described by means of an interaction potential. We have here used a hard-wall potential, but one can also model the bodies in contact explicitly and apply an interaction potential, as the Xu-Needleman (Xu and Needleman, 1993), where the contact response in normal direction is coupled to that in tangential direction.

An interesting application that can be envisaged for the GFMD method, in virtue of the extensions presented in this chapter, is the replacement of the FEM in discrete dislocation plasticity simulations of contact. This has the potential to significantly increase the time efficiency of the discrete dislocation plasticity calculations by that allowing to extend the applicability of such models to bodies of larger size, and with a realistic surface profile.

REFERENCES

Akarapu, S., Sharp, T., Robbins, M. O., 2011. Phys. Rev. Lett. 106, 204301.

Benassi, A., Vanossi, A., Santoro, G. E., Tosatti, E., August 2010. Parameter-free dissipation in simulated sliding friction. Phys. Rev. B 82, 081401.

Born, M., Huang, K., 1998. Dynamical Theory of Crystal Lattices. International series of monographs on physics. Clarendon Press.

Campañá, C., Müser, M. H., Aug 2006. Practical Green's function approach to the simulation of elastic semi-infinite solids. Physical Review B 74, 075420.

Campañá, C., Müser, M. H., 2007. EPL 77, 38005.

Carbone, G., Lorenz, B., Persson, B. N. J., Wohlers, A., 2009. Eur. Phys. J. E 29, 275–284.

Carbone, G., Mangialardi, L., 2008. J. Mech. Phys. Sol. 56, 684–706.

Kajita, S., Washizu, H., Ohmori, T., 2012. Phys. Rev. B 86, 075453.

Karpov, E. G., Park, H. S., Liu, W. K., September 2007. A phonon heat bath approach for the atomistic and multiscale simulation of solids. Int. J. Numer. Meth. Engng 70, 351–378.

Karpov, E. G., Wagner, G. J., Liu, W. K., December 2004. A Green's function approach to deriving non-reflecting boundary conditions in molecular dynamics simulations. Int. J. Numer. Meth. Engng 62, 1250–1262.

Kong, L. T., Bartels, G., Denniston, C., Campañá, C., Müser, M. H., 2009. Implementation of Green's function molecular dynamics: An extension to LAMMPS. Comput. Phys. Commun., 1004–1010.

Nicola, L., der Giessen, E. V., Needleman, A., 004 2004. Relaxation of thermal stress by dislocation motion in passivated metal interconnects. Journal of Materials Research 19 (4), 1216–1226.

Park, H. S., Karpov, E. G., Liu, W. K., September 2005. Non-reflecting boundary conditions for atomistic, continuum and coupled atomistic/continuum simulations. Int. J. Numer. Meth. Engng 64, 237–259.

Pastewka, L., Prodanov, N., Lorenz, B., Müser, M. H., Robbins, M. O., Persson, B. N. J., 2013. Phys. Rev. E 87, 062809.

Pastewka, L., Sharp, T. A., Robbins, M. O., 2012. Phys. Rev. B 86, 075459.

Persson, B. N., 2001. Theory of rubber friction and contact mechanics. The Journal of Chemical Physics 115 (8), 3840–3861.

Prodanov, N., Dapp, W. B., Müser, M. H., 2014. On the contact area and mean gap of rough, elastic contacts: Dimensional analysis, numerical corrections, and reference data. Tribology Letters 53 (2), 433–448.

Putignano, C., Carbone, G., Dini, D., 2015. International Journal of Solids and Structures x, X.

Robertson, C. F., Fivel, M. C., jun 1999. A study of the submicron indent-induced plastic deformation. Journal of Materials Research 14 (06), 2251–2258.

Synn, S. Y., Fulton, R. E., 1995. The performance prediction of a parallel skyline solver and its implementation for large scale structure analysis. Computing Systems in Engineering 6 (3), 275 – 284.

Szabo, B., Babuška, I., 1991. Finite Element Analysis. A Wiley-Interscience publication. Wiley.

van der Giessen, E., Needleman, A., 1995. Discrete dislocation plasticity: a simple planar model. Modelling and Simulation in Materials Science and Engineering 3 (5), 689.

Venugopalan, S. P., Nicola, L., Müser, M. H., 2017. Green's function molecular dynamics: including finite heights, shear, and body fields. Modelling and Simulation in Materials Science and Engineering 25 (3), 034001.

Weygand, D., Friedman, L. H., der Giessen, E. V., Needleman, A., 2002. Aspects of boundary-value problem solutions with three-dimensional dislocation dynamics. Modelling and Simulation in Materials Science and Engineering 10 (4), 437.

Xu, X. P., Needleman, A., 1993. Void nucleation by inclusion debonding in a crystal matrix. Modelling and Simulation in Materials Science and Engineering 1 (2), 111.

3

GREEN'S FUNCTION MOLECULAR DYNAMICS MEETS DISCRETE DISLOCATION PLASTICITY

Metals deform plastically at the asperity level when brought in contact with a counter body even when the nominal contact pressure is small. Modeling the plasticity of solids with rough surfaces is challenging due to the multi-scale nature of surface roughness and the length-scale dependence of plasticity. While discrete-dislocation plasticity (DDP) simulations capture size-dependent plasticity by keeping track of the motion of individual dislocations, only simple two-dimensional surface geometries have so far been studied with DDP. The main computational bottleneck in contact problems modeled by DDP is the calculation of the dislocation image fields. We address this issue by combining two-dimensional DDP with Green's function molecular dynamics (GFMD). The resulting method allows for an efficient boundary-value-method based treatment of elasticity in the presence of dislocations. We demonstrate that our method captures plasticity quantitatively from single to many dislocations and that it scales more favorably with system size than conventional methods. We also derive the relevant Green's functions for elastic slabs of finite width allowing arbitrary boundary conditions on top and bottom surface to be simulated.

3.1. INTRODUCTION

Modeling the contact mechanics of solid bodies assuming realistic surface roughness is highly relevant to tribology, the science of friction. This is a demanding task, because the height spectra of most surfaces, even polished ones, have non-negligible magnitude over several decades of wavelengths, typically from the atomic scale to several dozen or even hundreds of microns (Plouraboué and Boehm, 1999; Simonsen et al., 2002), i.e., the root-mean-square heights are determined by the longest-wavelength height fluctuations (relevant for sealing and lubricant flow) while the root-mean-square gradients (relevant for typical contact stresses, at least in the elastic limit) are determined by the shortest wavelengths. In the past years, various theories of rough surface contact have been presented (Archard, 1957; Bush et al., 1975; Greenwood and Williamson, 1966; Persson, 2006, 2001, 2008). Persson's contact-mechanics theory (Persson, 2006, 2001, 2008) appears particularly promising to us, because it accounts for long-range elastic deformations, unlike traditional approaches such as those inspired by Greenwood and Williamson (Greenwood and Williamson, 1966), who pursued local bearing models. In fact, Persson theory reproduces quite well experiments and numerical results on relative contact area, interfacial stress distribution functions, stress spectra, and gap distribution functions, although it requires a fitting parameter of order unity. However, the validity of Persson's analysis of plastic contacts (Persson, 2006) in the range where plasticity is size-dependent (Fleck et al., 1994; Greer et al., 2005; Ma and Clarke, 1995; Nicola et al., 2006a) has not yet been shown.

Numerical simulations of contact between elastic rough surfaces are made possible through several techniques. Of particular interest are the boundary-element based approaches such as BEM (Putignano et al., 2012a,b; Stanley and Kato, 1997) and Green's function molecular dynamics (GFMD) (Campañá and Müser, 2007; Campañá et al., 2008; Kajita, 2016; Wagner et al., 2004, 2005), which calculate the response of a solid to contact loading by modeling only the surface. These methods are suitable to study large systems where the surface roughness is described by many orders of length scale (Campañá and Müser, 2007; Dapp et al., 2014; Prodanov et al., 2014). In this work, we choose GFMD over BEM, since it is a simpler method, which does not involve solving the Fredholm integral equations. In GFMD, the equilibrium positions of the interfacial grid points are found by means of damped dynamics in Fourier space, where the individual modes

decouple. This allows for large systems to be quickly brought to equilibrium. While the computational complexity of BEM scales with $O(n^2)$, where n is the number of discretization nodes, GFMD scales as $O(n\sqrt{n}\log(n))$. Furthermore, it is straightforwad in GFMD to employ non-holonomic boundary conditions and/or interaction potentials between the contacting bodies and hence it is cost-effective in studying problems where the contact area is not known *a priori*. Conventional FEM or BEM methods typically require several iterations as well as incremental updating of the boundary conditions in order to converge to a final contact area. Additionally, GFMD has the advantage that it can be extended to a multi-scale method (Pastewka et al., 2012) where the surface layer can be described atomically and the substrate underneath be treated within the harmonic approximation. Pastewka *et al.* (Pastewka and Robbins, 2014; Pastewka et al., 2012) have shown that the elastic Green's function can be quickly computed from interatomic potentials and a seamless coupling to the atomic region can be derived even for interactions going beyond nearest-neighbor interactions. GFMD has been successfully used to model the contact response of semi-infinite elastic solids (Campañá et al., 2007; Pastewka et al., 2013; Prodanov et al., 2014), while plasticity was neglected.

There has also been much progress in the numerical study of elasto-plastic contacts. These, however, are either based on continuum plasticity (Almqvist et al., 2007; Kogut and Etsion, 2002; Pei et al., 2005), or, limited to single-wavelength roughness (Song et al., 2017), or, based on brute-force all-atom approaches (Mo et al., 2009; Spijker et al., 2011). To date, no studies of rough surface contact appear to have disseminated, in which (size-dependent) plasticity and long-range elasticity were both accurately modeled. Our work aims at building such a model.

Size-dependent plasticity in metal crystals has been successfully predicted by discrete dislocation plasticity (DDP) (van der Giessen and Needleman, 1995) simulations, which for simple problems, as the tensile response of free–standing metal films, give results in quantitative agreement with experiments (Nicola et al., 2006b). In the context of contact mechanics, DDP has been used to study indentation of flat surfaced single crystals with single indenters (Balint et al., 2006; Widjaja et al., 2007), periodic indenters (Nicola et al., 2007, 2008), as well as an indenter with self-affine surface modeled as a collection of Hertzian contacts (Yin and Komvopoulos, 2012). The only DDP studies, in which the plastically deforming bodies were not approximated to be flat, involved the

flattening of simple sinusoidal surfaces (Ng and Nicola, 2016a,b; Sun et al., 2012). Results showed that the contact area is not continuous, but serrated, as a consequence of dislocations exiting the surface through discrete slip planes and leaving crystallographic steps. Due to the serrated nature of the contact area, the local contact pressure presented high spikes, at odds with the pressure profiles predicted by continuum plasticity. The study of size-dependent plasticity for realistic surface geometries is computationally very expensive. In order to being able to study indentation using realistic surface geometries, we here combine the accurate description of plasticity offered by DDP with the fastly converging elastic solution delivered by GFMD, in a modeling technique which we name Green's function dislocation dynamics (GFDD). This is not the first attempt to combine dislocation dynamics with a boundary element method (El-Awady et al., 2008, 2009; Zhou et al., 2011, 2010). However, for realistic surface geometries coming into contact, which require a fine discretization, GFDD should be more cost-effective. This is because the method relies on fast Fourier transform (FFT) and employs damped dynamics to quickly equilibrate large systems.

We briefly introduce DDP in section 3.2 and GFMD in section 3.3. We then present the methodology of the new model in section 5.2.2. The results obtained using the new GFDD model are compared with DDP in section 3.5 and 3.6. Section 4.4 summarizes the advantages and potentials of the new method.

3.2. DISCRETE DISLOCATION PLASTICITY

Discrete dislocation plasticity is a numerical technique to solve boundary-value problems (b.v.p), which treats plasticity as the collective motion of discrete dislocations (van der Giessen and Needleman, 1995). The dislocations are modeled as line defects in an elastic continuum. The solution at each time step of the simulation is obtained by the superposition of two linear elastic solutions: The elastic fields for dislocations in a homogeneous infinite solid, and the solution to the complementary elastic b.v.p., which corrects for the boundary conditions. The methodology is illustrated for the indentation of a single crystal by an array of flat rigid indenters in figure 3.1. The elastic dislocation fields are represented by a superscript ($^\mathrm{d}$), the fields solving the complementary b.v.p. by a superscript (^). The elastic dislocation fields are given analytically. The dislocation in the repetitive cell and its periodic replicas are treated as an infinite array of dislocations. The

solution to the b.v.p. is traditionally obtained using the finite-element method FEM. The rigid indenter is modeled implicitly by imposing boundary conditions on the deformable body.
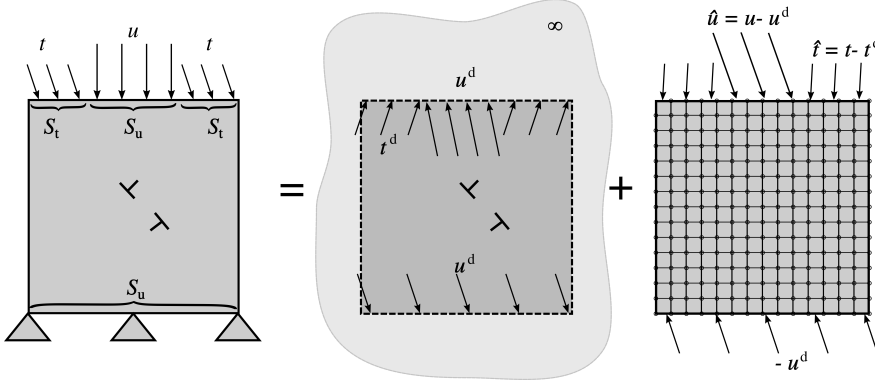
Figure 3.1: Schematic representation of the DDP methodology: The boundary-value problem for a body containing dislocations is decomposed into two parts: the fields of the dislocations in an infinite medium and the solution to the elastic boundary-value problem which corrects for the boundary conditions.

The total stress and displacement fields obtained at a given time increment are used, along with a set of constitutive rules, to describe the evolution of the dislocation structure. The constitutive rules are based on the Peach-Koehler force and control dislocation glide, nucleation, annihilation and pinning at obstacles. At the beginning of the simulation, the crystal is dislocation-free, but contains a density of point sources and obstacles that mimic Frank-Read sources and precipitates, respectively. The density of sources and obstacles is constant during the simulation. A dislocation pair is generated by a point source when the resolved shear stress acting on the source exceeds a critical nucleation strength, τ_{nuc}. The dislocation then glides on a plane with a velocity proportional to the Peach-Koehler force. Two dislocations with opposite Burgers vector annihilate when they come closer to each other than a threshold length, set to $6b$, where b is the magnitude of the Burgers vector. Whenever a dislocation meets an obstacle it gets pinned. It is released by the obstacle only when the Peach-Koehler force acting on the dislocation exceeds the critical strength of the obstacle, τ_{obs}. Dislocations can exit the domain through the free surface leaving behind a displacement step of $\pm b/2$ along the slip direction.

The aim of this work is to replace the FEM solution to the complementary b.v.p. with GFMD, while the constitutive rules that control the dislocation dynamics remain un-

changed and similar to those proposed in reference (van der Giessen and Needleman, 1995).

3.3. GREEN'S FUNCTION MOLECULAR DYNAMICS

GFMD is also a boundary-value method to study the elastic response of a body subjected to contact loading. In GFMD, only the surface of the deformable body is modeled explicitly and discretized using equi-spaced grid points as seen in figure 3.2. The grid points, under the influence of an external load, are displaced from their initial position, causing an increase in the areal elastic energy of the system. The new equilibrium positions are then calculated using damped dynamics in Fourier space. The advantage of damping the system in Fourier space is that the different modes describing the surface are uncoupled, and the stress-displacement relationship, when applying a load in z−direction, simply reads:

$$\tilde{u}_\alpha(\mathbf{q}) = \tilde{G}_{\alpha\beta}(\mathbf{q})\tilde{\sigma}_{z\beta}(\mathbf{q}), \tag{3.1}$$

where $G_{\alpha\beta}(\mathbf{q})$ is the Green's function tensor, $u_\alpha(\mathbf{q})$ is the α component of the displacement and and $\sigma_{z\beta}(\mathbf{q})$ is the traction in β−direction corresponding to wavenumber $\mathbf{q}$. The Green's function tensor depends on the elastic properties and size of the body.
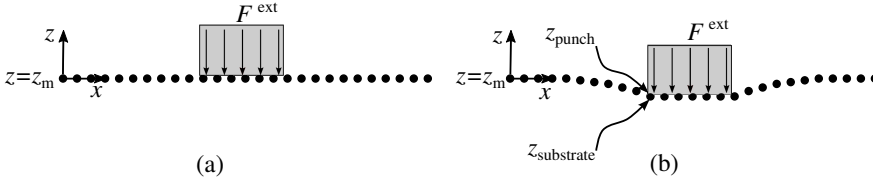
Figure 3.2: Schematic representation of a rigid punch indenting a flat deformable body: (a) the undeformed configuration and (b) the deformed configuration.

Here, the load is applied in an incremental manner by means of a rigid flat indenter, which is modeled by a hard wall potential. To satisfy static equilibrium at each incremental change of the loading, the following condition must hold:

$$\tilde{\boldsymbol{F}}^{\text{ext}}(q) + \tilde{\boldsymbol{F}}^{\text{el}}(q) + \tilde{\boldsymbol{F}}^{\text{if}}(q) = 0, \tag{3.2}$$

where $\tilde{\boldsymbol{F}}^{\text{ext}}(q)$ is the external force; $\tilde{\boldsymbol{F}}^{\text{if}}(q)$ is the interfacial force ensuring the non-overlap constraint, which are imposed "by hand" after each time step, in real space; $\tilde{\boldsymbol{F}}^{\text{el}}(q)$ is the

elastic restoring force that can be written as:

$$\tilde{\boldsymbol{F}}^{\mathrm{el}}(q)/A_0 = \tilde{\boldsymbol{G}}^{-1}(q)\tilde{\boldsymbol{u}}(q) = \nabla_{\tilde{u}}\,v_{\mathrm{el}}, \tag{3.3}$$

where A_0 is the total surface area and $\tilde{\boldsymbol{G}}^{-1}(q)$ is the inverse Green's function, which can be evaluated from the areal elastic energy density v_{el}. The areal elastic energy was derived for a slab with deformable top and fixed bottom in previous works (Carbone and Putignano, 2013; Venugopalan et al., 2017b). In section 4.1, we extend the derivation to the case where the bottom surface can be exposed to arbitrary stress, displacement, or mixed boundary condition. This is necessary for the coupling to dislocation dynamics, as should become clear in the following section.

The damping force has the form:

$$\tilde{\boldsymbol{F}}^{\mathrm{damp}}(q) = \eta(\tilde{\boldsymbol{u}}^{n-1}(q) - \tilde{\boldsymbol{u}}^{n}(q)) \tag{3.4}$$

where η is the damping factor, chosen such to critically damp the slowest mode, i.e., the center of mass mode, corresponding to $q = 0$, for quick convergence. Various further improvements can be applied to speed up convergence, such as, mode-dependent masses or damping. However, this was not pursued in this work, because even without these optimizations, the main computational time is related to the DDD part of the simulations.

The damping force is used in the position-Verlet algorithm to solve for the displacement fields at each increment $(n + 1)$,

$$\tilde{\boldsymbol{u}}^{n+1}(q) = 2\tilde{\boldsymbol{u}}^{n}(q) - \tilde{\boldsymbol{u}}^{n-1}(q) + \left(\tilde{\boldsymbol{F}}^{\mathrm{el}}(q) + \tilde{\boldsymbol{F}}^{\mathrm{ext}}(q) + \tilde{\boldsymbol{F}}^{\mathrm{damp}}(q)\right)\tau^2, \tag{3.5}$$

where τ is the non-dimensional discrete time step used in the simulation.

The hard-wall potential is employed at the end of each iteration to ensure there is no inter-penetration, $i.e.$, in real space,

$$z_{\mathrm{punch}}(x) \geq z_{\mathrm{substrate}}(x), \tag{3.6}$$

where z_{punch} and $z_{\mathrm{substrate}}$ are the z- coordinates of the punch and substrate surface, respectively as seen in the figure 3.2. Notice that the method is not bound to use a hard-wall potential. Finite interactions can be accounted for, however, we have here chosen

for a hard-wall potential for the sake of comparison to conventional DDP.

When the surface equilibrates to the final deformed configuration, the body fields are calculated from the discrete surface fields using closed-form analytical solutions (Venugopalan et al., 2017b).

3.4. GREEN'S FUNCTION DISLOCATION DYNAMICS

The Green's function dislocation dynamics method is based on the same decomposition concept as used in DDP except that, now, the image fields are found using GFMD instead of FEM. The methodology is schematically presented in figure 3.3 for the case of a layer indented using a flat rigid punch. Note that GFDD can solve generic boundary value problems where both top and bottom boundaries are arbitrarily partitioned into traction and displacement boundaries.
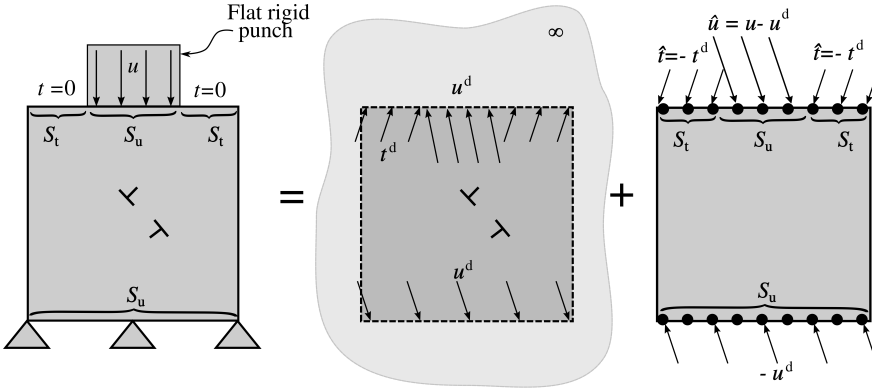
Figure 3.3: Decomposition of the problem for the dislocated body similar to figure 3.1 except for the complementary problem, which is solved using GFMD.

When solving the complementary b.v.p., both tractions and displacements caused by the dislocations on the top and bottom boundary of the body need to be simultaneously prescribed at a given time increment. Tractions are imposed in Fourier space as described in the previous section by using $\hat{t}(q)$ as external force $\tilde{F}^{\text{ext}}(q)$ before stepping forward in time. Here $\hat{t}(q)$ is the Fourier transformation of the discontinuous function $\hat{t}(r)$ at point $r = (x, z)$:

$$\hat{t}(r) = t(r) - t^{\text{d}}(r) \qquad \text{if } r \in S_{\text{t}},$$
$$\hat{t}(r) = 0 \qquad \text{if } r \in S_{\text{u}},$$

(3.7)

where S_t and S_u are traction- and displacement-prescribed boundaries, respectively. Unlike tractions, displacements are imposed in real space by setting the equilibrium position of the hard-wall to the required position:

$$\hat{\boldsymbol{u}}(\boldsymbol{r}) = \boldsymbol{u}(\boldsymbol{r}) - \boldsymbol{u}^{\mathrm{d}}(\boldsymbol{r}) \qquad \text{if } \boldsymbol{r} \in S_u. \tag{3.8}$$

The hard-wall is not applied to the boundaries where traction is prescribed S_t.

Notice that the elastic energy required for the evaluation of the Green's function, which is needed in the calculation of the restoring elastic force, was derived in (Venugopalan et al., 2017b) but only for the case of an isotropic slab with an undulated top layer and a fixed bottom. This allows a b.v.p. to be solved for a mixed boundary condition at the top, however, with the restriction of the bottom displacement to be zero. Here, however, we need to impose mixed boundary conditions also at the bottom. To this end, the areal elastic energy is required for a solid with both top and bottom undulation as seen in figure 3.4. This will be dealt with in the subsequent section.

3.4.1. ELASTIC ENERGY OF AN ELASTIC LAYER LOADED AT BOTH SURFACES

A linear elastic isotropic body in a slab geometry is considered. The equilibrium condition for the case of no body forces can be written as $\partial_\alpha \sigma_{\alpha\beta}(\boldsymbol{r}) = 0$, where $\sigma_{\alpha\beta}(\boldsymbol{r})$ is the stress at point (x, z) represented by vector $\boldsymbol{r}$ and $\partial_\alpha \equiv \partial/\partial r_\alpha$. This can be written as:

$$\begin{aligned}
[C_{11}\partial_x^2 + C_{44}\partial_z^2]u_x(\boldsymbol{r}) + (C_{44} + C_{12})\partial_x\partial_z u_z(\boldsymbol{r}) = 0, \\
[C_{11}\partial_z^2 + C_{44}\partial_x^2]u_z(\boldsymbol{r}) + (C_{44} + C_{12})\partial_z\partial_x u_x(\boldsymbol{r}) = 0,
\end{aligned} \tag{3.9}$$

where C_{ij} denotes the coefficients of the elastic tensor. The in-plane wavenumber q is a scalar for the two-dimensional body considered here.

It is shown in A that for the system of differential equations (3.9) the solutions of the in-plane cosine transform of the lateral u_x displacement field couples to the in-plane sine transform of the normal u_z displacement and vice versa. Thus, we can write:

$$\begin{aligned}
u_x^{\mathrm{c}}(x, z) = \cos(qx)\tilde{u}_x^{\mathrm{c}}(q, z), \\
u_z^{\mathrm{s}}(x, z) = \sin(qx)\tilde{u}_z^{\mathrm{s}}(q, z).
\end{aligned} \tag{3.10}$$
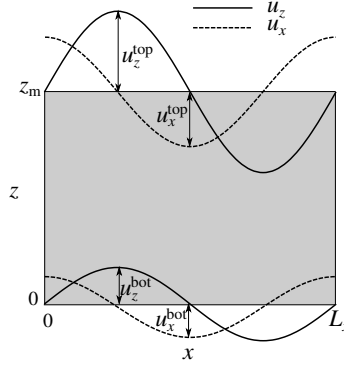
Figure 3.4: Periodic unit cell of an isotropic slab of height z_{m} represented by the shaded region is undulated at the top and bottom surfaces in lateral and normal directions.

Solutions satisfying the following boundary conditions:

$$
\begin{aligned}
\tilde{u}_x^{\mathrm{c}}(q,0) &= u_x^{\mathrm{bot}}, \\
\tilde{u}_z^{\mathrm{s}}(q,0) &= u_z^{\mathrm{bot}}, \\
\tilde{u}_x^{\mathrm{c}}(q,z_{\mathrm{m}}) &= u_x^{\mathrm{top}}, \\
\tilde{u}_z^{\mathrm{s}}(q,z_{\mathrm{m}}) &= u_z^{\mathrm{top}}
\end{aligned}
\tag{3.11}
$$

and equation (3.9) are then obtained to satisfy

$$
\begin{bmatrix} \tilde{u}_x^{\mathrm{c}}(q,z) \\ \tilde{u}_z^{\mathrm{s}}(q,z) \end{bmatrix} = \begin{bmatrix} h_1(q,z) & h_2(q,z) & -h_3(q,z) & -h_4(q,z) \\ h_3(q,z) & h_4(q,z) & h_5(q,z) & h_6(q,z) \end{bmatrix} \begin{bmatrix} A_1 \\ A_2 \\ A_3 \\ A_4 \end{bmatrix}
\tag{3.12}
$$

with

$$
\begin{aligned}
h_1(q,z) &= (1-r)\cosh(qz) + rqz\sinh(qz), \\
h_2(q,z) &= \sinh(qz) + rqz\cosh(qz), \\
h_3(q,z) &= r(qz\cosh(qz) - \sinh(qz)), \\
h_4(q,z) &= rqz\sinh(qz), \\
h_5(q,z) &= (1+r)\cosh(qz) - rqz\sinh(qz), \\
h_6(q,z) &= \sinh(qz) - rqz\cosh(qz),
\end{aligned}
\tag{3.13}
$$

where $r = \dfrac{1-s}{1+s}$ and $s = C_{44}/C_{11}$. A_i can be found by applying the boundary conditions in equation (3.11):

$$
\begin{bmatrix} A_1 \\ A_2 \\ A_3 \\ A_4 \end{bmatrix} = \frac{1}{f(q,z_m)} \begin{bmatrix} \dfrac{f(q,z_m)}{(1-r)} & 0 & 0 & 0 \\ k_1(q,z_m) & k_2(q,z_m) & k_3(q,z_m) & k_4(q,z_m) \\ 0 & \dfrac{f(q,z_m)}{(1+r)} & 0 & 0 \\ k_5(q,z_m) & k_6(q,z_m) & k_7(q,z_m) & k_8(q,z_m) \end{bmatrix} \begin{bmatrix} \tilde{u}_x^c(q,0) \\ \tilde{u}_z^s(q,0) \\ \tilde{u}_x^c(q,z_m) \\ \tilde{u}_z^s(q,z_m) \end{bmatrix} \tag{3.14}
$$

with

$$
\begin{aligned}
k_1(q,z_m) &= rqz_m - \sinh(qz_m)\cosh(qz_m), \\
k_2(q,z_m) &= -\frac{r}{1+r}(\cosh^2(qz_m) - 1 + r(qz_m)^2), \\
k_3(q,z_m) &= h_6(q,z_m), \\
k_4(q,z_m) &= h_4(q,z_m), \\
k_5(q,z_m) &= \frac{r}{1-r}(\cosh^2(qz_m) - 1 - r(qz_m)^2), \\
k_6(q,z_m) &= -rqz_m - \sinh(qz_m)\cosh(qz_m), \\
k_7(q,z_m) &= -h_4(q,z_m), \\
k_8(q,z_m) &= h_2(q,z_m),
\end{aligned} \tag{3.15}
$$

and

$$
\begin{aligned}
f(q,z_m) &= \cosh^2(qz_m) - (rqz_m)^2 - 1 \\
&= \frac{1}{2}\left\{\cosh(2qz_m) - 2(rqz_m)^2 - 1\right\}.
\end{aligned} \tag{3.16}
$$

Similarly, the in-plane sine transform of u_x and cosine transform of u_z can be obtained from:

$$
\begin{bmatrix} \tilde{u}_x^s(q,z) \\ \tilde{u}_z^c(q,z) \end{bmatrix} = \begin{bmatrix} h_1(q,z) & h_2(q,z) & h_3(q,z) & h_4(q,z) \\ -h_3(q,z) & -h_4(q,z) & h_5(q,z) & h_6(q,z) \end{bmatrix} \begin{bmatrix} B_1 \\ B_2 \\ B_3 \\ B_4 \end{bmatrix} \tag{3.17}
$$

with

$$
\begin{bmatrix} B_1 \\ B_2 \\ B_3 \\ B_4 \end{bmatrix} = \frac{1}{f(q,z_m)} \begin{bmatrix} \dfrac{f(q,z_m)}{(1-r)} & 0 & 0 & 0 \\ k_1(qz_m) & -k_2(qz_m) & k_3(qz_m) & -k_4(qz_m) \\ 0 & \dfrac{f(q,z_m)}{(1+r)} & 0 & 0 \\ -k_5(qz_m) & k_6(qz_m) & -k_7(qz_m) & k_8(qz_m) \end{bmatrix} \begin{bmatrix} \tilde{u}_x^s(q,0) \\ \tilde{u}_z^c(q,0) \\ \tilde{u}_x^s(q,z_m) \\ \tilde{u}_z^c(q,z_m) \end{bmatrix}. \quad (3.18)
$$

From equation (3.12), the strains are calculated as:

$$
\begin{aligned}
\tilde{\epsilon}_{xx}^s(q,z) &= -q\tilde{u}_x^c(q,z), \\
\tilde{\epsilon}_{zz}^s(q,z) &= \partial_z \tilde{u}_z^s(q,z), \\
\tilde{\epsilon}_{xz}^c(q,z) &= \partial_z \tilde{u}_x^c(q,z) + q\tilde{u}_z^s(q,z).
\end{aligned} \quad (3.19)
$$

Stresses are then obtained as usual through Hooke's law:

$$
\sigma_i = C_{ij}\epsilon_j. \quad (3.20)
$$

Gathering all contributions to the elastic energy leads to

$$
\begin{aligned}
v_{el} = \frac{C_{11}q}{2} \Big[& s\tilde{\epsilon}_{xz}^c(q,z_m)\tilde{u}_x^c(q,z_m) + \big\{ \tilde{\epsilon}_{zz}^s(q,z_m) + (1-2s)\tilde{\epsilon}_{xx}^s(q,z_m) \big\} \tilde{u}_z^s(q,z_m) \\
& + s\tilde{\epsilon}_{xz}^c(q,0)\tilde{u}_x^c(q,0) + \big\{ \tilde{\epsilon}_{zz}^s(q,0) + (1-2s)\tilde{\epsilon}_{xx}^s(q,0) \big\} \tilde{u}_z^s(q,0) \Big]
\end{aligned}
$$

$$
= \frac{C_{11}q}{2} \begin{bmatrix} \tilde{u}_x^c(q,0) & \tilde{u}_z^s(q,0) & \tilde{u}_x^c(q,z_m) & \tilde{u}_z^s(q,z_m) \end{bmatrix} \begin{bmatrix} H_{ij}(q,z_m) \end{bmatrix} \begin{bmatrix} \tilde{u}_x^c(q,0) \\ \tilde{u}_z^s(q,0) \\ \tilde{u}_x^c(q,z_m) \\ \tilde{u}_z^s(q,z_m) \end{bmatrix} \quad (3.21)
$$

with

$$H_{11}(q, z_{\mathrm{m}}) = H_{33}(q, z_{\mathrm{m}}) = (1 - r)\frac{\sinh(qz_{\mathrm{m}})\cosh(qz_{\mathrm{m}}) - rqz_{\mathrm{m}}}{f(q, z_{\mathrm{m}})}$$

$$-H_{12}(qz_{\mathrm{m}}) = H_{34}(qz_{\mathrm{m}}) = \frac{1 - r}{1 + r}\frac{(1 - r)\sinh^2(qz_{\mathrm{m}}) - 2(rqz_{\mathrm{m}})^2}{f(q, z_{\mathrm{m}})},$$

$$H_{13}(q, z_{\mathrm{m}}) = (1 - r)\frac{rqz_{\mathrm{m}}\cosh(q, z_{\mathrm{m}}) - \sinh(qz_{\mathrm{m}})}{f(q, z_{\mathrm{m}})},$$

$$-H_{14}(q, z_{\mathrm{m}}) = H_{23}(q, z_{\mathrm{m}}) = (1 - r)\frac{rqz_{\mathrm{m}}\sinh(qz_{\mathrm{m}})}{f(q, z_{\mathrm{m}})},$$

$$H_{22}(q, z_{\mathrm{m}}) = H_{44}(q, z_{\mathrm{m}}) = (1 - r)\frac{\sinh(qz_{\mathrm{m}})\cosh(qz_{\mathrm{m}}) + rqz_{\mathrm{m}}}{f(q, z_{\mathrm{m}})},$$

$$H_{24}(q, z_{\mathrm{m}}) = -(1 - r)\frac{rqz_{\mathrm{m}}\cosh(q, z_{\mathrm{m}}) + \sinh(qz_{\mathrm{m}})}{f(qz_{\mathrm{m}})}.$$

(3.22)

The complete elastic energy density containing the complex Fourier transform of the displacement with wavenumber q reads

$$v_{\mathrm{el}} = \sum_q \frac{C_{11}q}{2}\begin{bmatrix} \tilde{u}_x^*(q, 0) & \tilde{u}_z^*(q, 0) & \tilde{u}_x^*(q, z_{\mathrm{m}}) & \tilde{u}_z^*(q, z_{\mathrm{m}}) \end{bmatrix}\begin{bmatrix} H_{ij}(q, z_{\mathrm{m}}) \end{bmatrix}\begin{bmatrix} \tilde{u}_x(q, 0) \\ \tilde{u}_z(q, 0) \\ \tilde{u}_x(q, z_{\mathrm{m}}) \\ \tilde{u}_z(q, z_{\mathrm{m}}) \end{bmatrix}$$

(3.23)

with

$$\begin{bmatrix} H_{ij}(q, z_{\mathrm{m}}) \end{bmatrix} = \begin{bmatrix} H_{11}(q, z_{\mathrm{m}}) & -iH_{12}(q, z_{\mathrm{m}}) & -iH_{13}(q, z_{\mathrm{m}}) & -iH_{14}(q, z_{\mathrm{m}}) \\ iH_{21}(q, z_{\mathrm{m}}) & H_{22}(q, z_{\mathrm{m}}) & -iH_{23}(q, z_{\mathrm{m}}) & -iH_{24}(q, z_{\mathrm{m}}) \\ iH_{31}(q, z_{\mathrm{m}}) & iH_{32}(q, z_{\mathrm{m}}) & H_{33}(q, z_{\mathrm{m}}) & -iH_{34}(q, z_{\mathrm{m}}) \\ iH_{41}(q, z_{\mathrm{m}}) & iH_{42}(q, z_{\mathrm{m}}) & iH_{43}(q, z_{\mathrm{m}}) & H_{44}(q, z_{\mathrm{m}}) \end{bmatrix}. \quad (3.24)$$

The body fields are obtained through the closed-form analytical expressions in equation (3.12) and (3.17). The displacement fields hence obtained are compared with those obtained by FEM in figures 3.5 and 3.6. The relative difference in the displacement field obtained using both methods are found to be below 0.25 %. It has to be noted that peri-

odic boundary conditions in GFMD are intrinsically enforced through the periodicity of the Fourier transforms. In FEM, periodicity can be imposed using various methods, including the penalty method, as done in this study, or Lagrangian multipliers, but is never exact.
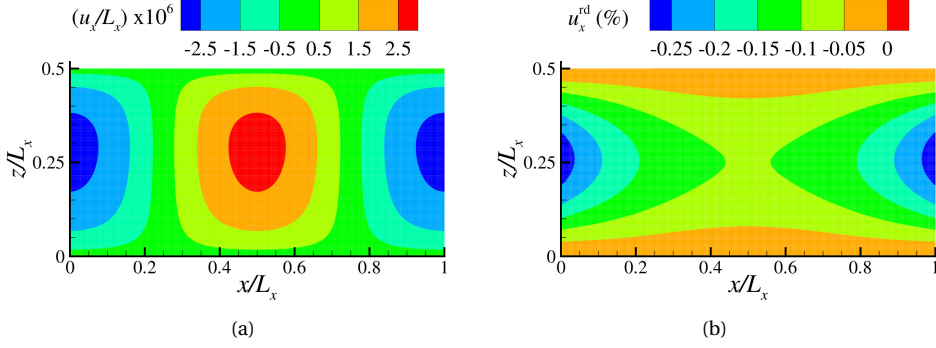

(a)   (b)

Figure 3.5: Lateral displacement u_x in an elastic layer with undulations $u_x^{\text{bot}}/L_x = 0$, $u_z^{\text{bot}}/L_x = \frac{0.5 \times 10^{-4}}{12}$, $u_x^{\text{top}}/L_x = 0$ and $u_z^{\text{top}}/L_x = \frac{1 \times 10^{-4}}{12}$ obtained using (a) GFMD and (b) the relative difference map with
$$u_x^{\text{rd}} = \left(\frac{u_x^{\text{GFMD}} - u_x^{\text{FEM}}}{u_z^{\text{top}}} \times 100 \right)\%.$$

(a)   (b)

Figure 3.6: Normal displacement u_z in an elastic layer with undulations $u_x^{\text{bot}}/L_x = 0$, $u_z^{\text{bot}}/L_x = \frac{0.5 \times 10^{-4}}{12}$, $u_x^{\text{top}}/L_x = 0$ and $u_z^{\text{top}}/L_x = \frac{1 \times 10^{-4}}{12}$ obtained using (a) GFMD and (b) the relative difference map with
$$u_z^{\text{rd}} = \left(\frac{u_z^{\text{GFMD}} - u_z^{\text{FEM}}}{u_z^{\text{top}}} \times 100 \right)\%.$$

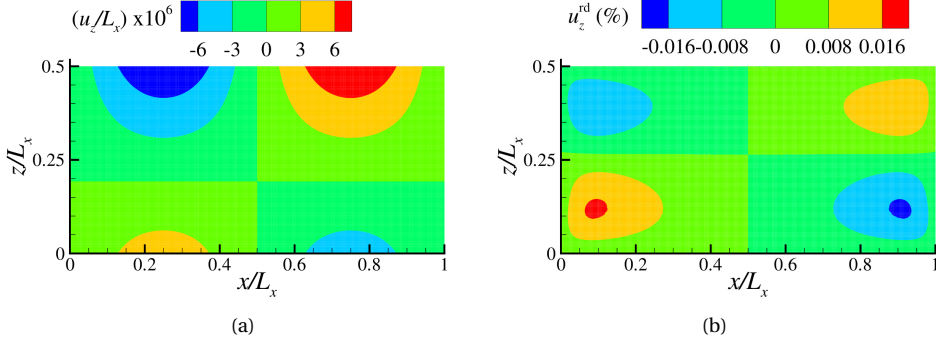The elastic energy density in equation (3.23) is extended to the case of a semi-infinite half-space in B. This opens up the possibility of modeling the plastic contact response of a semi-infinite body using dislocation-dynamics simulations. This is beneficial to study

the plastic response of a body under contact loading without the effect of its bottom, *i.e.,* an increase in contact pressure caused by dislocations piling up at the bottom of the body.

3.5. PRELIMINARY RESULTS: A SIMPLE STATIC SOLUTION

In this section, the new GFDD model is compared to DDP when computing the image fields for the simplest case scenario: a single dislocation pinned in an isotropic slab with Young's modulus $E = 70$ GPa and Poisson's ratio $\nu = 0.33$. The magnitude of the Burger's vector is $b = 0.25$ nm.

Simulations are carried out for a unit cell with the bottom fixed and a traction free top surface, *i.e.,*

$$u_x(x,0) = u_z(x,0) = 0,$$
$$\sigma_{xz}(x,z_{\mathrm{m}}) = \sigma_{zz}(x,z_{\mathrm{m}}) = 0. \tag{3.25}$$

The stress distribution obtained using GFDD is compared with DDP in figure 3.7. The displacements at the top surface, where tractions are zero, and the tractions at the bottom surface, where displacement are zero, are shown in figure 3.8 and figure 3.9.
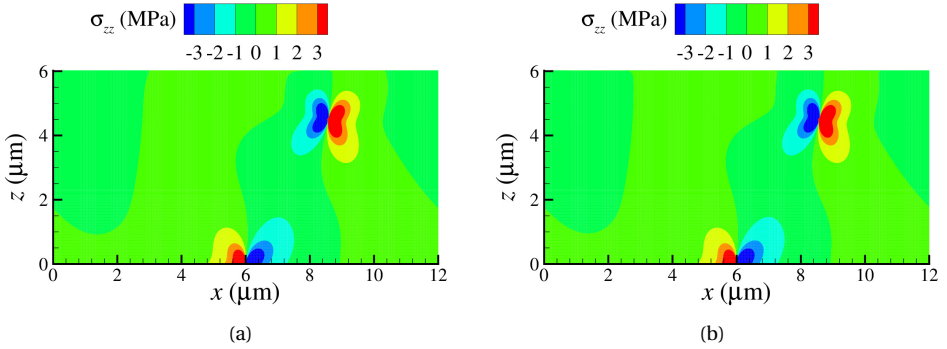
Figure 3.7: Stress fields for a dislocated elastic layer with a traction free top surface obtained using (a) GFDD and (b) DDP.

It is found that the tractions at the surface obtained using GFDD suffer from ringing, also known as Gibb's phenomenon (see figure 3.10). This is because the discontinuities in the displacement imposed at the surfaces cause the higher harmonics of the traction
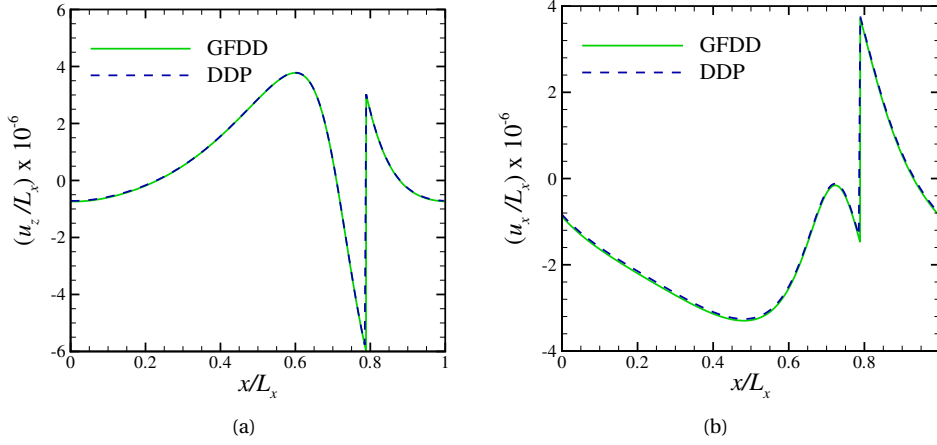
Figure 3.8: (a) Normal displacement u_z and (b) lateral displacement u_x at the traction free surface of an elastic layer containing a pinned edge dislocation obtained using GFDD and DDP.
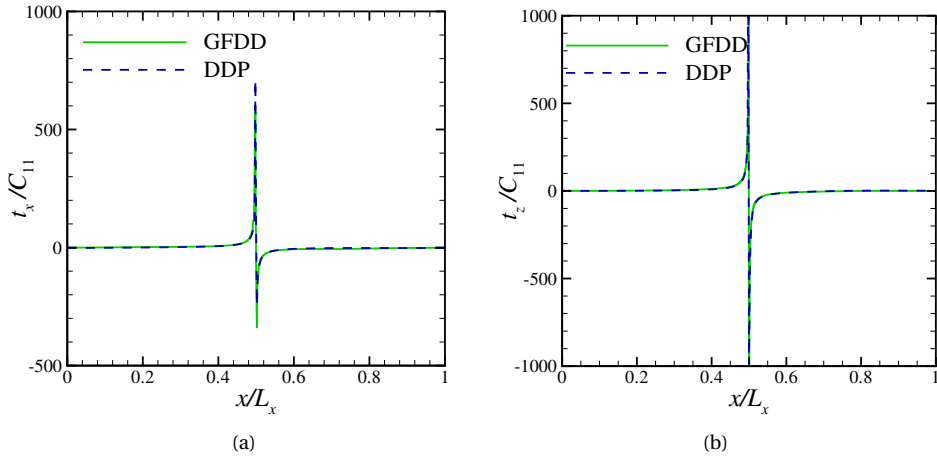
Figure 3.9: (a) Lateral traction t_x and (b) normal traction t_z at the bottom surface of the elastic layer containing a pinned edge dislocation obtained using GFDD and DDP.
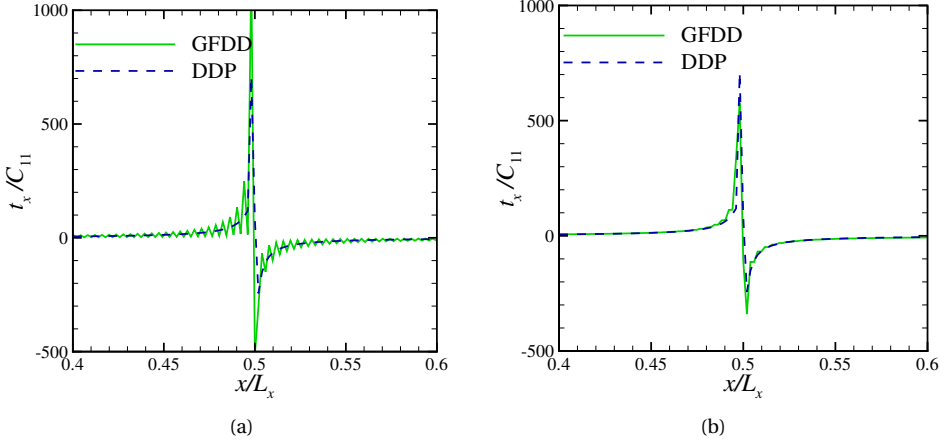
Figure 3.10: Lateral traction t_x at the bottom surface (a) before and (b) after the removal of ringing artifacts.

to have higher amplitudes than the lower harmonics. To remove the ringing artifacts the results displayed in figure 3.9 are obtained after multiplying the traction $\boldsymbol{t}(q)$ with a sinc function $\mathrm{sinc}(qa_0)$, where a_0 is the discretization length. This is equivalent to convolving in real space the traction suffering from ringing with a rectangular box of unit height and width equal to the discretization length. Notice, however, that ringing affects only surface tractions, not surface displacements, from which the body fields are calculated.

3.6. INDENTATION BY AN ARRAY OF FLAT RIGID PUNCHES

This benchmark problem is used to compare GFDD to classical DDP. The simulations are carried out for a unit cell that is indented by a rigid punch as in figure 3.11.
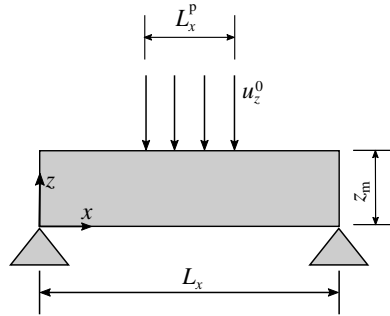
Figure 3.11: Boundary-value problem.

3.6.1. BOUNDARY-VALUE PROBLEM

The indentation is prescribed by specifying the normal displacement rate along the contact of length L_x^{p}:

$$\dot{u}_z(x, z_{\mathrm{m}}) = -\dot{u}_z^0, \quad x \in \left[\frac{L_x - L_x^{\mathrm{p}}}{2}, \frac{L_x + L_x^{\mathrm{p}}}{2} \right].$$

A sticking contact is modeled in DDP by taking the lateral displacement $u_x = 0$ in the contact region. In GFDD, the lateral movement in the contact region is constrained horizontally through the hard-wall potential. The non-contact part of the top surface of the unit cell is taken to be traction-free,

$$\sigma_{xz}(x, z_{\mathrm{m}}) = \sigma_{zz}(x, z_{\mathrm{m}}) = 0.$$

This is achieved in GFDD by letting the contact points relax to equilibrium without any constraints. Finally, the bottom of the unit cell, $z = 0$ is fixed:

$$u_x(x, 0) = u_z(x, 0) = 0.$$

In GFDD, this is implemented by constraining the lateral and normal motion of grid points at the bottom surface using the hard-wall potential.

3.6.2. CHOICE OF PARAMETERS

Calculations are carried out for crystals with aspect ratio $a = z_{\mathrm{m}}/L_x = 1/2$, contact fractions $L_x^{\mathrm{p}}/L_x = 1/12$ and $L_x = 12\ \mu\mathrm{m}$. The elastic constants are chosen to represent aluminum: the Young's modulus is $E = 70$ GPa and Poisson's ratio $\nu = 0.33$.

For the DDP simulations, the slab is discretized using a uniform mesh of square elements. The number of degrees of freedom is $n_{\mathrm{dof}} = 2nnx \times nnz$, where nnx is the number of nodes in x-direction, and nnz the number of nodes in z-direction. For the GFDD simulations, the surface is discretized using nx equi-spaced grid points, with $nx = nnx$.

In GFDD, the center-of-mass mode is critically damped or slightly under-damped for quick convergence. The damping factor η is

$$\eta \propto \frac{1}{\tau \sqrt{nx}}, \tag{3.26}$$

where τ is the non-dimensional time step shown earlier in equation (3.5) that is used in the position-Verlet algorithm in GFMD to solve for the unknown displacement fields and it is taken to be τ=0.25. The number of iterations used to reach convergence scales as $n_{\text{it}} \propto \sqrt{a\,nx}$.

The dislocations can glide on three sets of parallel slip planes, with slip plane orientations: 0°, 60° and 120° to the top surface. The discrete slip planes are spaced at $200b$ where $b = 0.25$ nm is the length of the Burger's vector. The Frank-Read sources and obstacles are randomly distributed in the crystal with a density $\rho_{\text{nuc}} = 30\ \mu\text{m}^{-2}$ and $\rho_{\text{obs}} = 30\ \mu\text{m}^{-2}$ in an initially dislocation free crystal. The strength of the sources follows a Gaussian distribution with mean strength $\tau_{\text{nuc}} = 50$ MPa and standard deviation of 10 MPa. The critical time for nucleation is $t_{\text{nuc}} = 1$ ns. The strength of the obstacles is taken to be 150 MPa. Dislocations of opposite sign in the same slip plane annihilate when the distance between them is below $L_{\text{ann}} = 6b$. The time step in both DDP and GFDD simulations is taken to be $\Delta t = 2.5$ ns.

3.6.3. A SIMPLE DISLOCATION DYNAMIC SIMULATION: A SINGLE FRANK-READ SOURCE

In this section, a simple problem is considered where a rigid flat punch indents a crystal containing a single Frank-Read source as shown in figure 3.12(a). In order to observe appreciable plastic deformation in the material, the magnitude of the Burger's vector is magnified four times, $i.e.$, $b = 1.0$ nm. The mean contact pressure obtained using both methods is displayed in figure 3.12(b). While the flat rigid punch indents the layer, the source keeps generating dislocation dipoles, causing periodic kinks in the pressure-displacement curve. The difference in mean contact pressure in figure 3.12(b) is not seen to the naked eye.

The surface fields obtained using both methods at $u_z = 0.01\mu$m are shown in figure 3.13. The displacement steps formed due to the exiting of dislocations can be clearly seen close to $x/L_x = 0.6$.

Note that in figure 3.13(a) the curves for the u_z displacement overlap since in z–direction displacement boundary conditions are imposed. The difference between the curves representing u_x stems from the numerical difference in calculating the resolved shear stress acting on the source and the location of the dislocations in the two numeri-
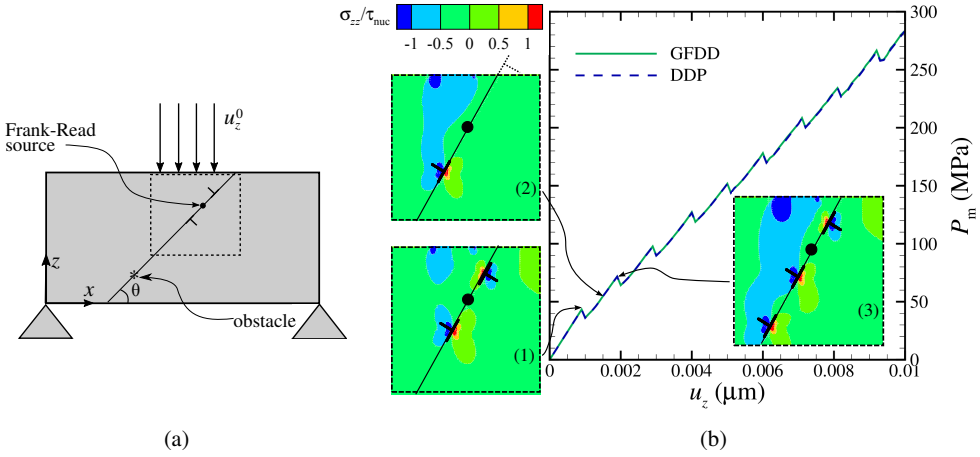
Figure 3.12: (a) Schematic representation of the problem with a single Frank-Read source lying on a slip plane at an angle θ with the surface of the crystal. (b) Mean contact pressure for $nx = nnx = 256$. The dislocation structure and stress distribution is shown at three different depth of indentations: (1) when the first pair of dislocation is nucleated, (2) when the first dislocation exits and (3) when the second dipole is nucleated.

cal schemes. The calculated stress field depends not only on boundary conditions when the simulation is elastic, but also on the location of other dislocations in the crystal when there is plasticity. Therefore, the differences builds up with increasing dislocation density. However, relative differences between contact pressure claculated in 3.13(b) with two methods remain below 0.45%.

3.6.4. DISLOCATION DYNAMICS SIMULATION WITH MANY SOURCES AND OB- STACLES

In this section the indented crystals contain a density of Frank-Read sources $\rho_{\text{nuc}} = 30 \ \mu\text{m}^{-2}$ and a density of obstacles $\rho_{\text{obs}} = 30 \ \mu\text{m}^{-2}$. The simulations are carried out with DDP and GFDD on crystals containing the same realization of sources and obstacles, *i.e.*, the location as well as the strength of sources and obstacles are identical. Figure 3.15 shows the stress state and dislocation distribution at final indentation depth. Note that there is no one-to-one correspondence between the dislocations and therefore also not in terms of stress distribution. This is not surprising given that a tiny difference in the evolution of the dislocation structure, like a small delay in the nucleation of a dislocation or in the formation of a junction, would trigger an avalanche of differences in the following dislocation dynamics (Deshpande et al., 2001). The overall features such as the shear
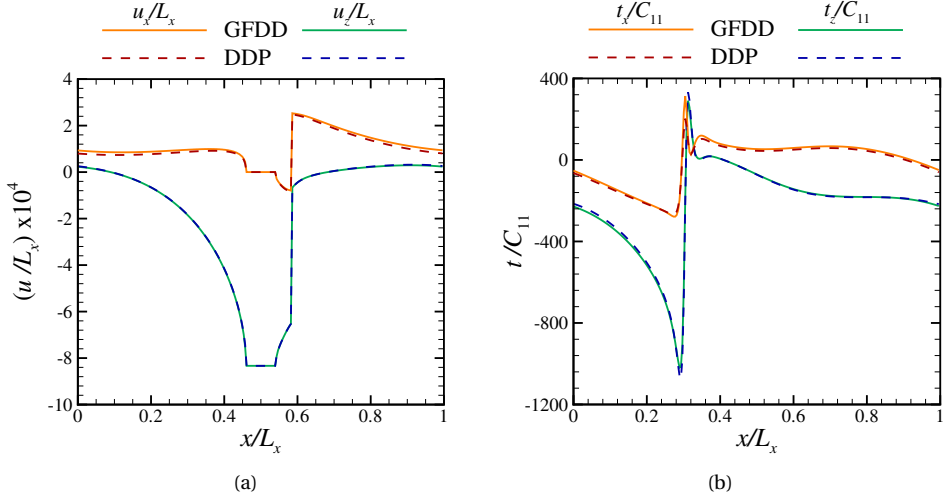
Figure 3.13: (a) Displacement at the top surface and (b) traction at the bottom surface obtained using GFDD and DDP at the final indentation depth $u_z = 0.01$ μm. The green curve in (a) overlaps with the blue-dashed curve since displacement boundary conditions are prescribed in the z–direction.

bands emitted by the contact are captured by both methods in the same way. This is also testified by the mean contact pressure in figure 3.14(a) for the simulation presented in figure 3.15 and for a different realization. While DDP and GFDD do not produce identical mean pressures as a function of displacement for a given realization of Frank-Read sources, differences tend to be larger within one method from one realization to the next. In figure 3.14(b) are presented the average between the two realizations.

3.6.5. SIMULATION TIME

The computational complexity involved in solving the elastic b.v.p. using GFDD is only $O(nx\sqrt{nx} \log nx)$ (Venugopalan et al., 2017b), while it is $O(nx^2B^2)$ (Synn and Fulton, 1995) in DDP, where B is the mean bandwidth of the stiffness matrix, which cannot exceed nx.

The time consuming part in 2D dislocation dynamics is the calculation of the resolved shear stress τ_{res} at the location of objects, *i.e.*, sources, dislocations and obstacles. In DDP, this requires searching the element where the object is located and subsequently calculating the stress and interpolating it to the location of the object. This procedure scales as $O(nx^2)$. In GFDD, instead, the resolved shear stress can be evalu-

(a)   (b)
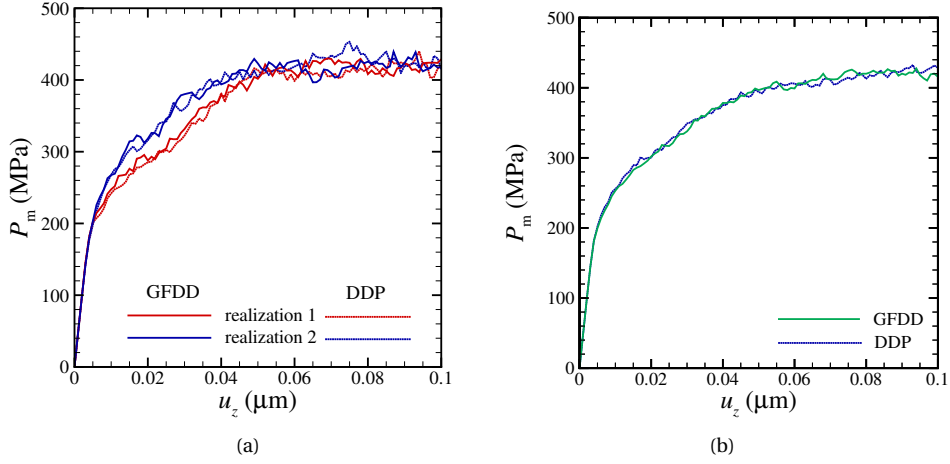
Figure 3.14: Mean contact pressure P_m obtained using GFDD and DDP for $nx = nnx = 512$ are plotted for (a) two different initial realizations of dislocation structure and (b) average of three different realizations.

(a)   (b)
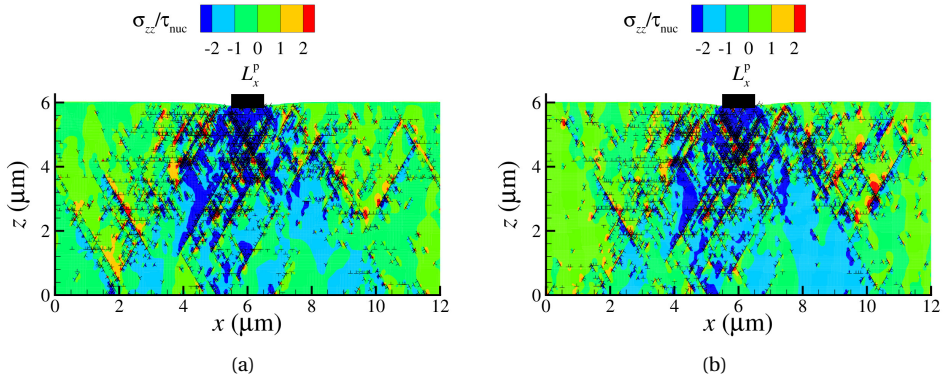
Figure 3.15: Stress and dislocation distribution in the crystal for the first realization obtained using (a) GFDD and (b) DDP for an indentation depth $u_z = 0.1$ μm and $nx = nnx = 512$.

ated directly at the points of interest, *i.e.*, at dislocations, sources and obstacles, which requires a smaller computational effort, scaling with $O(nx)$. This is because the body field is calculated based on surface displacements $\bar{\boldsymbol{u}}(q)$ using $nx/2$ modes.

The simulation time required for elasticity and for the calculation of the resolved shear stress is displayed in figure 3.16, and shows in both cases how the computational advantage of using GFDD increases with increasing discretization. It has to be noted that we use a skyline solver for FEM. The computational time using this solver was found to be of the same order as that of iterative solvers. The simulations performed on a single Intel Xeon(R) 3.10 GHz processor with 31.3 GB of RAM.

The dislocation dynamics is computed using the same algorithm in both methods and takes therefore the same amount of time and resources. The time required for the dynamics is independent of the discretization and increases with dislocation density. For the DDP simulations performed here, the time consumed by the dislocation dynamics is a negligible fraction of the time required to compute the resolved shear stress. GFDD is thus computationally more efficient than DDP independently of dislocation density.
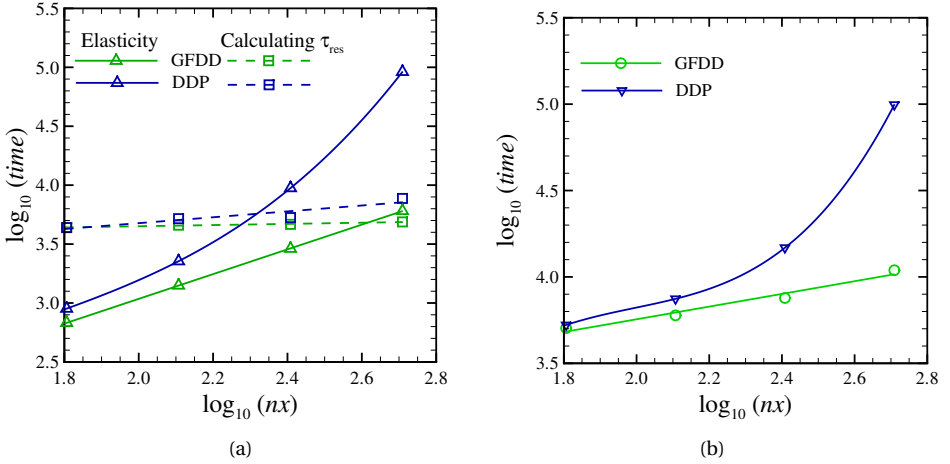
Figure 3.16: (a) Simulation time (in seconds) for the elastic boundary-value problem and calculating resolved shear stress τ_{res} are plotted separately, (b) total simulation time including dislocation dynamics for GFDD vs DDP for the full simulation.

It has to be noted that the maximum number of surface nodes chosen for this study is only 2^9. If one intends to study the contact response of a realistic self-affine surface where roughness scales over three orders of magnitude ranging in scale from 50 nm to

100 μm (Plouraboué and Boehm, 1999), the surface has to be discretized by at least 2^{13} points (or even more depending on the thermodynamic and continuum limit (Prodanov et al., 2014)). For such large systems, and small strain simulations, as typically used in dislocation dynamics, the computational complexity for elastic b.v.p. was found to always dominate in comparison to the dislocation dynamics. In this case the computational advantage of GFDD becomes even more appreciable.

Notice also that the benchmark problem chosen in this work involves a constant contact area. For contact problems where the area is not constant, DDP becomes even slower since finding the correct contact area by means of the FEM requires many iterations as well as updating the boundary conditions at each time increment. GFDD is inherently impervious to such issues since it employs an interaction potential between the contacting surfaces.

3.7. CONCLUDING REMARKS

In this work, we propose a modeling technique, Green's function dislocation dynamics, which combines Green's function molecular dynamics with discrete dislocation plasticity. We firstly extended the existing Green's function molecular dynamics model such that it can simulate an elastic layer with arbitrary loading at both the top and bottom surfaces. To this end we derived the areal elastic energy for the case of an isotropic layer with sinusoidal loading at both ends. In addition, we derived the body fields required to capture the evolution of the dislocation structure. The results obtained using GFDD are compared with conventional DDP for a benchmark problem: periodic indentation of a single crystal by flat punches.

The mean contact pressure during indentation using the two methods is found to differ less than two different realizations using the same method. Here by realization is intended a given initial distribution of dislocation sources and obstacles. The differences between the two methods stems from the evaluation of the fields using different discretizations: GFDD discretizes only the surface, DDP also the body.

The new GFDD model has various advantages compared to classical DDP. First, it is faster and opens up the possibility of studying realistic rough surfaces by exploiting a larger number of degrees of freedom. Next, GFDD employs an interaction potential between the contacting bodies, and does not involve time-consuming algorithms to keep

track of the evolution of the contact area. Also, the periodicity in GFDD is intrinsically enforced through Fourier transforms, making it a better candidate than DDP to study contact problems by exploiting the periodicity of the unit cell on which the analysis is performed. Obviously, this is also a limitation of the GFDD model, which is currently not suitable to study non-periodic problems. Extension of the model to overcome this limitation seems an interesting avenue for future research. Additionally, the GFDD model has the potential to serve as a platform for multi-scale modeling where the surface has an explicit atomistic description and the bulk can be treated as a dislocated continuum.

ACKNOWLEDGEMENT

REFERENCES

Almqvist, A., Sahlin, F., Larsson, R., Glavatskih, S., 2007. On the dry elasto-plastic contact of nominally flat surfaces. Tribology International 40 (4), 574 – 579, nORDTRIB 2004.

Archard, J. F., 1957. Elastic deformation and the laws of friction. Proceedings of the Royal Society of London A: Mathematical, Physical and Engineering Sciences 243 (1233), 190–205.

Balint, D., Deshpande, V., Needleman, A., der Giessen, E. V., 2006. Discrete dislocation plasticity analysis of the wedge indentation of films. Journal of the Mechanics and Physics of Solids 54 (11), 2281 – 2303.

Bush, A., Gibson, R., Thomas, T., 1975. The elastic contact of a rough surface. Wear 35 (1), 87 – 111.

Campañá, C., Müser, M., Denniston, C., Qi, Y., Perry, T., 2007. Elucidating the contact mechanics of aluminum silicon surfaces with green's function molecular dynamics. Journal of Applied Physics 102 (11).

Campañá, C., Müser, M. H., 2007. Contact mechanics of real vs. randomly rough surfaces: A green's function molecular dynamics study. EPL (Europhysics Letters) 77 (3), 38005.

Campañá, C., Müser, M. H., Robbins, M. O., 2008. Elastic contact between self-affine surfaces: comparison of numerical stress and contact correlation functions with analytic predictions. Journal of Physics: Condensed Matter 20 (35), 354013.

Carbone, G., Putignano, C., 2013. A novel methodology to predict sliding and rolling friction of viscoelastic materials: Theory and experiments. Journal of the Mechanics and Physics of Solids 61 (8), 1822 – 1834.

Dapp, W., Prodanov, N., Müser, M., 2014. Systematic analysis of persson's contact mechanics theory of randomly rough elasticsurfaces. Journal of Physics Condensed Matter 26 (35).

Deshpande, V. S., Needleman, A., Van der Giessen, E., 2001. Dislocation dynamics is chaotic. Scripta Materialia 45, 1047–1053.

El-Awady, J. A., Biner, S. B., Ghoniem, N. M., 2008. A self-consistent boundary element, parametric dislocation dynamics formulation of plastic flow in finite volumes. Journal of the Mechanics and Physics of Solids 56 (5), 2019 – 2035.

El-Awady, J. A., Wen, M., Ghoniem, N. M., 2009. The role of the weakest-link mechanism in controlling the plasticity of micropillars. Journal of the Mechanics and Physics of Solids 57 (1), 32 – 50.

Fleck, N., Muller, G., Ashby, M., Hutchinson, J., 1994. Strain gradient plasticity: Theory and experiment. Acta Metallurgica et Materialia 42 (2), 475 – 487.

Greenwood, J. A., Williamson, J. B. P., 1966. Contact of nominally flat surfaces. Proceedings of the Royal Society of London A: Mathematical, Physical and Engineering Sciences A295 (300).

Greer, J. R., Oliver, W. C., Nix, W. D., 2005. Size dependence of mechanical properties of gold at the micron scale in the absence of strain gradients. Acta Materialia 53 (6), 1821 – 1830.

Kajita, S., 2016. Green's function nonequilibrium molecular dynamics method for solid surfaces and interfaces. Phys Rev E 94, 033301.

Kogut, L., Etsion, I., 2002. Elastic-plastic contact analysis of a sphere and a rigid flat. Journal of Applied Mechanics 69, 657.

Ma, Q., Clarke, D. R., Apr. 1995. Size dependent hardness of silver single crystals. Journal of Materials Research 10, 853–863.

Mo, Y., Turner, K., Szlufarska, I., 2009. Friction laws at the nanoscale. Nature 457 (7233), 1116–1119.

Ng, W. S. K., Nicola, L., 2016a. Contact between two plastically deformable crystals: a discrete dislocation dynamics study. Philosophical Magazine 96, 2583–2599.

Ng, W. S. K., Nicola, L., 2016b. Discrete dislocation plasticity analysis of contact between deformable bodies with simple geometry. Modelling and Simulation in Materials Science and Engineering 24 (4).

Nicola, L., Bower, A., Kim, K.-S., Needleman, A., Van der Giessen, E., 2007. Surface versus bulk nucleation of dislocations during contact. Journal of the Mechanics and Physics of Solids 55 (6), 1120–1144.

Nicola, L., Bower, A., Kim, K.-S., Needleman, A., Van Der Giessen, E., 2008. Multi-asperity contact: A comparison between discrete dislocation and crystal plasticity predictions. Philosophical Magazine 88 (30-32), 3713–3729.

Nicola, L., Xiang, Y., Vlassak, J., der Giessen, E. V., Needleman, A., 2006a. Plastic deformation of freestanding thin films: Experiments and modeling. Journal of the Mechanics and Physics of Solids 54 (10), 2089 – 2110.

Nicola, L., Xiang, Y., Vlassak, J. J., Van der Giessen, E., Needleman, A., 2006b. Plastic deformation of freestanding thin films: experiments and modeling. Journal of the Mechanics and Physics of Solids 54 (10), 2089–2110.

Pastewka, L., Prodanov, N., Lorenz, B., Müser, M. H., Robbins, M. O., Persson, B. N. J., Jun 2013. Finite-size scaling in the interfacial stiffness of rough elastic contacts. Phys. Rev. E 87, 062809.

Pastewka, L., Robbins, M. O., 2014. Contact between rough surfaces and a criterion for macroscopic adhesion. Proceedings of the National Academy of Sciences 111 (9), 3298–3303.

Pastewka, L., Sharp, T. A., Robbins, M. O., 2012. Seamless elastic boundaries for atomistic calculations. Physical Review B 86 (7), 075459.

Pei, L., Hyun, S., Molinari, J., Robbins, M. O., 2005. Finite element modeling of elasto-plastic contact between rough surfaces. Journal of the Mechanics and Physics of Solids 53 (11), 2385 – 2409.

Persson, B., 2006. Contact mechanics for randomly rough surfaces. Surf. Sci. Rep. 61 (4), 201–227.

Persson, B. N., 2001. Theory of rubber friction and contact mechanics. The Journal of Chemical Physics 115 (8), 3840–3861.

Persson, B. N. J., 2008. On the elastic energy and stress correlation in the contact between elastic solids with randomly rough surfaces. Journal of Physics: Condensed Matter 20 (31), 312001.

Plouraboué, F., Boehm, M., 1999. Multi-scale roughness transfer in cold metal rolling. Tribology International 32 (1), 45 – 57.

Prodanov, N., Dapp, W. B., Müser, M. H., 2014. On the contact area and mean gap of rough, elastic contacts: Dimensional analysis, numerical corrections, and reference data. Tribology Letters 53 (2), 433–448.

Putignano, C., Afferrante, L., Carbone, G., Demelio, G., 2012a. The influence of the statistical properties of self-affine surfaces in elastic contacts: A numerical investigation. Journal of the Mechanics and Physics of Solids 60 (5), 973 – 982.

Putignano, C., Afferrante, L., Carbone, G., Demelio, G., 2012b. A new efficient numerical method for contact mechanics of rough surfaces. International Journal of Solids and Structures 49 (2), 338 – 343.

Simonsen, I., Tarrats, A., Vandembroucq, D., 2002. Characterization of rough self-affine surfaces by electromagnetic wave scattering. Journal of Optics A: Pure and Applied Optics 4 (5), 168.

Song, H., Vakis, A., Liu, X., der Giessen, E. V., 2017. Statistical model of rough surface contact accounting for size-dependent plasticity and asperity interaction. Journal of the Mechanics and Physics of Solids 106 (Supplement C), 1 – 14.

Spijker, P., Anciaux, G., Molinari, J.-F., 2011. Dry sliding contact between rough surfaces at the atomistic scale. Tribology Letters 44 (2), 279.

Stanley, H., Kato, T., 1997. An fft-based method for rough surface contact. Journal of Tribology 119 (3), 481–485.

Sun, F., van der Giessen, E., Nicola, L., 2012. Plastic flattening of a sinusoidal metal surface: A discrete dislocation plasticity study. Wear 296, 672–680.

Synn, S. Y., Fulton, R. E., 1995. The performance prediction of a parallel skyline solver and its implementation for large scale structure analysis. Computing Systems in Engineering 6 (3), 275 – 284.

van der Giessen, E., Needleman, A., 1995. Discrete dislocation plasticity: a simple planar model. Modelling and Simulation in Materials Science and Engineering 3 (5), 689.

Venugopalan, S. P., Müser, M. H., Nicola, L., 2017a. Green's function molecular dynamics meets discrete dislocation plasticity. Modelling and Simulation in Materials Science and Engineering 25 (6), 065018.

Venugopalan, S. P., Nicola, L., Müser, M. H., 2017b. Green's function molecular dynamics: including finite heights, shear, and body fields. Modelling and Simulation in Materials Science and Engineering 25 (3), 034001.

Wagner, G. J., Karpov, E. G., Liu, W. K., 2004. Molecular dynamics boundary conditions for regular crystal lattices. Comput. Methods in Appl. Mech. Eng. 193, 1579–1601.

Wagner, G. J., Karpov, E. G., Liu, W. K., 2005. A green's function approach to deriving nonreflecting boundary conditions in molecular dynamics simulations. Int J Numer Meth Eng 62, 1250.

Widjaja, A., Van der Giessen, E., Deshpande, V., Needleman, A., 2007. Contact area and size effects in discrete dislocation modeling of wedge indentation. Journal of Materials Research 22 (3), 655–663.

Yin, X., Komvopoulos, K., 2012. A discrete dislocation plasticity analysis of a single-crystal semi-infinite medium indented by a rigid surface exhibiting multi-scale roughness. Philosophical Magazine 92 (24), 2984–3005.

Zhou, C., Beyerlein, I. J., LeSar, R., 2011. Plastic deformation mechanisms of fcc single crystals at small scales. Acta Materialia 59 (20), 7673 – 7682.

Zhou, C., Biner, S., LeSar, R., 2010. Discrete dislocation dynamics simulations of plasticity at small scales. Acta Materialia 58 (5), 1565–1577.

4

INDENTATION OF A PLASTICALLY DEFORMING METAL CRYSTAL WITH A SELF-AFFINE RIGID SURFACE

Although indentation of elastic bodies by self-affine rough indenters has been studied extensively, little attention has so far been devoted to plasticity. This is mostly because modeling plasticity as well as contact with a self-affine rough surface is computationally quite challenging. Here, we succeed in achieving this goal by using Green's function dislocation dynamics, which allows to describe the self-affine rough surface using wavelengths spanning from 5 nm to 100 μm. The aim of this work is to gain understanding in how plastic deformation affects the contact area, contact pressure and hardness, gap profile and subsurface stresses, while the roughness of the indenter is changed. Plastic deformation is found to be more pronounced for indenters with larger root-mean-square height and/or Hurst exponent, and to be size dependent. The latter means that it is not possible to scale observables, as typically done in elastic contact problems. Also, at a given indentation depth (interference) the contact area is smaller than for the corresponding elastic contact problem, but gap closure is more pronounced. Contact hardness is found to be much larger than what reported by classical plasticity studies. Primarily, this is caused by limited dislocation availability, for which the stiffness of the deforming crystal is in between that of a linear elastic and an elastic-perfectly plastic material. When calculating hardness and nominal contact pressure, including very small wavelength in the description of the surface is not necessary, because below a given wavelength the subsurface stresses become invariant to a further decrease in true contact area. This is true for both elastic and plastic materials. Considering small wavelengths is instead required to capture accurately roughening and contact stress distribution.

4.1. INTRODUCTION

Contact between surfaces under moderate load involves only a fraction of the surface asperities, given that most surfaces, even when visually flat, have a self-affine fractal character (Bouchaud, 1997; Bouchaud et al., 1990; Dauskardt et al., 1990; Imre et al., 1992; Krim and Palasantaz, 1995; Lechenault et al., 2010; Majumdar and Tien, 1990; Mandelbrot et al., 1984; Plouraboué and Boehm, 1999). The change in contact area and local stress distribution when the surfaces are pressed into contact determines phenomena such as friction, wear, adhesion, fretting and contact fatigue. However, experimentally, it is very challenging to measure local changes in contact area, especially when the surfaces are non transparent, as in the case of metals, which is the material of interest in this study.

Recently, much effort has been devoted to the numerical modeling of rough surface contacts. In virtue of advances in numerical techniques it is now possible to model the self-affinity of surfaces incorporating a wide range of length scales. These modeling techniques include the biconjugate-gradient stabilized method (Wu, 2006), the boundary-element approach (Ilincic et al., 2011, 2009; Putignano et al., 2012a,b), the fast-Fourier-transform based boundary-value methods (FFT-BVM) (Polonsky and Keer, 2000; Stanley and Kato, 1997) and Green's function molecular dynamics (GFMD) (Campañá and Müser, 2007; Campañá et al., 2008; Dapp et al., 2014; Prodanov et al., 2014). Studies using these methods have so far mostly focused on describing contact between bodies that behave elastically. However, the assumption that bodies behave elastically during contact is only valid as long as the stress in the body is mostly hydrostatic, i.e. when the bodies are nearly in full contact, or when the root-mean-square (rms) height of the rough surface or its Hurst exponent are very small. All these conditions are not met by metal surfaces, which require extremely high loads to reach full closure, have rms height ranging from 0.3 μm to 2.5 μm (Plouraboué and Boehm, 1999) and have Hurst exponent ranging from 0.3 to 0.9 (Bouchaud et al., 1990; Dauskardt et al., 1990; Imre et al., 1992; Lechenault et al., 2010; Plouraboué and Boehm, 1999), depending on the finishing. Rough metal bodies are therefore expected to deform plastically under rather moderate load. The main objective of this work is to study the plastic response of metal crystals indented by a self-affine rigid surface and investigate how their behavior differs from that of elastically deforming bodies. To this end we will use a modeling technique,

Green's function dislocation dynamics, which accurately captures deformation of the rough surface, as well as dislocation plasticity in a two-dimensional framework (Venugopalan et al., 2017a).

While there is a broad literature dealing with elastic deformation of rough surfaces, much less work has been devoted to plastic deformation (see Ghaednia *et. al.* (Ghaednia et al., 2017) for a recent review). The first elasto-plastic contact model was proposed by Chang, Etsion and Bogy (Chang et al., 1987) and was based on the conservation of volume of the plastically deforming asperities. At a critical interference value, the material would switch from the fully elastic to the fully plastic regime. The model, although improved by Zhao *et. al.* (Zhao et al., 2000) to include an intermediate elasto-plastic regime, has the drawback that ignores interaction between asperities. The interaction is naturally captured in the work of Gao *et. al.* (Gao et al., 2006; Gao and Bower, 2006), who studied elasto-plastic contact between sinusoidal surfaces and surfaces with a Weierstrass profile. These studies showed that the pressure to cause complete contact between surfaces can reach a value 5.8 times larger than the yield strength of the bulk material, thus larger than the hardness of an isolated asperity modeled by classical plasticity (about $3\sigma_{\text{y}}$). This is in consistence with the findings of Pei *et. al.* (Pei et al., 2005) who modeled indentation of a flat body, deforming according to J_2 plasticity, indented by a self-affine fractal rigid surface. They argued that it is the interaction between asperities that brings the mean contact pressure p_{m} above the single asperity hardness. Both the work of Gao *et. al.* (Gao et al., 2006) and of Pei *et. al.* (Pei et al., 2005) were based on classical plasticity and therefore ignored size effects, which are found to play an important role at the micro-scale (Fleck et al., 1994; Greer et al., 2005; Ma and Clarke, 1995; Nicola et al., 2003, 2006; Volkert and Lilleodden, 2006). Due to size-dependent plasticity, metals are found to be harder to indent for decreasing size of the indenter and of the indentation depth (Nix and Gao, 1998; Swadener et al., 2002; Zong and Soboyejo, 2005). One can therefore expect that size-dependent plasticity would also affect the response of rough metal surfaces upon contact, especially when interference is small. Discrete dislocation dynamics simulations can well capture size effects and will enable us in this work to assess their influence on the contact response of rough surfaces. Also, the simulations provide the subsurface stress fields, which are of great importance in determining where are the critical locations where dislocation-driven failure mechanisms can occur.

Discrete dislocation plasticity simulations of contact were already performed for very simple surfaces: indentation or shearing by isolated indenters in two- (Balint et al., 2006; Deshpande et al., 2007; Sun et al., 2016; Widjaja et al., 2007) and three-dimensions (Curtin and Miller, 2003; Fivel, 2008), periodic arrays of flat indenters (Nicola et al., 2007, 2008) and flattening of sinusoidal surfaces (Deshpande et al., 2007; Ng Wei Siang and Nicola, 2017; Sun et al., 2015, 2012). These simulations confirm that for these very simple geometry the plastic response is size dependent. Dislocation dynamics simulations of contact are computationally rather expensive even in two dimensions, therefore the contact problem between self-affine surfaces, which require a fine discretization to capture a broad range of wavelength, was not attempted so far. However, Yin *et*. *al*.(Yin and Komvopoulos, 2012) presented dislocation dynamics simulations for an indenter made of Hertzian asperities of different size, to simulate the effect of multi-scale roughness and showed that rougher asperities induce more plasticity than smooth ones, and that subsurface stresses and dislocation densities strongly increase with interference. Recently, we presented a new version of two-dimensional discrete dislocation plasticity based on the formulation of Van der Giessen and Needleman (van der Giessen and Needleman, 1995) that uses Green's function molecular dynamics to compute the image fields, and by that provides a significant gain in computational speed (Venugopalan et al., 2017a). Thanks to this method we can now model indentation with a self-affine rough indenter of a crystal deforming by dislocation plasticity to gain a better understanding of the effect of roughness parameters such as rms height, Hurst exponent, and short wavelength cut-off, by keeping track of the evolution of the contact area, of the tractions and subsurface stresses.

The remainder of the chapter starts with the formulation of the problem in section 5.2. Then the GFDD methodology is briefly presented in 5.2.2, more details can be found in (Venugopalan et al., 2017a). The way in which the surfaces are generated is given in section 4.2.2. The parameters chosen for the GFDD simulations are listed in section 4.2.3. In section 4.3.1, the loading rate is determined at which the GFDD simulations can be considered quasi-static. In section 4.3.2 the size dependence of self-affine plastic indentation is demonstrated. The effect of rms height and Hurst exponent on the contact pressure and area are presented in section 4.3.3. The effect of short wavelength cut-off on the contact deformation of elastic and plastic crystals is shown in section 4.3.4.

The area–load dependency for the elasto-plastic crystal is presented in section 4.3.5.

4.2. FORMULATION OF THE PROBLEM

The schematic representation of the metal crystal indented by a rigid rough indenter is shown in figure 4.1. Indentation is performed by specifying the displacement rate of the
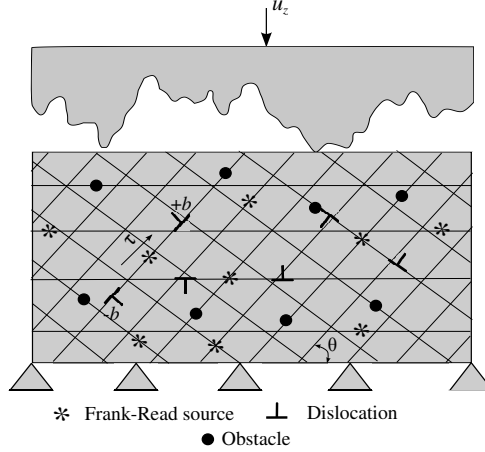
Figure 4.1: Schematic representation of the metal crystal indented by a rough surface.

rigid indenter $\dot{u}_z$. The top surface of the crystal is taken to be frictionless at the points of contact, $\sigma_{xz}(x_c, z_c) = 0$, and traction-free elsewhere, $\sigma_{xz}(x_{nc}, z_{nc}) = \sigma_{zz}(x_{nc}, z_{nc}) = 0$. The subscripts 'c' and 'nc' stand for 'points in contact' and 'points not in contact', respectively. The bottom of the unit cell, $z = 0$ is fixed: $u_x(x, 0) = u_z(x, 0) = 0$.

Following van der Giessen and Needleman (1995) the crystal is initially dislocation free, and contains a given density of slip planes, dislocation sources, and obstacles. When the stress in the body is sufficiently high, dislocation dipoles are nucleated from the sources and glide on the slip planes, by that reducing the stress in the body. Each dislocation source nucleates a dipole when subjected to a resolved shear stress exceeding its critical strength, τ_{nuc}, for a given amount of time, t_{nuc}. Each dislocation source can emit multiple dipoles. The velocity with which dislocations glide is controlled by the Peach-Koehler force acting on them. Dislocations are stopped by the obstacles, but released when the resolved shear stress on them exceeds the critical strength associated to the obstacle, τ_{obs}.

4.2.1. SOLUTION THROUGH GREEN'S FUNCTION DISLOCATION DYNAMICS

The solution at each time step of the simulation is obtained by the superposition of two linear elastic solutions: The elastic analytical fields for dislocations in a homogeneous infinite solid, and the solution to the complementary elastic boundary-value problem, which corrects for the boundary conditions (van der Giessen and Needleman, 1995). The latter is obtained through Green's function molecular dynamics (GFMD) (Prodanov et al., 2014). The methodology is illustrated in figure 4.2 for the indentation of a single crystal by a rigid indenter with self-affine surface topography. The elastic dislocation fields are represented by the superscript (^{d}), the fields solving the complementary boundary-value problem by the superscript (^).
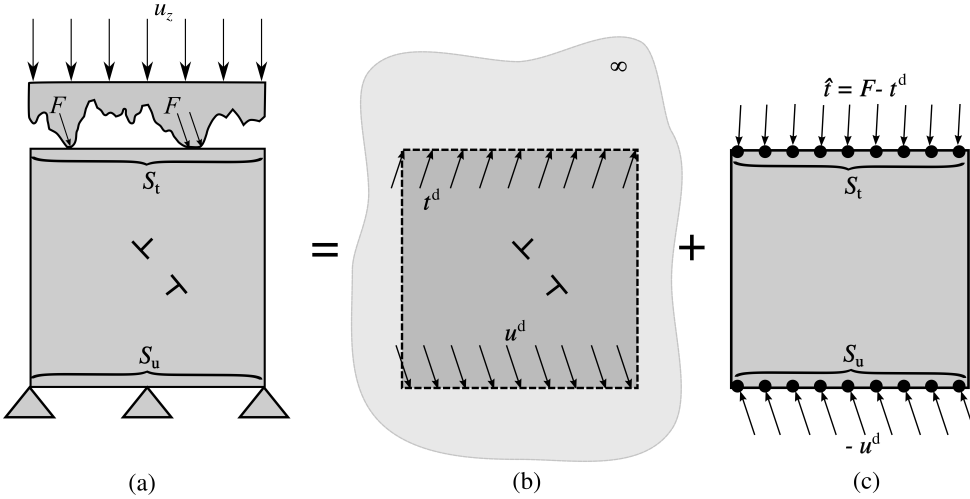
Figure 4.2: (a) Schematic representation of the dislocated crystal indented by a rigid rough body. The bottom of the crystal is fixed while the indenter is pressed into contact by applying a constantly increasing displacement which gives rise to interfacial tractions, F. The solution is obtained by superposing (b) the elastic fields of the dislocations in an infinite medium and (c) the solution to the elastic boundary-value problem which corrects for the boundary conditions.

GFMD is a boundary-value method to study the elastic response of a body subjected to contact loading (Prodanov et al., 2014; Venugopalan et al., 2017a,b). In GFMD, only the surface of the deformable body is modeled explicitly and discretized using nx equi-spaced grid points. The rough surface is assumed to obey the small slope approximation. The interfacial interaction adopted here is the simplest possible: in normal direction a hard-wall constraint is imposed to avoid inter-penetration, and in tangential direction the contact is assumed to be frictionless. This is achieved by letting the contact points

oscillate laterally to equilibrium without any constraint. It is possible to use more so-phisticated interfacial interactions, for instance traction–separation laws that allow for the coupling between normal and tangential separation, but in this work we have chosen to focus on plasticity instead of on the interfacial behavior.

The unknown surface displacement fields $\tilde{\boldsymbol{u}}(q) = (\tilde{u}_1(q), \tilde{u}_3(q))$ for each mode with wavenumber q are calculated in Fourier space using damped dynamics. The advantage of damping the system in Fourier space is that the different modes describing the surface are uncoupled. The static solution is found using damped dynamics, while the body fields are calculated from the surface fields using closed-form analytical solutions (Venugopalan et al., 2017a).

4.2.2. Generation of the rough surface

The periodic self-affine surface topography for an indenter with Gaussian height distribution is generated with the power spectral density method (Campañá et al., 2008). The self-affine surfaces are constructed by generating the Fourier coefficients of the height profile as:

$$\tilde{h}(q) = h_0 \, \tilde{\Delta}_{\mathrm{G}}(q) \sqrt{C_{\mathrm{h}}(q)} = h_0 \, \frac{\tilde{\Delta}_{\mathrm{G}}(q)}{q^{\left(\frac{1}{2} + H\right)}}, \tag{4.1}$$

where h_0 is a real-valued constant which can be adjusted to obtain the aspired rms slope of the surface, $\tilde{\Delta}_{\mathrm{G}}(q)$ is a Gaussian random variable with random phase such that $\langle \tilde{\Delta}_{\mathrm{G}}(q) \rangle = 0$, $C_{\mathrm{h}}(q)$ is the surface height spectrum corresponding to a wave number q, and H is the Hurst exponent. The real and imaginary parts of the Gaussian random variable $\tilde{\Delta}_{\mathrm{G}}(q) = \mathscr{R}\{\tilde{\Delta}_{\mathrm{G}}(q)\} + i\mathscr{I}\{\tilde{\Delta}_{\mathrm{G}}(q)\}$ are found from a real-valued Gaussian sequence $G[n]$ of finite length nx as:

$$\begin{aligned} \mathscr{R}\{\tilde{\Delta}_{\mathrm{G}}(q)\} &= \frac{1}{nx} \sum_{n=0}^{nx} G[n] \cos qn, \\ \mathscr{I}\{\tilde{\Delta}_{\mathrm{G}}(q)\} &= \frac{1}{nx} \sum_{n=0}^{nx} G[n] \sin qn. \end{aligned} \tag{4.2}$$

The power-law scaling for the surface height spectrum applies between cut-offs at long and short wave numbers $q_0 < q < q_{\mathrm{s}}$, where $q_0 = 2\pi/\lambda_{\mathrm{l}}$ and $q_{\mathrm{s}} = 2\pi/\lambda_{\mathrm{s}}$ are the wavenumbers corresponding to the long and short wavelengths λ_{l} and λ_{s} (see figure 4.3). The rms

height $\bar{h}$ and rms gradient $\bar{g}$ of the surface are

$$\bar{h}^2 = \frac{1}{nx} \sum_{\mathbf{q}} |\tilde{h}(\mathbf{q})|^2$$

$$\bar{g}^2 = \frac{1}{nx} \sum_{\mathbf{q}} q^2 |\tilde{h}(\mathbf{q})|^2 .$$

(4.3)
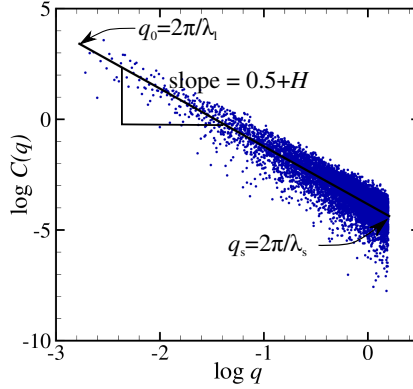
Figure 4.3: Power spectral density with Gaussian distribution generated numerically for a given realization.

For different realizations of the rough surface, all parameters, including the cut-off values, are kept fixed except the Gaussian random variable $\tilde{\Delta}_G(q)$ whose phase is randomly varied.

Before starting the simulation the surfaces so generated are shifted such that the lowest point touches the substrate at zero interfacial pressure.

4.2.3. CHOICE OF PARAMETERS

In this section the default parameters used in the simulations are listed.

The height of the crystal is chosen to be $z_m = 10\ \mu$m, which is sufficiently large that dislocations do not interact with the bottom of the crystal and sufficiently small to guarantee that plastic deformation occurs at small interference.

The elastic constants are taken to represent aluminum: the Young's modulus is $E = 70$ GPa and Poisson's ratio $\nu = 0.33$. The dislocations can glide on three sets of parallel slip planes, orientated at: 0°, 60° and 120° with the bottom surface. The discrete slip

planes are spaced at $100b$ where $b = 0.25$ nm is the length of Burger's vector. The Frank-Read sources and obstacles are randomly distributed in the crystal with a density $\rho_{\text{nuc}} = 40\ \mu\text{m}^{-2}$ and $\rho_{\text{obs}} = 40\ \mu\text{m}^{-2}$. The average source spacing $L_{\text{ave}} = \sqrt{1/\rho_{\text{nuc}}} = 158$ nm. The strength of the sources follows a Gaussian distribution with mean strength $\tau_{\text{nuc}} = 50$ MPa and standard deviation of 10 MPa. The critical time for nucleation is $t_{\text{nuc}} = 10$ ns. The strength of the obstacles is taken to be $\tau_{\text{obs}} = 150$ MPa. Dislocations of opposite sign in the same slip plane annihilate when the distance between them is below $L_{\text{ann}} = 6b$. The time step required to properly capture the dislocation interactions is found to be $\Delta t = 2.5$ ns.

In GFMD, the center-of-mass mode is critically damped or slightly under-damped for quick convergence. The damping factor is

$$\eta \propto \frac{1}{\tau}\sqrt{\left(\frac{E}{2(1+\nu)}\right)\left(\frac{L_x}{z_{\text{m}}\ nx}\right)}, \tag{4.4}$$

where $\tau = 0.25$ is the dimensionless time step used for the damped dynamics. The number of iterations to reach convergence scales as

$$n_{\text{it}} \propto \sqrt{\left(\frac{2(1+\nu)}{E}\right)\left(\frac{z_{\text{m}}\ nx}{L_x}\right)}. \tag{4.5}$$

The values for the thermodynamic, fractal and continuum (TFC) discretizations, unless otherwise stated, are $\epsilon_{\text{t}} = 2^{-1}$, $\epsilon_{\text{f}} = 512^{-1}$ and $\epsilon_{\text{c}} = 32^{-1}$. The fractal discretization, $\epsilon_{\text{f}} = \lambda_{\text{s}}/\lambda_{\text{l}}$, defines the number of wavelengths used to describe the surface. Here, the long wavelength cut-off is kept constant, i.e. $\lambda_{\text{l}} = 10\ \mu$m and the short wavelength cut-off varied to assess the effect of small features on the plastic response of the crystal. The thermodynamic discretization is defined as $\epsilon_{\text{t}} = \lambda_{\text{l}}/L_x$, where L_x is the width of the periodic unit cell. In the limiting case of $\epsilon_{\text{t}} \to 0$, which corresponds to the thermodynamic limit, the surface is no longer periodic since $L_x \to \infty$. Finally, the continuum discretization is defined as $\epsilon_{\text{c}} = a_0/\lambda_{\text{s}}$ where a_0 is the spacing between the grid points that discretize the surface of the substrate. In the limiting case of $\epsilon_{\text{c}} \to 0$, the grid spacing $a_0 \to 0$ and hence the surface has a continuum representation, therefore the solution must converge to the continuum mechanics solution.

4.3. RESULTS AND DISCUSSION

4.3.1. LOADING RATE

Firstly, we determine for which loading rate the simulations can be considered quasi-static. To this end, the crystal is indented at different loading rates to a depth of 0.01 μm. The indenter is then held at constant depth until $t = 125 \times \dot{u}_z^0/\dot{u}_z$ ns, where $\dot{u}_z^0 = 4 \times 10^5$ μm/s is the reference loading rate. Figure 4.4 shows the change in nominal contact pressure $p_n = F/L_x$, where F is the total contact force. It can be seen that, upon loading, the response of the substrate is stiffer for higher loading rates. This is caused by the fact that the generation of dislocations is controlled by the nucleation time t_{nuc}. If the loading is fast compared with the rate of dislocation nucleation, L_{nuc}/t_{nuc}, dislocations do not have the time to nucleate, glide, and relax the pressure as much as needed. This is why for the faster loading rate used here, $\dot{u}_z^0 = 4 \times 10^5$ μm/s, the loading curve is close to the elastic limit. Only when the indenter is kept fixed at final indentation depth, the dislocations have the time to be nucleated also in the crystals that where subjected to fast loading, leading to a decrease of the contact pressure. A loading rate of $\dot{u}_z^0 = 4 \times 10^3$ μm/s is chosen for all our simulations since it results in a negligible relaxation of the contact pressure at constant loading.

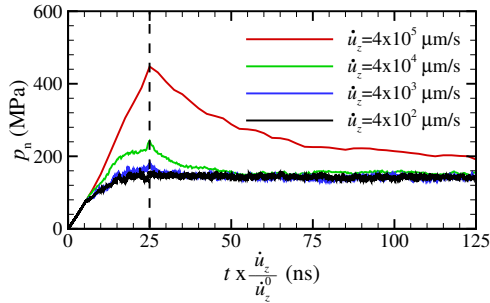Figure 4.4: Nominal contact pressure upon indentation to a depth of 0.01 μm and subsequent relaxation.

4.3.2. SIZE EFFECT

To assess the occurrence of plasticity size effects in self-affine indentation we scale both the size of the crystal and the rough surface topography equally in $x-$ and $z-$ direction, while keeping the realization of the rough surface unaltered. The scaling ensures that the

elastic response of all crystals is identical, such that differences in the plastic response are highlighted. The smallest crystal has width $L_x = 10\ \mu$m and height $z_m = 5\ \mu$m. It is indented by a rough surface with rms height $\bar{h} = 0.05\ \mu$m. The dimensions of the other two crystals are scaled up by two and four, so is the rms roughness height of the indenter. All crystals are indented to the same strain, $u_z / z_m = 0.002$.

As expected, the curves representing nominal contact pressure versus strain are found to be indistinguishable for all elastic crystals, as can be seen in figure 4.5(a). On the contrary, a size effect is observed for the plastically deforming crystals. The thinner crystals, indented by a surface with smaller rms height, have a stiffer response upon indentation. Also, the contact area they form is larger and closer to the elastic limit (figure 4.5(b)). The relative contact area in figure 4.5(b) is defined as $a_r = A / A_0$, where A is the real contact area and A_0 is the apparent contact area. The kink in the curves in figure 4.5(a) indicates that a new cluster of asperities has come into contact.

It is important to note here, that for a given displacement of the indenter, the contact area is smaller for plastic crystals compared to their elastic counterparts. Since the occurrence of plastic deformation reduces the interfacial force, a larger interference is required to reach the same contact area that would be reached elastically. This findings are in contradiction with the early elasto-plastic models (Chang et al., 1987; Zhao et al., 2000), where contact area was expected to increase with plasticity. This is because those models are based on the incorrect assumption that the plastic contact area is given by the geometric intersection between crystal and indenter.

The normal traction t_z profiles at final strain are shown in figure 4.6. As expected, the elastic profiles overlap again, while the traction profiles become closer to the elastic solution for smaller rms height. The high peaks that characterize the profile for larger rms height are a consequence of the serrated nature of plastically deforming surfaces: the exit of dislocations leads to crystallographic steps at the surface which become more pronounced when several dislocations leave the body from the same slip plane Ng Wei Siang and Nicola (2017). The difference between contact pressure profiles for elastically and plastically deformed surfaces is rather pronounced: plasticity does not only lead to a smaller nominal contact pressure and true contact area, but to a very different distribution of the contact stresses. Locally the surface stresses are an order of magnitude larger than what predicted by earlier classical plasticity study (the nucleation strength
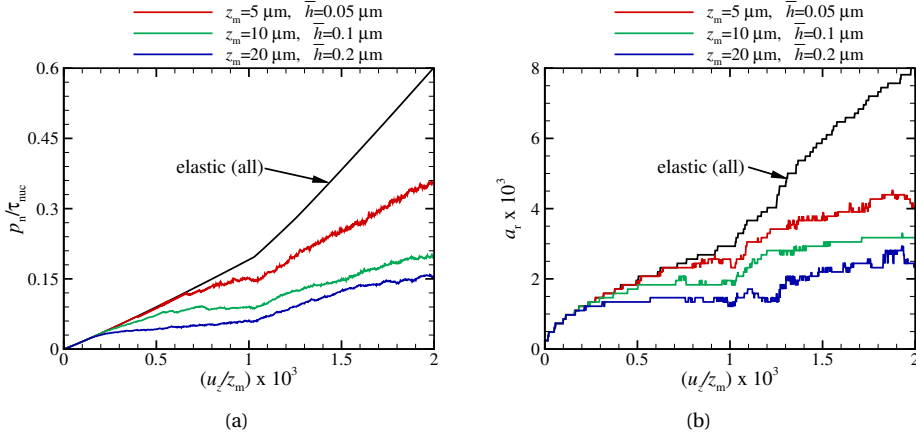
Figure 4.5: (a) Nominal contact pressure and (b) relative contact area as a function of strain for crystals with scaled height indented by a rough profile with scaled rms height.

on which the tractions are magnified is of the same order as the yield strength). Consequently, also the subsurface stresses are much affected by plasticity, as shown in figure 4.7, where the stress distribution in crystals of different size are compared. Here, one can see that the size dependence is caused by dislocation source starvation in the smaller crystals: the reduced contact area is the same as in larger crystals, but the actual contact area is smaller. Therefore, the contact pressure gives rise to a smaller region affected by high stresses, where dislocations can nucleate. Because of limited source availability, the crystal with smaller dimensions exhibits less plasticity.

Figure 4.6: Normal traction t_z profiles at strain $u_z/z_m = 0.002$ for crystals with scaled dimensions, indented by a rough surface with scaled rms height.

An important implication of the size-dependent response just demonstrated is that–

Figure 4.7: Stress and dislocation distribution in two crystals with (a) $z_m = 5$ μm, $\bar{h} = 0.05$ μm and (b) $z_m = 20$ μm, $\bar{h} = 0.2$ μm at strain $u_z/z_m = 0.002$. The 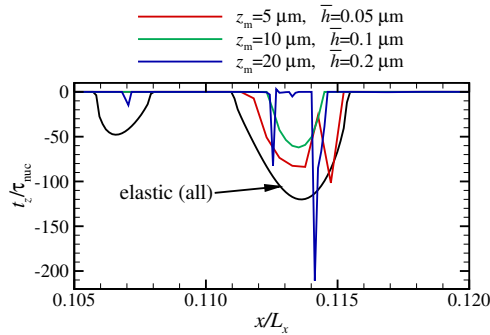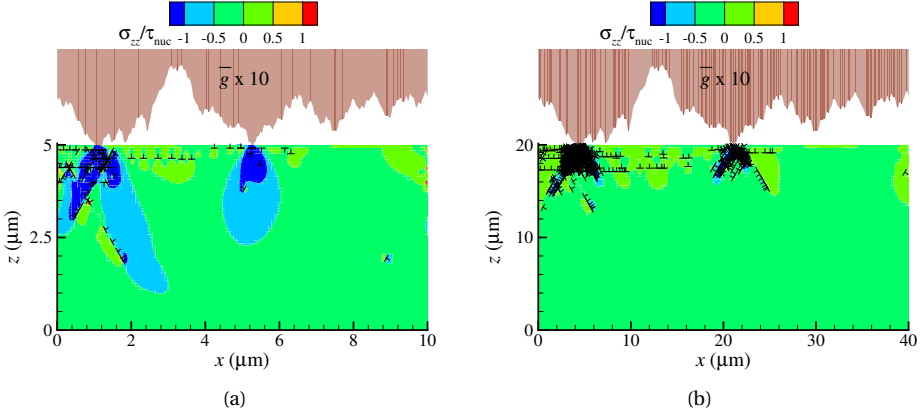rms height of the indenter is also scaled with z_m, and magnified by a factor of 10 in $z-$direction for better visualization.

for plastically deforming bodies–it is not possible to scale observables such as the contact pressure, the contact area, and the gap, with crystal size or rms height of the indenter, as typically done for elastic contact problems Müser et al. (2017); Prodanov et al. (2014).

4.3.3. EFFECT OF RMS HEIGHT AND HURST EXPONENT

Here, differently from the previous section, we keep the crystal size constant and we search for the rms height that causes appreciable plasticity: a small rms height is expected to mostly induce a hydrostatic stress state in the subsurface, while a deviatoric stress component is needed to induce plasticity.

Figure 4.8(a) displays the nominal contact pressure, normalized on $\tau_{nuc}\bar{g}$, as a function of indentation depth u_z, normalized on rms height $\bar{h}$. The normalization allows for the overlapping of the elastic curves. Again, the plastic response cannot be scaled, and one can observe that the larger the rms height the larger the reduction in mean contact pressure assisted by plasticity. Although elastically at a given $u_z/\bar{h}$ the reduced pressure is the same for all cases considered, the subsurface stresses induced by different rms height differ. This is because a small rms height corresponds to various small and closely spaced contact patches, which induce an almost hydrostatic subsurface stress state. A large rms height corresponds instead to few larger but more isolated contacts,

which lead to a larger deviatoric stress component. For a rms height of 1 μm the plastic response is mostly pronounced as seen in the dislocation density plots in figure 4.8(b).

We select $\bar{h} = 0.1$ μm for all simulations in the subsequent sections, since a lower value of rms height - as generally chosen in the literature of elastic contacts Hyun et al. (2004); Persson (2001); Polonsky and Keer (2000); Prodanov et al. (2014)- is unrealistic for metals and, as we just saw, induces a mostly hydrostatic stress state. A larger value of rms height violates the assumption of small-slope approximation on which the GFMD model is based, already at small indentation depth. It is however noteworthy, that metal contacts with rms height larger than what selected here are common, and they will have an even larger plastic contribution than what presented in this work.

(a)   (b)
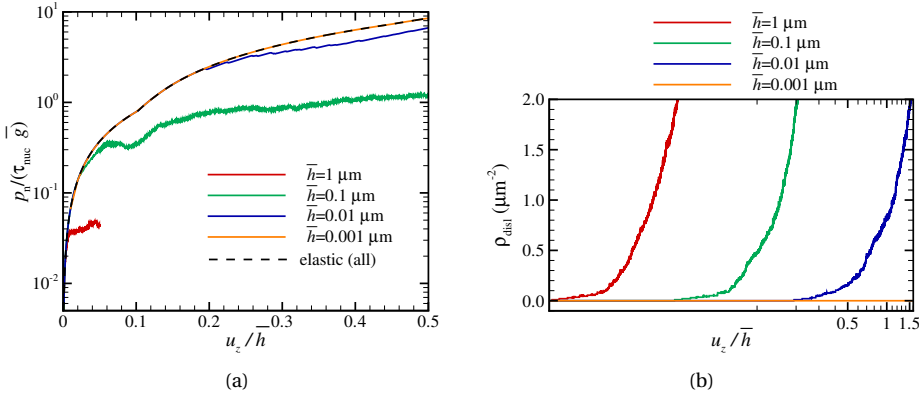
Figure 4.8: (a) Normalized nominal contact pressure for different rms heights. All elastic curves overlap. Also, the curve corresponding to the plastic response of the crystal with rms height $\bar{h} = 0.001$ μm overlaps with the elastic curve, but will deviate at larger indentation depth. (b) Dislocation density ρ_{disl} in the crystal is plotted for different rms heights.

Next, we analyze the effect of varying Hurst exponent of the indenting surface on the plastic response of the crystals, while all other surface parameters are kept constant. Experimentally measured values of the Hurst exponent for metals fall in the range of $H = 0.3$ to $H = 0.9$ depending on the material and its finishing Bouchaud et al. (1990); Dauskardt et al. (1990); Imre et al. (1992); Lechenault et al. (2010); Plouraboué and Boehm (1999).

The change in nominal contact pressure, relative contact area and dislocation density for indentation with surfaces with three different Hurst exponents $H = 0.3$, 0.5, 0.8 are presented in figure 4.9. It can be seen that for the elastic crystals, the resistance to

indentation is larger for increasing values of the Hurst exponent since for a given inden-
tation depth the smoother indenter profiles form a larger contact area with the crystal.
However, for plastically deforming crystals, the contact pressure curves corresponding to
different Hurst exponents tend to converge at large indentation depth such that plastic-
ity acts as a grand equalizer, consistently to what Pei et. al. Pei et al. (2005) had observed.
This implies that the contribution of plasticity increases with the Hurst exponent (see
for confirmation figure 4.9(c)). This is to be expected, considering that the larger contact
area induced by the indenters with larger H (see figure 4.9(b)) is related to a broader sub-
surface stressed region and therefore a greater availability of active dislocation sources.

The shear bands that form during plastic flow can be seen for $H = 0.3$ and $H = 0.8$
in figure 4.10(a) and 4.10(b). One can see that the crystal indented by the surface with
$H = 0.3$ has more, but smaller, areas of contact than the other crystal. The shear bands
that form are therefore more but shorter, since they form later and they intersect, ob-
structing each others propagation. The crystal indented by the surface with larger Hurst
exponent has a very long shear band that extends deep in the material. Notice, that these
shear bands could not be captured by classical plasticity. The capability of capturing the
subsurface stress distribution is very important, since it can signal initiation of failure in
the material, for instance the initiation of cracks.

In all subsequent simulations, we choose a Hurst exponent $H = 0.8$ as observed on
most metallic surfaces (Bouchaud et al., 1990; Dauskardt et al., 1990).

4.3.4. THE SHORT WAVELENGTH CUT-OFF

In this section we investigate the effect of including fine roughness features on the plas-
tic contact response, by comparing simulations in which the indenter is described using
various fractal discretizations $\epsilon_f = \lambda_s / \lambda_l$. The fractal discretization is varied by keep-
ing the long wavelength cut-off constant and equal to 10 μm and changing the short
wavelength cut-off. The largest fractal discretization $\epsilon_f = 1$ corresponds to a sinusoidal
indenter and the smallest fractal discretization $\epsilon_f = 512^{-1}$ to wavelengths down to $\lambda_s =$
19.5 nm.

Figure 4.11 shows the deformed surface after indentation to $u_z = 0.05$ μm for elastic
and plastic crystals. Surface profiles for $\lambda_s = 19.5$ nm and $\lambda_s = 156$ nm are compared and
contrasted with those obtained by indenting with a sinusoidal surface. For the sinusoidal

(a)

(b)

(c)
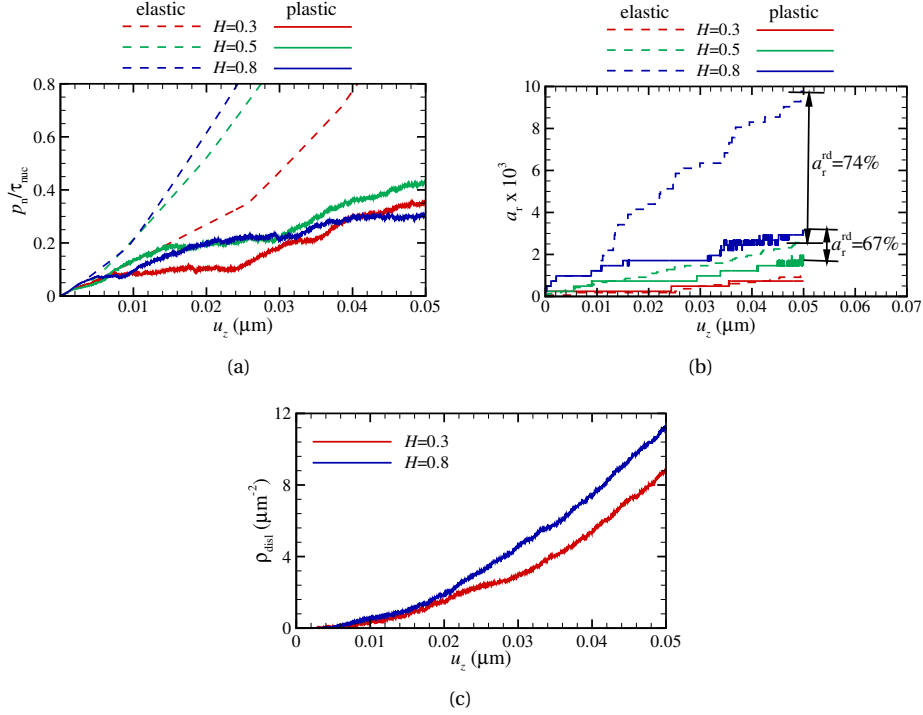
Figure 4.9: (a) Nominal contact pressure (b) relative contact area, and (c) dislocation density during indentation with a rigid rough surface with various Hurst exponents.

(a)

(b)
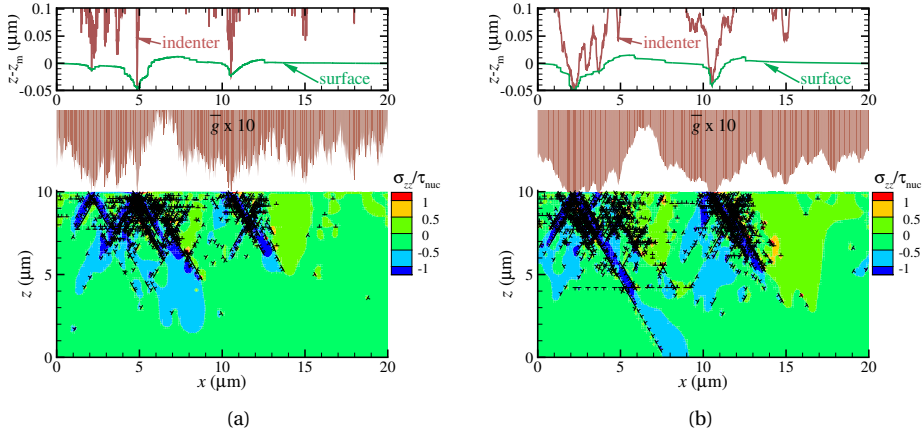
Figure 4.10: Deformed surface profile (top); stress and dislocation distribution (bottom) for (a) $H = 0.3$ and (b) $H = 0.8$.

indentation, the contact occurs elastically over a single large patch whereas for the self-affine indenter, the contact is formed by several smaller patches. As a result, the real contact area for $\lambda_s = 156$ nm is found to be at least an order of magnitude smaller than that of sinusoidal indentation.

With plasticity, there is a pronounced material pile up in the zones surrounding the contact. This results in the surface conforming more to the indenter and hence into a significantly smaller interfacial separation. This is relevant for problems concerning the leakage of seals, where the gap between surfaces controls percolation of the fluid (Dapp et al., 2012; Pérez-Ràfols et al., 2016).

(a)

(b)

(c)
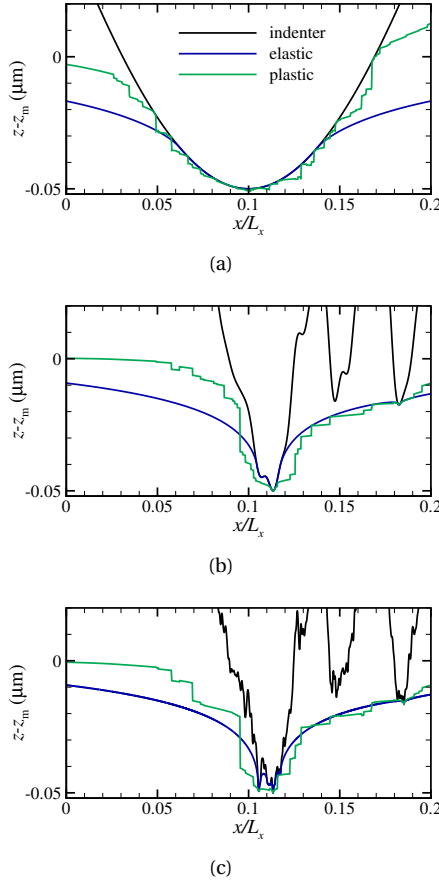
Figure 4.11: Deformed surface profile at an indentation depth of 0.05 μm for (a) sinusoidal indenter and fractal indenters with (b) $\lambda_s = 156$ nm and (c) $\lambda_s = 19.5$ nm.

Despite interfacial separation is smaller for plasticity than for elasticity, the contact area

is smaller for the plastic case, given that, at a given indentation depth, the contact pressure is reduced by plasticity. Figure 4.12 shows the relative contact area at final indentation depth a_r^{fin} for different fractal discretizations. It is seen that the contact area decreases with fractal discretization for both elastic and plastic crystals with approximately the same rate. Smaller fractal discretization is characterized by asperities with smaller length scales that form contact over several smaller patches. In the case of sinusoidal indentation, the difference between elastic and plastic contact area is less. This is due to the fact that when the surface deforms plastically, dislocations exit the free surface leaving crystallographic displacement steps. This gives rise to small protrusions that make additional contact with the indenter (see figure11).
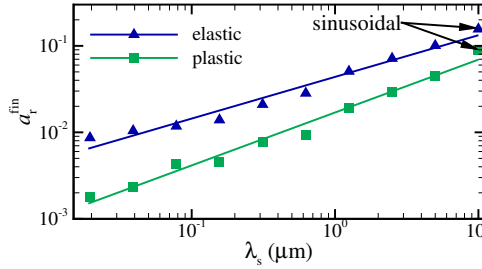
Figure 4.12: Contact area at final indentation depth for different fractal discretizations.

The increase of contact pressure with loading is shown in figure 4.13(a) for various values of fractal discretization. A sudden increase in pressure is observed every time a new cluster of asperities comes into contact. For the two larger discretizations, the nominal contact pressure are very close, although not overlapping, neither for the elastic nor for the plastic simulations.

The results for final nominal contact pressure, normalized on source strength, are reported in figure 4.13 for various values of the fractal discretization, i.e. various λ_s, for elastic and plastic simulations. The results lead to three main observations: (1) the data obtained with dislocation dynamics is just shifted with respect to the data obtained with elastic simulations, with plastic values being approximately 85% (for the dislocation parameters chosen in this work) smaller than the elastic values; (2) Below a threshold wavelength, $\lambda_s = 156$ nm (for the roughness parameters used in these simulations), the nominal contact pressure is unaffected by a further reduction of the short wavelength cut-off. Therefore, if one is interested in nominal contact pressure, it is not worth using a dis-

cretization smaller than this threshold value, irrespectively of whether the simulations include or not plasticity; (3) Despite true contact area always decreases with decreasing fractal discretization (see figure 4.12) nominal contact pressure does not. This means that below a given threshold for λ_s the mean contact pressure, which can be interpreted as hardness of the contact, would increase rather significantly, only because the real contact area decreases. As we will see in more detail shortly, this increase in hardness does not really reflect the physics of the problem.
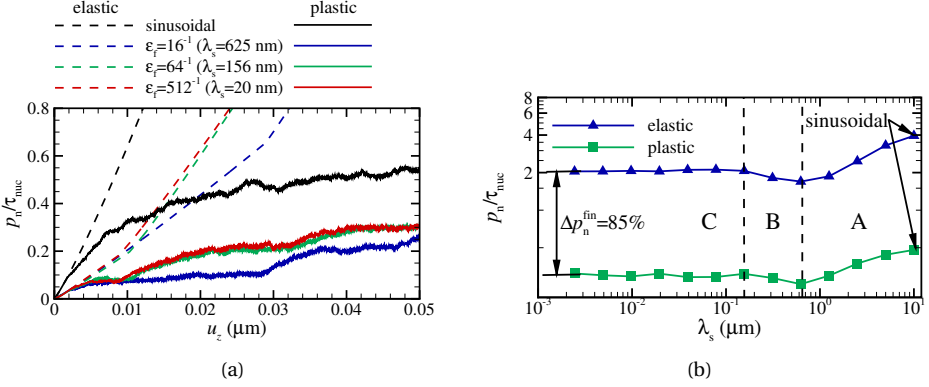
Figure 4.13: (a) Evolution of contact pressure with indentation depth and (b) contact pressure at final indentation depth, for elastic and plastically deformed crystals and various values of the fractal discretization.

Notice that we have distinguished three different domains in figure 4.13(b), indicated with A, B, and C. Zone A represents the large wavelength zone, including as upper limit the sinusoidal wave. In this region the contact occurs at a single protrusion of the indenter, which becomes thinner while decreasing lambda and therefore indents the crystal meeting less resistance. There is only a continuous single contact area. In zone B, an additional decrease in wavelength is accompanied by roughening of the protruding peak which makes contact with the crystal through a couple of closely spaced contact patches, who interact elastically and effectively act as a super-contact with end-to-end distance larger than the true contact area, which always decreases with λ_s. This gives an increase in the resistance to indentation and therefore of contact pressure. In zone C, decreasing wavelength further, corresponds to additional fragmentation of the already very small and closely spaced contact patches. This fragmentation decreases the true contact area further, but does not affect the stressed region in the subsurface, and does therefore not change the nominal contact pressure. This is demonstrated in figure 4.14 for $\lambda_s = 156$ nm

and 19.5 nm. It can be seen that, although the true contact areas are different, in virtue of the elastic interactions, the subsurface stresses are comparable. This implies that (1) measuring or calculating true contact area below a critical threshold wavelength is not useful to determine the mechanical response (even elastic response) of the contact and (2) the quantity that is important to determine the mean contact pressure (or contact hardness) is not the the true contact area, but the effective contact area, indicated in figure 4.14 as AB, which is invariant below the threshold value $\lambda_s = 156$ nm.
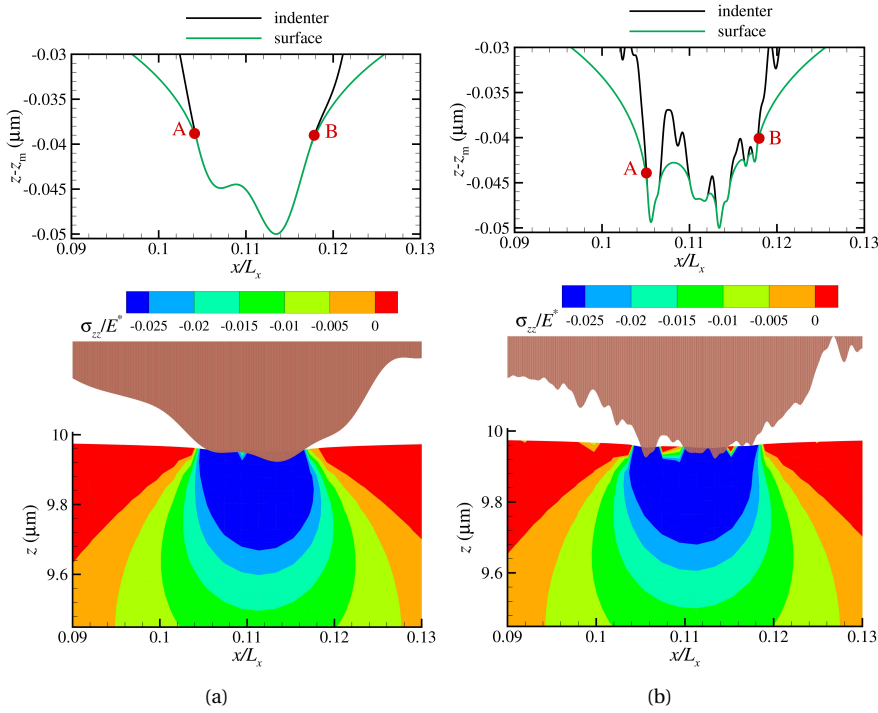
Figure 4.14: Indenters and surface profiles (top) and stress distribution (bottom) for indentation using (a) $\lambda_s = 156$ nm and (b) $\lambda_s = 19.5$ nm.

We choose therefore the threshold value $\lambda_s = 156$ nm to present the change of mean contact pressure $p_m = F/A$ for different source densities in figure 4.15(a). Here F is the interfacial force and A is the true contact area. The mean contact pressure depends rather mildly on the range of source densities chosen, and even for the largest source density considered here it is significantly larger, 35 τ_{nuc}, than what found in simulations based on classical plasticity theory Gao et al. (2004); Pei et al. (2005), where $p_m \approx 6\,\sigma_Y$.

Here σ_Y is the yield strength on tension, which for the material parameters used in our simulations, is 60 MPa, thus of the same order as the nucleation strength, $\tau_{nuc} = 50$ MPa. The reason for the difference between the prediction in mean contact pressure of Green's function dislocation dynamics and the classical plasticity simulations Gao et al. (2004); Pei et al. (2005) is twofold: the most important is that while in classical plasticity, plastic deformation occurs at any location where the yield strength is exceeded, in dislocation dynamics plasticity is limited by the availability of dislocation sources; also, the fractal discretization considered in this work, although cut off, is smaller than that considered in Gao et al. (2004); Pei et al. (2005). The hardness increases as finer roughness is added to the indenter as seen in figure 4.15(b), where the mean contact pressure at $u_z = 20$ nm, which we will call hardness σ_h in the following, is presented as a function of the short wavelength cut-off for $\rho_{nuc} = 40 \ /\mu m^2$. The increase in hardness is mainly due to the decrease in contact area with the decrease in λ_s (see figure 4.12). Since the decrease in true contact area below $\lambda_s \leq 156$ nm was shown to not affect the subsurface stress distribution, the contact hardness should be cut off below this threshold, and the constant value σ_h^{eff} used, as indicated in figure 4.15(b).
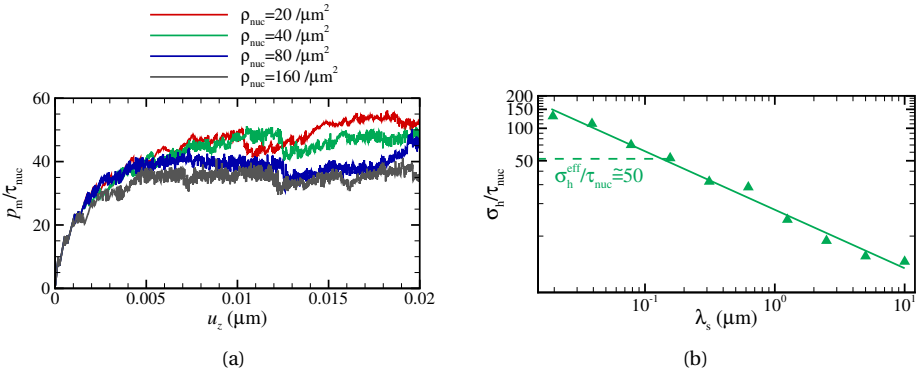
Figure 4.15: (a) Mean contact pressure as a function of strain u_z/z_m for different values of source densities ρ_{nuc}. (b) Asperity hardness σ_h calculated at 0.2 % strain is plotted as a function of λ_s.

The results of this section lead us to the following conclusions that hold for both elasticity and plasticity: If one is interested in real contact area, contact traction distribution, or gap geometry, the surface must be described with great accuracy, including the shortest wavelength observed in the self-affine surface under study. This corresponds to a fractal discretization of the surface of the order of $10^3 \ /\mu m$ ($\lambda_s \approx 10$ nm). If one is instead

investigating the nominal contact pressure, mean contact pressure, or residual stress distribution inside the substrate, the fractal discretization of the surface can be an order less, i.e., $10^2/\mu$m, value at which the results converge.

4.3.5. AREA-LOAD DEPENDENCY

A quantity that has attracted much attention in the contact mechanics community is the proportionality coefficient κ, defined as $\kappa = a_\mathrm{r}/p^*$, where p^* is the reduced pressure expressed as $p^* = p_\mathrm{n}/E^*\bar{g}$. So far, the study of κ has been mostly limited to self-affine indentation of elastic bodies. It was shown that κ in elastic bodies follows a power law with respect to fractal discretization, i.e., $\kappa \propto \epsilon_\mathrm{f}^{0.67}$ (Prodanov et al., 2014). Pei $et.\ al.$ (Pei et al., 2005) performed simulations of rough surface contact using J_2 plasticity with isotropic hardening and found a larger value for κ for plasticity than for elasticity. Here we are interested to see how κ found for elastic simulations compares to that found by our dislocation dynamics simulations for various values of the fractal discretization, namely $2048^{-1} < \epsilon_\mathrm{f} < 1$, and whether our findings are in line with those of Pei $et.\ al.$ Pei et al. (2005). Notice that the simulations in this work are two-dimensional, but it was shown that the difference in κ between 2D and 3D simulations is only about 10% (van Dokkum et al., 2018). Here we can unfortunately not compare directly our κ with that of Pei $et.\ al.$ (Pei et al., 2005), because κ depends on various factors that are different in our simulations: Pei et al. (Pei et al., 2005) consider a softer material, a larger rms roughness, a significantly larger indentation depth, and they do not report the value of fractal discretization.

We present the evolution of relative contact area a_r with respect to the reduced pressure p^* in figure 4.16. The results are separated in two figures, one which includes the initial non-linear response and the other for the linear response at larger load. In figure 4.16(b) the curves for the plastically deforming crystals stop when the load reaches its maximum value, i.e. an additional increase in displacement will not lead to an increase in nominal contact pressure. Notice that, in accordance with the findings of Pei $et.\ al.$ Pei et al. (2005), the values of the slope κ are found to be larger for plastic than elastic crystals. Thus, for a given pressure, the contact area is larger if the crystal deforms plastically. Be reminded that for a given indentation depth, the opposite holds true: the contact area is larger if the bodies deform elastically (see figure 4.12).
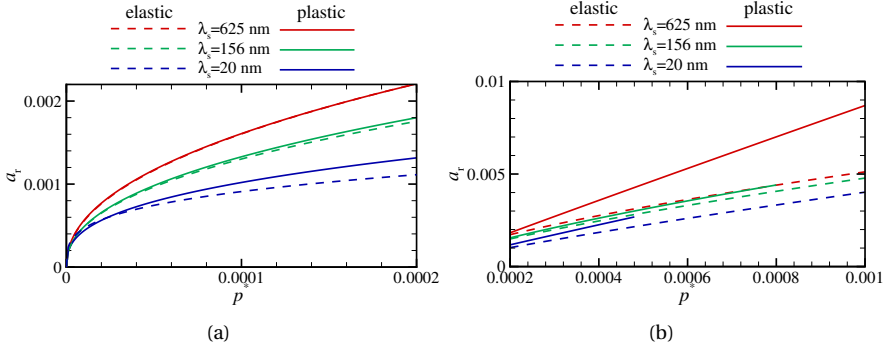
Figure 4.16: Contact area vs. reduced pressure for (a) $p^* < 0.0002$ and (b) $p^* > 0.0002$.

The dependency of the contact area fraction to the reduced pressure is found to be non-linear at the beginning of indentation ($p^* < 0.0002$) because the reduced pressure $p^* = \dfrac{p_n}{E^* \bar{g}}$ is here normalized, as usual, by the gradient of the indenter $\bar{g}$ whereas it is the gradient of the deformed surface $\bar{g}_c$ during indentation the quantity that determines the change of contact area with load. Therefore in the following we will use the actual gradient of the surface $\bar{g}_c$ calculated as:

$$\bar{g}_c^2 = \frac{1}{n_c} \left(\sum_{i=1}^{nx} \left(\frac{z_s^{i+1} - z_s^i}{a_0} \right)^2 \cdot (1 - \delta_{0, t_z^i}) \right), \tag{4.6}$$

where z_s^i is the location of the ith grid point and the number of contacting points is calculated as $n_c = \sum_{i=1}^{nx} (1 - \delta_{0, t_z^i})$, where $\delta_{\alpha\beta}$ is the Kronecker delta and t_z^i is the normal traction at the ith grid point. It can be seen from figure 4.17(a) that $\bar{g}/\bar{g}_c$ is large at small loading, causing the initial non-linear dependency. Also, the difference between $\bar{g}$ and $\bar{g}_c$ is larger for plastically deforming surfaces.[1]

In figure 4.17(b) one can see that using $\bar{g}_c$ instead of $\bar{g}$ results in a linear dependency of contact area on reduced pressure and all curves almost overlap leading to a universal value of $\kappa_c = 1.67 \pm 10\%$. It is noteworthy that this overlap does not indicate that there is no difference between elasticity and plasticity in terms of load-area dependency, just that this difference is now reflected in the actual gradient of the contact (see figure 4.17(a)).

---

[1]The difference in local and overall gradient for elastic contacts is significant only for linear contacts, while for surface contacts it is negligible (Müser, 2017; van Dokkum et al., 2018).
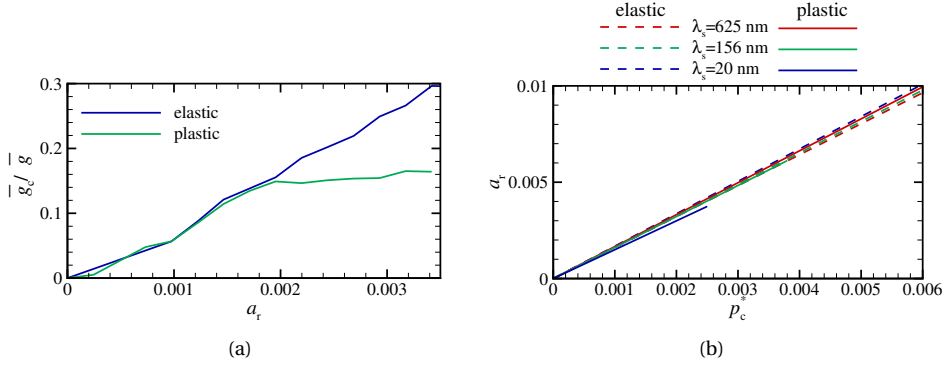
Figure 4.17: (a) Evolution of local gradient with respect to contact area for indentation of an elastic and plastic crystal using an indenter with $\lambda_s = 156$ nm. (b) Contact area vs. reduced pressure p_c^* for different values of λ_s.

In figure 4.18 the results for κ and κ_c are compiled for one of the realizations (a given set of sources and obstacle distribution). It can be seen that the difference in κ for the plastic and elastic crystals is lower with smaller fractal discretization. This is because the smaller the contact area the more plasticity is source limited. Here, we have also indicated a curve for κ_{eff}, which differs from κ only below the threshold $\epsilon_f = 64^{-1}$, since, as previously demonstrated, the effective contact area which determines the stress state in the body does not change below the threshold. It is seen that $\kappa_{\text{plas}}^{\text{eff}}/\kappa_{\text{elas}}^{\text{eff}} \to 2.4$.
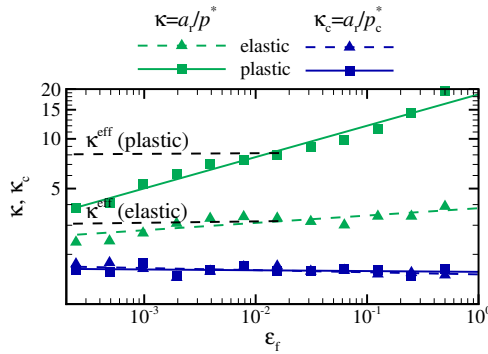
Figure 4.18: κ and κ_c are plotted for different fractal discretization.

4.4. CONCLUDING REMARKS

We modeled indentation of a metal single crystal by means of a self-affine rigid surface using Green's function dislocation dynamics (GFDD). The method provides an accurate description of plasticity by accounting for the collective glide of discrete dislocations as well as a detailed description of the self-affine roughness. Indentation is performed with a loading rate of $\dot{u}_z = 4 \times 10^3$ μm/s, which is found to be slow enough to ensure that the simulations are quasi-static. The simulations keep track of the changing contact area, the roughening of the metal surface, the pressure distribution, and of sub-surface plastic deformation. The results of the simulations lead us to the following observations and conclusions:

- By comparing the contact response of crystals with scaled dimensions indented by self-affine rough surfaces with similarly scaled topography, it is found that, although the elastic behavior is identical, the plastic response is not. Plasticity brings in a size effect, for which larger systems (thicker crystals indented deeper by surfaces with larger dimensions) deform plastically more than smaller systems, for which dislocation nucleation is source limited. This entails that the scaling of observables typically performed for elastic contact problems is not appropriate for plastically deforming crystals.

- At a given indentation depth a body that deforms plastically forms a smaller contact area with the indenter than one that deforms elastically. However, if the comparison is made at the same nominal contact pressure, the opposite holds true.

- Plastic deformation induces material pile-up. As a consequence, although at a given interference the contact area is smaller than that of a corresponding elastic crystal, the surface is more conforming to the indenter, for which the gap closure is larger. This is of relevance in problems related to leakage.

- The rms height is an important length in contact problems involving plasticity: the larger it is, the stronger the effect of plasticity. This is because a larger rms height induces a larger deviatoric stress component in the subsurface, and therefore earlier plasticity, although the elastic reduced contact pressure is the same.

- Although for elastic crystals the resistance to indentation increases with Hurst ex-

ponent, plasticity is marginally affected by H. At rather small interference the pressure–displacement curves for various H become indistinguishable. This entails that plasticity is more effective when the Hurst exponent is large.

- Indentation to an interference of 50 nm for various values of the fractal discretization has indicated that, although the actual contact area decreases with decreasing fractal discretization, the nominal contact pressure is constant below a threshold value for λ_s. We have shown that below that value, due to elastic interaction, the fragmented contact area acts as a continuous effective contact, whose length does not change with further decreasing true contact area and which causes a constant subsurface stress distribution. We conclude that if one is interested in either nominal or mean contact pressure at a given indentation, for either elastic or plastic contacts, it is not worthwhile to describe the surface with wavelengths below the threshold. In fact considering λ_s below the threshold is not only useless but deleterious: since true contact area decreases so does hardness, despite the subsurface stresses are invariant. On the contrary, when one is interested in real contact area, contact traction distribution, or gap geometry, the surface must be described with great accuracy, including the shortest wavelength present in the self-affine surface under study.

- The mean contact pressure (or contact hardness) at 20 nm is found to be significantly larger than in previous plasticity studies, up to $40\,\sigma_Y$, for the threshold value $\lambda_s = 156$ nm. The contact stiffness found with dislocation dynamics simulations is in between the elastic stiffness and the stiffness found by classical plasticity.

- The proportionality coefficient $\kappa = a_r/p^*$ strongly depends on fractal discretization. However, we find that $\kappa_{\text{plas}}^{\text{eff}}/\kappa_{\text{elas}}^{\text{eff}} \to 2.4$ for our choice of continuum and thermodynamic discretizations $\epsilon_c = 32^{-1}$ and $\epsilon_t = 2^{-1}$.

It is finally to be noted that the results presented in this work are based on a two-dimensional representation of the contact problem and cannot capture the dislocation structures that could form in three-dimensions. It is therefore not possible to estimate the effect of dislocation double cross-slip, which might be promoted by the large stresses acting in the contact regions and is observed in simulations of indentation modeled by three-dimensional dislocation dynamics (Gagel et al., 2016). Other limitations are that the

model only considers small deformations and studies the behavior of a pure single crystal.

REFERENCES

Balint, D., Deshpande, V., Needleman, A., der Giessen, E. V., 2006. Discrete dislocation plasticity analysis of the wedge indentation of films. Journal of the Mechanics and Physics of Solids 54 (11), 2281 – 2303.

Bouchaud, E., 1997. Scaling properties of cracks. Journal of Physics: Condensed Matter 9 (21), 4319.

Bouchaud, E., Lapasset, G., Planes, J., 1990. Fractal dimension of fractured surfaces: a universal value? EPL (Europhysics Letters) 13 (1), 73.

Campañá, C., Müser, M. H., 2007. Contact mechanics of real vs. randomly rough surfaces: A green's function molecular dynamics study. EPL (Europhysics Letters) 77 (3), 38005.

Campañá, C., Müser, M. H., Robbins, M. O., 2008. Elastic contact between self-affine surfaces: comparison of numerical stress and contact correlation functions with analytic predictions. Journal of Physics: Condensed Matter 20 (35), 354013.

Chang, W., Etsion, I., Bogy, D. B., 1987. An elastic-plastic model for the contact of rough surfaces. Journal of tribology 109 (2), 257–263.

Curtin, W. A., Miller, R. E., 2003. Atomistic/continuum coupling in computational materials science. Modelling and simulation in materials science and engineering 11 (3), R33.

Dapp, W., Prodanov, N., Müser, M., 2014. Systematic analysis of persson's contact mechanics theory of randomly rough elasticsurfaces. Journal of Physics Condensed Matter 26 (35).

Dapp, W. B., Lücke, A., Persson, B. N., Müser, M. H., 2012. Self-affine elastic contacts: percolation and leakage. Physical review letters 108 (24), 244301.

Dauskardt, R., Haubensak, F., Ritchie, R., 1990. On the interpretation of the fractal character of fracture surfaces. Acta Metallurgica et Materialia 38 (2), 143–159.

Deshpande, V., Balint, D., Needleman, A., Van der Giessen, E., 2007. Size effects in single asperity frictional contacts. Modelling and Simulation in Materials Science and Engineering 15 (1), 97–108.

Fivel, M. C., 2008. Discrete dislocation dynamics: an important recent break-through in the modelling of dislocation collective behaviour. Comptes Rendus Physique 9 (3-4), 427–436.

Fleck, N., Muller, G., Ashby, M., Hutchinson, J., 1994. Strain gradient plasticity: Theory and experiment. Acta Metallurgica et Materialia 42 (2), 475 – 487.

Gagel, J., Weygand, D., Gumbsch, P., 2016. Formation of extended prismatic dislocation structures under indentation. Acta Materialia 111, 399 – 406.

Gao, Y., Bower, A., Kim, K.-S., 2004. Some issues of rough surface contact plasticity at micro-and nano-scales. MRS Online Proceedings Library Archive 841.

Gao, Y., Bower, A., Kim, K.-S., Lev, L., Cheng, Y., 2006. The behavior of an elastic–perfectly plastic sinusoidal surface under contact loading. Wear 261 (2), 145–154.

Gao, Y.-F., Bower, A., 2006. Elastic–plastic contact of a rough surface with weierstrass profile. Proceedings of the Royal Society of London A: Mathematical, Physical and Engineering Sciences 462 (2065), 319–348.

Ghaednia, H., Wang, X., Saha, S., Xu, Y., Sharma, A., Jackson, R. L., 2017. A review of elastic–plastic contact mechanics. Applied Mechanics Reviews 69 (6), 060804.

Greer, J. R., Oliver, W. C., Nix, W. D., 2005. Size dependence of mechanical properties of gold at the micron scale in the absence of strain gradients. Acta Materialia 53 (6), 1821 – 1830.

Hyun, S., Pel, L., Molinari, J., Robbins, M., 2004. Finite-element analysis of contact between elastic self-affine surfaces. Physical Review E - Statistical, Nonlinear, and Soft Matter Physics 70 (2 2), 026117–1–026117–12.

Ilincic, S., Tungkunagorn, N., Vernes, A., Vorlaufer, G., Fotiu, P., Franek, F., 2011. Finite and boundary element method contact mechanics on rough, artificial hip joints. Proceedings of the Institution of Mechanical Engineers, Part J: Journal of Engineering Tribology 225 (11), 1081–1091.

Ilincic, S., Vorlaufer, G., Fotiu, P., Vernes, A., Franek, F., 2009. Combined finite element-boundary element method modelling of elastic multi-asperity contacts. Proceedings of the Institution of Mechanical Engineers, Part J: Journal of Engineering Tribology 223 (5), 767–776.

Imre, A., Pajkossy, T., Nyikos, L., 1992. Electrochemical determination of the fractal dimension of fractured surfaces. Acta metallurgica et materialia 40 (8), 1819–1826.

Khajeh Salehani, M., Irani, N., Müser, M., Nicola, L., 2018. Modelling coupled normal and tangential tractions in adhesive contacts. Tribology International 124, 93–101.

Krim, J., Palasantaz, G., 1995. Experimental observations of self-affine scaling and kinetic roughening at sub-micron lengthscales. International Journal of Modern Physics B 09 (06), 599–632.

Lechenault, F., Pallares, G., George, M., Rountree, C., Bouchaud, E., Ciccotti, M., 2010. Effects of finite probe size on self-affine roughness measurements. Physical review letters 104 (2), 025502.

Ma, Q., Clarke, D. R., Apr. 1995. Size dependent hardness of silver single crystals. Journal of Materials Research 10, 853–863.

Majumdar, A., Tien, C., 1990. Fractal characterization and simulation of rough surfaces. Wear 136 (2), 313–327.

Mandelbrot, B. B., Passoja, D. E., Paullay, A. J., 1984. Fractal character of fracture surfaces of metals. Nature Publishing Group.

Müser, M. H., Aug 2017. On the linearity of contact area and reduced pressure. Tribology Letters 65 (4), 129.

Müser, M. H., Dapp, W. B., Bugnicourt, R., Sainsot, P., Lesaffre, N., Lubrecht, T. A., Persson, B. N. J., Harris, K., Bennett, A., Schulze, K., Rohde, S., Ifju, P., Sawyer, W. G., Angelini, T., Ashtari Esfahani, H., Kadkhodaei, M., Akbarzadeh, S., Wu, J.-J., Vorlaufer, G., Vernes, A., Solhjoo, S., Vakis, A. I., Jackson, R. L., Xu, Y., Streator, J., Rostami, A., Dini, D., Medina, S., Carbone, G., Bottiglione, F., Afferrante, L., Monti, J., Pastewka, L., Robbins, M. O., Greenwood, J. A., Aug 2017. Meeting the contact-mechanics challenge. Tribology Letters 65 (4), 118.

Ng Wei Siang, K., Nicola, L., 2017. Static friction of sinusoidal surfaces: a discrete dislocation plasticity analysis. Philosophical Magazine 97 (29), 2597–2614.

Nicola, L., Bower, A., Kim, K.-S., Needleman, A., Van der Giessen, E., 2007. Surface versus bulk nucleation of dislocations during contact. Journal of the Mechanics and Physics of Solids 55 (6), 1120–1144.

Nicola, L., Bower, A., Kim, K.-S., Needleman, A., Van Der Giessen, E., 2008. Multi-asperity contact: A comparison between discrete dislocation and crystal plasticity predictions. Philosophical Magazine 88 (30-32), 3713–3729.

Nicola, L., der Giessen, E. V., Needleman, A., 2003. Discrete dislocation analysis of size effects in thin films. Journal of Applied Physics 93 (10), 5920–5928.

Nicola, L., Xiang, Y., Vlassak, J., der Giessen, E. V., Needleman, A., 2006. Plastic deformation of freestanding thin films: Experiments and modeling. Journal of the Mechanics and Physics of Solids 54 (10), 2089 – 2110.

Nix, W., Gao, H., 1998. Indentation size effects in crystalline materials: A law for strain gradient plasticity. Journal of the Mechanics and Physics of Solids 46 (3), 411–425.

Pei, L., Hyun, S., Molinari, J., Robbins, M. O., 2005. Finite element modeling of elasto-plastic contact between rough surfaces. Journal of the Mechanics and Physics of Solids 53 (11), 2385 – 2409.

Pérez-Ràfols, F., Larsson, R., Almqvist, A., 2016. Modelling of leakage on metal-to-metal seals. Tribology International 94, 421–427.

Persson, B. N. J., Aug 2001. Elastoplastic contact between randomly rough surfaces. Phys. Rev. Lett. 87, 116101.

Plouraboué, F., Boehm, M., 1999. Multi-scale roughness transfer in cold metal rolling. Tribology International 32 (1), 45 – 57.

Polonsky, I., Keer, L., 2000. Fast methods for solving rough contact problems: A comparative study. Journal of Tribology 122 (1), 36–41.

Prodanov, N., Dapp, W. B., Müser, M. H., Feb 2014. On the contact area and mean gap of rough, elastic contacts: Dimensional analysis, numerical corrections, and reference data. Tribology Letters 53 (2), 433–448.

Putignano, C., Afferrante, L., Carbone, G., Demelio, G., 2012a. The influence of the statistical properties of self-affine surfaces in elastic contacts: A numerical investigation. Journal of the Mechanics and Physics of Solids 60 (5), 973 – 982.

Putignano, C., Afferrante, L., Carbone, G., Demelio, G., 2012b. A new efficient numerical method for contact mechanics of rough surfaces. International Journal of Solids and Structures 49 (2), 338 – 343.

Stanley, H., Kato, T., 1997. An fft-based method for rough surface contact. Journal of Tribology 119 (3), 481–485.

Sun, F., der Giessen, E. V., Nicola, L., 2015. Interaction between neighboring asperities during flattening: A discrete dislocation plasticity analysis. Mechanics of Materials 90 (Supplement C), 157 – 165.

Sun, F., van der Giessen, E., Nicola, L., 2012. Plastic flattening of a sinusoidal metal surface: A discrete dislocation plasticity study. Wear 296, 672–680.

Sun, F., Van Der Giessen, E., Nicola, L., 2016. Dry frictional contact of metal asperities: A dislocation dynamics analysis. Acta Materialia 109, 162–169.

Swadener, J., George, E., Pharr, G., 2002. The correlation of the indentation size effect measured with indenters of various shapes. Journal of the Mechanics and Physics of Solids 50 (4), 681–694.

van der Giessen, E., Needleman, A., 1995. Discrete dislocation plasticity: a simple planar model. Modelling and Simulation in Materials Science and Engineering 3 (5), 689.

van Dokkum, J. S., Khajeh Salehani, M., Irani, N., Nicola, L., Aug 2018. On the proportionality between area and load in line contacts. Tribology Letters 66 (3), 115.

Venugopalan, S., Nicola, L., 2019. Indentation of a plastically deforming metal crystal with a self-affine rigid surface: A dislocation dynamics study. Acta Materialia 165, 709 – 721.

Venugopalan, S. P., Müser, M. H., Nicola, L., 2017a. Green's function molecular dynamics meets discrete dislocation plasticity. Modelling and Simulation in Materials Science and Engineering 25 (6), 065018.

Venugopalan, S. P., Nicola, L., Müser, M. H., 2017b. Green's function molecular dynamics: including finite heights, shear, and body fields. Modelling and Simulation in Materials Science and Engineering 25 (3), 034001.

Volkert, C. A., Lilleodden, E. T., 2006. Size effects in the deformation of sub-micron au columns. Philosophical Magazine 86 (33-35), 5567–5579.

Widjaja, A., Van der Giessen, E., Deshpande, V., Needleman, A., 2007. Contact area and size effects in discrete dislocation modeling of wedge indentation. Journal of Materials Research 22 (3), 655–663.

Wu, J.-J., 2006. Numerical analyses on elliptical adhesive contact. Journal of Physics D: Applied Physics 39 (9), 1899–1907.

Yin, X., Komvopoulos, K., 2012. A discrete dislocation plasticity analysis of a single-crystal semi-infinite medium indented by a rigid surface exhibiting multi-scale roughness. Philosophical Magazine 92 (24), 2984–3005.

Zhao, Y., Maietta, D. M., Chang, L., 2000. An asperity microcontact model incorporating the transition from elastic deformation to fully plastic flow. Journal of Tribology 122 (1), 86–93.

Zong, Z., Soboyejo, W., 2005. Indentation size effects in face centered cubic single crystal thin films. Materials Science and Engineering: A 404 (1-2), 281–290.

5

PLASTIC CONTACT OF SELF-AFFINE SURFACES: PERSSON'S THEORY VERSUS DISCRETE DISLOCATION PLASTICITY

This chapter is submitted for publication

Persson's theory allows for a fast and effective estimate of contact area and contact stress distributions when a flat and a self-affine rough surface are pressed into contact. For elastic bodies, the theory was shown to give results in very good agreement with rather costly simulations. The theory has also been extended to plastic bodies. Here, we compare the results of Persson's theory with those of discrete dislocation plasticity simulations. Results show that the area–to–load curves obtained by theory and simulations are in good agreement when the indenter has a very small rms height. For larger rms heights, which are more realistic for metal surfaces, the agreement is no longer good, unless one uses in the theory, instead of the size independent material strength the yield strength obtained through the dislocation dynamics simulations, which is rms height and resolution dependent. A modification of this type, i.e. the use of a yield strength dependent on size, does however not lead to agreement between the probability distributions of contact stress, which are broader in the simulations than in the theory. A possible reason is that the theory only accounts for elastically perfectly plastic bodies and therefore neglects strain hardening.

5.1. INTRODUCTION

In the past decades, numerous experiments have confirmed that surfaces have a self-affine fractal character down to the nanoscale (Bouchaud, 1997; Bouchaud et al., 1990; Dauskardt et al., 1990; Imre et al., 1992; Krim and Palasantaz, 1995; Lechenault et al., 2010; Majumdar and Tien, 1990; Mandelbrot et al., 1984; Plouraboué and Boehm, 1999). To account for this, Persson (Persson, 2001a) developed a contact model that includes the presence of roughness on successive length scales. His theory can predict at a given nominal pressure the contact area, contact stress distribution and interfacial separation of elastic bodies in good agreement with experiments (Lorenz and Persson, 2009a,b; Persson, 2001a). Persson's theory has also been extended to study plasticity (Persson, 2001b). However, to the best of the authors knowledge, the validity of Persson's theory has never been tested for metal surfaces that deform plastically. Here, we intend to test the theory by comparing its results with those of two-dimensional discrete dislocation plasticity simulations.

Metallic rough surfaces span various orders of length scales, with asperities as small as a few nano-meters. Already at the micro-scale, plasticity has been experimentally found to be size-dependent (Fleck et al., 1994; Greer et al., 2005; Ma and Clarke, 1995; Nicola et al., 2006; Volkert and Lilleodden, 2006). The size dependence entails that, differently from the elastic response, the plastic response does not scale with size. Although the size effect cannot be captured by classical plasticity which does not contain any material length scale it is captured by non-local plasticity theories (Nix and Gao, 1998; Song et al., 2017) and by numerical simulations of the type of discrete dislocation plasticity (DDP) (Nicola et al., 2007, 2008, 2003; Venugopalan and Nicola, 2019). The latter contains various length scales, including the dislocation Burgers vector, and the average spacing between dislocation sources and dislocation obstacles. Recently, (Venugopalan and Nicola, 2019) preformed dislocation dynamics simulations to study indentation of metal crystals by self-affine rigid indenters with various roughness parameters. Results showed indeed a size dependence when scaling the dimensions of the rough body: the pressure-displacement response does not scale and smaller bodies are stronger. This phenomenon is mostly caused by limited dislocation availability, i.e. when the stressed subsurface regions become too small, they no longer contain a sufficient amount of dislocation sources to sustain the plastic deformation. The same phenomenon is observed

in (Venugopalan and Nicola, 2019) when indenting a crystal with constant size with a surface with smaller root mean square roughness: if pressure is normalized on the root mean square slope and interference by the root mean square height, the results are elastically identical, but not plastically. The crystal indented by the largest rms-height is subjected to a broader stressed region underneath the surface and is more susceptible to plastic deformation and therefore softer.

In order to include size-dependent plasticity in his theory, Persson suggested to replace the constant material yield strength with a resolution-dependent yield strength, i.e. a yield strength that increases with decreasing the short wavelength cut-off λ_s (Persson, 2006). The exact dependence of yield strength on resolution was not specified and it might be inferred by comparison with dislocation dynamics simulations, if the results are otherwise in agreement.

Before proceeding with the comparison it is important to note that the DD simulations are based on the small strain and small slope approximation. This means that for rms heights realistic for metals one can only reach partial closure of the contact. Persson's original theory is instead exact at full contact and requires a correcting factor at partial contact (Dapp et al., 2014; Manners and Greenwood, 2006; Wang and Müser, 2017). Therefore, for the sake of comparison, we will start by showing results of DD simulations for a very small rms height, that allows to reach closure, but that is not observed in typical metal surfaces. This is the case for which the best agreement is found between simulation and theory. We will then see that for surfaces with rms height more realistic for metals, the agreement is much poorer.

5.2. FORMULATION OF THE PROBLEM

A rigid indenter with self-affine roughness is pressed into contact against a metallic slab of finite height, see figure 5.1.

The power spectrum of the indenter is

$$
\begin{aligned}
C(q) &= C_0 \left(\frac{q}{q_0} \right)^{-2(H+\frac{1}{2})} && \text{if } q_0 < q < q_s, \\
C(q) &= 0 && \text{else,}
\end{aligned}
\tag{5.1}
$$

where $q_0 = 2\pi/\lambda_l$ and $q_s = 2\pi/\lambda_s$ are the wavenumbers corresponding to the long and
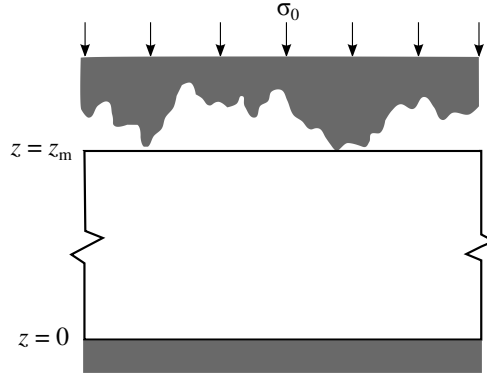
Figure 5.1: Schematic representation of the metal slab indented by a rough surface.

short wavelengths cut-offs, i.e. λ_l and λ_s, respectively. C_0 is determined by the root-mean-square (rms) height $\bar{h}$ as

$$\bar{h}^2 = 2 \int_{q_0}^{q_s} C(q)\, \mathrm{d}q. \tag{5.2}$$

Assuming $q_s >> q_0$ implies that

$$C_0 = \frac{H\bar{h}^2}{q_0}, \tag{5.3}$$

where H is the Hurst exponent. The power-law scaling for the surface height spectrum applies between cut-offs at long and short wave numbers $q_0 < q < q_s$.

The slab is taken to be elastically isotropic with Young's modulus $E = 70$ GPa and Poisson's ratio $\nu = 0.33$, representative values for aluminium. Moreover, it has a finite height z_m. The top surface of the crystal is frictionless at the points of contact, $\sigma_{xz}(x^c, z_m^c) = 0$, and traction-free elsewhere, $\sigma_{xz}(x^{nc}, z_m^{non}) = \sigma_{zz}(x^{non}, z_m^{non}) = 0$. The superscripts 'c' and 'non' stand for points 'in contact' and points 'not in contact', respectively. Furthermore, the bottom of the substrate is kept fixed: $u_x(x,0) = u_z(x,0) = 0$.

5.2.1. PERSSON'S THEORY FOR LINE CONTACTS IN SOLIDS WITH FINITE HEIGHT

Under the assumption that at resolution q the contact is full, Persson's theory (Persson, 2001a,b) states that on all length scales the distribution of contact stress σ is

$$P(\sigma, q) = \langle \delta(\sigma - \sigma_{nom}) \rangle. \tag{5.4}$$

Here, σ_{nom} is the nominal contact stress when the surface roughness with wavenumbers larger than q have been smoothed out and $\langle\dots\rangle$ stands for ensemble averaging over different surface roughness profiles. As finer roughness features are added, the contact stress distribution becomes $P(\sigma, q + \Delta q) = \langle\delta(\sigma - (\sigma_{\text{nom}} + \Delta\sigma))\rangle$. By expanding this equation to linear order in Δq

$$\frac{\partial P}{\partial q} = k(q)\,\frac{\partial^2 P}{\partial \sigma^2}, \tag{5.5}$$

where

$$k(q) = \frac{\langle\Delta\sigma^2\rangle}{2\,\Delta q}. \tag{5.6}$$

The partial differential Eq. 5.5 can be solved by imposing the following boundary conditions:

$$P(0, q) = 0, \tag{5.7a}$$

$$P(\sigma, 0) = \delta(\sigma - \sigma_0), \tag{5.7b}$$

$$P(\sigma_Y, q) = 0. \tag{5.7c}$$

The boundary conditions enforce that (5.7a) when the local contact stress reaches zero, contacting surfaces detach; (5.7b) at the lowest resolution, the stress distribution is a delta function; (5.7c) the contact stress does not exceed the yield strength σ_Y. Persson's theory for plasticity applies indeed to ideal elasto-plastic solids that display no work hardening. Notice that solving an elastic contact problem is equivalent to imposing $\sigma_Y \to \infty$ in Eq.5.7c.

Following (Persson, 2001a,b), the solution to Eq. (5.5) with boundary conditions (5.7a)-(5.7c) can be written as

$$P(\sigma, q) = \sum_{n=1}^{\infty} A_n(q)\sin\left(\frac{n\pi\sigma}{\sigma_Y}\right). \tag{5.8}$$

Substituting the expression above in Eq. (5.5) leads to the following partial differential equation:

$$\frac{\mathrm{d}A_n}{\mathrm{d}q} = -k(q)\left(\frac{n\pi}{\sigma_Y}\right)^2 A_n, \tag{5.9}$$

which after solution leads to

$$A_n(q) = \frac{2}{\sigma_{\mathrm{Y}}} \sin(\alpha_n) \exp\left[-\left(\frac{n\pi}{\sigma_{\mathrm{Y}}}\right)^2 \int_{q_0}^{q} k(q')\,\mathrm{d}q'\right]. \tag{5.10}$$

The full expression of the contact stress distribution is then given by

$$P(\sigma, q) = \frac{2}{\sigma_{\mathrm{Y}}} \sum_{n=1}^{\infty} \sin(\alpha_n) \exp\left[-\alpha_n^2 L(q)\right] \sin\left(\frac{n\pi\sigma}{\sigma_{\mathrm{Y}}}\right), \tag{5.11}$$

where $\alpha_n = \dfrac{n\pi\sigma_0}{\sigma_{\mathrm{Y}}}$ and $L(q) = \int_{q_0}^{q} \dfrac{k(q')}{\sigma_0^2}\,\mathrm{d}q'$. In order to solve Eq. (5.5), one must obtain $k(q)$ from $\Delta\sigma(q)$. It was shown by (Wang and Müser, 2017) that for elastic substrates with a finite height, $\Delta\sigma$ is given by

$$\Delta\sigma(q) = \sqrt{W(a_{\mathrm{r}})}\left(\frac{qE^* f(q)}{2}\right)|\tilde{h}(q)|, \tag{5.12}$$

where a_{r} is the relative contact area, and E^* is the effective elastic modulus. Moreover, $W(a_{\mathrm{r}})$ is the correction introduced by (Wang and Müser, 2017) for the low load regimes, i.e. when contact is partial. Furthermore, for frictionless elastic contacts, a substrate of height z_{m}, and a fixed bottom, $f(q)$ is given as (Venugopalan et al., 2017b)

$$f(q) = \frac{\cosh(2qz_{\mathrm{m}}) + 2(qz_{\mathrm{m}})^2 + 1}{\sinh(2qz_{\mathrm{m}}) - 2qz_{\mathrm{m}}}. \tag{5.13}$$

and

$$k(q) = \frac{\langle\Delta\sigma^2\rangle}{2\Delta q} = \frac{1}{2} W[a_{\mathrm{r}}(q)]\left(\frac{qE^* f(q)}{2}\right)^2 |\tilde{h}(q)|^2. \tag{5.14}$$

Finally, for the power spectrum $C(q)$ in this work

$$k(q) = \frac{H\bar{h}^2 q_0}{8} W(a_{\mathrm{r}})\left(E^* f(q)\right)^2 \left(\frac{q}{q_0}\right)^{1-2H}. \tag{5.15}$$

Having found $k(q)$, we may then proceed to solve the partial differential Eq. (5.5).

Subsequently, from the contact stress distribution $\mathrm{P}(\sigma, q)$, one can obtain the following quantities (Persson, 2001a,b):

(i) The fractions of macro-contact area which are not in contact A_{non}, which are in plastic

contact A_{pl}, and in elastic contact A_{el}:

$$
\begin{aligned}
A_{\mathrm{non}} &= \int_{q_0}^{q} k(q') \frac{\partial P}{\partial \sigma}(0, q') \, \mathrm{d}q' \\
&= \frac{2}{\pi} \sum_{n=1}^{\infty} \frac{\sin(\alpha_n)}{n} \left(1 - \exp\left[-\alpha_n^2 L(q)\right]\right), \\
A_{\mathrm{pl}} &= -\int_{q_0}^{q} k(q') \frac{\partial P}{\partial \sigma}(\sigma_{\mathrm{Y}}, q') \, \mathrm{d}q' \\
&= -\frac{2}{\pi} \sum_{n=1}^{\infty} (-1)^n \frac{\sin(\alpha_n)}{n} \left(1 - \exp\left[-\alpha_n^2 L(q)\right]\right), \\
A_{\mathrm{el}} &= 1 - A_{\mathrm{pl}} - A_{\mathrm{non}}.
\end{aligned}
\tag{5.16}
$$

(ii) The total relative contact area a_{r}, comprising both the area in elastic and plastic contact:

$$
a_{\mathrm{r}} = 1 - A_{\mathrm{non}}.
\tag{5.17}
$$

5.2.2. GREEN'S FUNCTION DISLOCATION DYNAMICS

The solution of the boundary value problem in figure 5.1 at each time step of the simulation is obtained by the superposition of two linear elastic solutions: The elastic analytical fields for dislocations in a homogeneous infinite solid, and the solution to the complementary elastic boundary-value problem, which corrects for the boundary conditions. The methodology is similar to (van der Giessen and Needleman, 1995), however, the solution to the complementary elastic boundary-value problem is obtained through Green's function molecular dynamics (GFMD) (Venugopalan et al., 2017a).

The schematics of the indented single crystal is shown in figure 5.2. Indentation is performed by applying the displacement U_z on top of the rigid indenter from which the value of the equivalent applied pressure σ_0 is obtained.

Following (van der Giessen and Needleman, 1995), the dislocation dynamics are controlled by constitutive rules inspired by atomic scale phenomena that control the nucleation and glide of the dislocations. The crystal is initially dislocation free, and contains a given density of slip planes, dislocation sources, and obstacles that are randomly distributed. When the stress in the body reaches the nucleation strength $\bar{\tau}_{\mathrm{nuc}}$ on a dislocation source for a given amount of time t_{nuc}, a dislocation dipole is nucleated from the
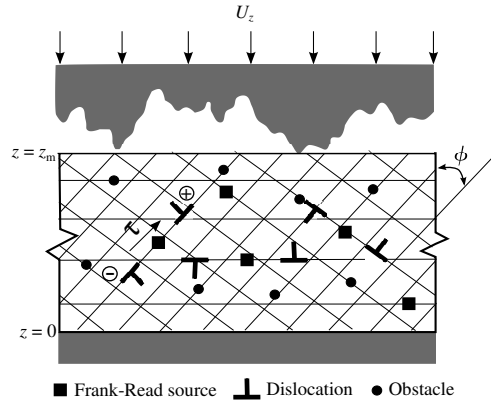
Figure 5.2: Schematic representation of the metal crystal indented by a rough surface.

sources and glides on the slip plane resulting in plastic deformation. The velocity with which dislocations glide is controlled by the Peach-Koehler force acting on them. Dislocations are stopped by the obstacles, but released when the resolved shear stress on them exceeds the critical strength associated to the obstacle, τ_{obs}.

CHOICE OF PARAMETERS FOR THE SIMULATIONS

Dislocations are nucleated from randomly distributed nucleation sources on slip planes oriented at $\phi = 60°$, $-60°$, and $90°$ with respect to the loading direction. The simulations are performed for a nucleation source density $\rho_{\mathrm{nuc}} = 40\ \mu\mathrm{m}^{-2}$. In both cases, the sources have a Gaussian strength distribution with the mean strength being $\bar{\tau}_{\mathrm{nuc}} = 50$ MPa. The nucleation time $t_{\mathrm{nuc}} = 10$ ns. The density of obstacles is $\rho_{\mathrm{obs}} = 40\ \mu\mathrm{m}^{-2}$ and the obstacle strength is $\tau_{\mathrm{obs}} = 150$ MPa. The drag coefficient for glide is $B = 10^{-4}$ Pa s and the critical distance for annihilation is $L_{\mathrm{e}} = 6b$, where $b = 2.5 \times 10^{-4}\ \mu\mathrm{m}$ is the magnitude of the Burgers vector. Moreover, in all calculations a time step of $\Delta t = 2.5$ ns is employed. The GFDD simulations are performed for 10 realizations of nucleation source and obstacle distributions. In the following, the presented results are obtained by averaging over these 10 realizations.

The roughness of the indenter is obtained using the power spectral density method (Campañá et al., 2008). The power spectrum $C(q)$ is used to construct a periodic self-affine surface with a Gaussian height distribution. The Fourier transform of the height profile

$h(r)$ of the indenter is given as:

$$\tilde{h}(q) = h_0 \, \tilde{\Delta}_{\mathrm{G}}(q) \sqrt{C(q)} = h_0 \, \frac{\tilde{\Delta}_{\mathrm{G}}(q)}{q^{\left(\frac{1}{2} + H\right)}}, \qquad (5.18)$$

where h_0 is a real-valued constant which can be adjusted to obtain the required rms slope of the surface, $\tilde{\Delta}_{\mathrm{G}}(q)$ is a Gaussian random variable with random phase such that $\langle \tilde{\Delta}_{\mathrm{G}}(q) \rangle = 0$, and H is the Hurst exponent. For different realizations of the rough surface, all parameters, including the cut-off values, are kept fixed except the Gaussian random variable $\tilde{\Delta}_{\mathrm{G}}(q)$ whose phase is randomly varied. Furthermore, before starting the simulations the surfaces so generated are shifted such that the lowest point touches the substrate at zero interfacial pressure. The thermodynamic, fractal, and continuum discretizations are set to $\epsilon_{\mathrm{t}}^{-1} = 2$ and $\epsilon_{\mathrm{c}}^{-1} = 32$, respectively. We selected for the Hurst exponent the value $H = 0.8$, as observed for most metallic surfaces (Bouchaud et al., 1990; Dauskardt et al., 1990). The long wavelength cut-off λ_{l} is kept constant and equal to 10 μm. The short wavelength cut-off is changed in the simulations, to represent a change in the resolution in Persson's theory. The rms height values considered are $\bar{h} = 0.001$, 0.01, and 0.1 μm, the latter being the most realistic for metal surfaces.

5.2.3. The yield strength

While in Persson's theory the yield stress is an input to the calculation, in discrete dislocation plasticity it is an output. To calculate it, we perform a uniaxial tensile loading simulation on a single crystal with the material properties mentioned above. The dimensions of the crystal are $L = 12.5$ μm and $W = 5$ μm are selected to be large enough to not experience size effects. The schematics of the uniaxial tensile test is shown in figure 5.3(a). The predicted nominal tensile stress versus applied strain $\varepsilon = 2 U_x / L$ is presented in figure 5.3(b). This figure shows that the tensile yield strength of the crystal is $\sigma_{\mathrm{Y}}^{\mathrm{Tensile}} = 60$ MPa. It is important to highlight that the yield strength identified with $\sigma_{\mathrm{Y}}^{\mathrm{Tensile}}$ here and in all the manuscript is a size-independent quantity.
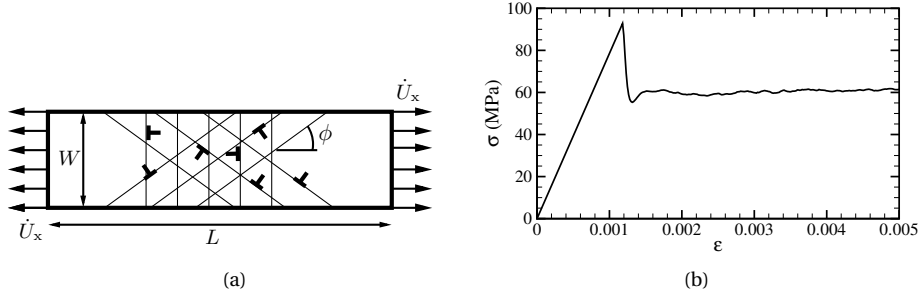
Figure 5.3: (a) Schematics of the uniaxial tensile test. (b) Uniaxial tensile stress-strain ($\sigma - \varepsilon$) curve from discrete dislocation plasticity.

5.3. PERSSON'S THEORY: CORRECTING FACTOR AT LOW LOADS FOR VARIOUS FRACTAL DISCRETIZATIONS

The expression for the elastic energy in Persson's theory was corrected by (Wang and Müser, 2017) to hold at low loads. The correcting factor in the fractal limit, $\lambda_s \to 0$, was given by the authors as

$$W[a_r(\sigma_0^*)] = 1 + c_1(1 - a_r(\sigma_0^*)^2) + c_2(1 - a_r(\sigma_0^*)^4), \tag{5.19}$$

where $\sigma_0^* = \dfrac{\sigma_0}{E^* \bar{g}}$ is the reduced pressure, σ_0 is the applied pressure and $\bar{g}$ is the root-mean-square gradient of the indenter. Selecting the values of 2/9 and -2/3 for the constants c_1 and c_2 leads to good correspondence between Persson's theory and GFMD simulations.

In this work, we intend to consider fractal discretizations also far from the limit, namely $\epsilon_f = 64^{-1}, 32^{-1},$ or 16^{-1}. To this end, we first proceed to check to which extent the correction factor is independent of fractal discretization, by comparing in figure 5.4(a) the results of Persson's theory with our GFMD calculations for an indenter with rms height $\bar{h} = 0.001 \ \mu$m. The results of the relative contact area a_r versus applied load in figure 5.4(a) show that there is a small discrepancy between GFMD and Persson's theory at intermediate load. This corresponds for the larger discretization to a non-negligible difference in the probability distribution of the contact stress P(σ^*), as shown in figure 5.4(b).

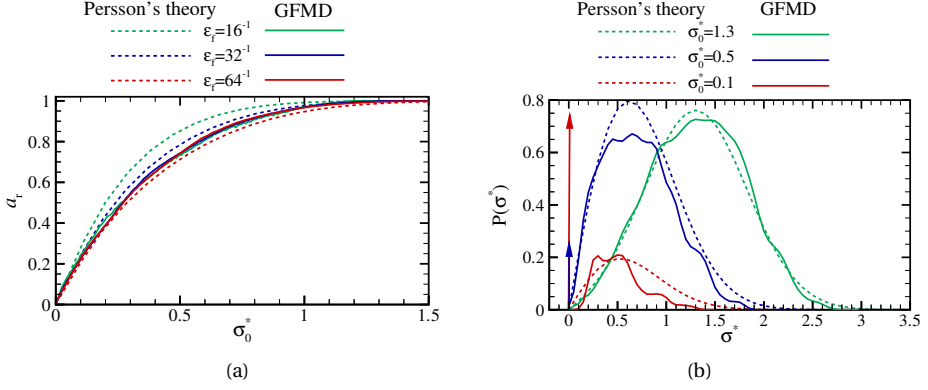To assure that at least our elastic simulations well compare with Persson's theory, we

Figure 5.4: (a) Relative contact area a_r against reduced applied pressure σ_0^* for indenters with $\bar{h} = 0.001 \ \mu$m and three fractal discretizations ϵ_f. (b) Probability distribution of reduced contact stress σ^* for an indenter with $\epsilon_f = 16^{-1}$ at three instances of applied pressure $\sigma_0^* = 0.1$, 0.5 and 1.3.

proceed to search for the c_1 and c_2 coefficients that minimize the difference between the area–load curves for theory and simulations. The values are listed in table 5.1 and lead to the correction factors in figure 5.5(a) and to the contact stress distributions in figure 5.5(b).

Table 5.1: Coefficients c_1 and c_2 in Eq. (5.19)

	$\epsilon_f = 16^{-1}$	$\epsilon_f = 32^{-1}$	$\epsilon_f = 64^{-1}$
c_1	-2.3	-0.6	0.19
c_2	1.9	0.2	-0.6

We have verified that the correction factors $W(a_r)$ found for indenters with rms height $\bar{h} = 0.001 \ \mu$m are appropriate also for the other rms heights used in this work, and are therefore used throughout the manuscript.

5.4. COMPARISON BETWEEN THEORY AND SIMULATIONS FOR INDENTERS WITH SMALL RMS HEIGHT

We start by comparing Persson's theory with DD simulations for the indentation of a metal crystal by a rigid indenter with surface roughness with $\bar{h} = 0.001 \ \mu$m and fractal discretization $\epsilon_f^{-1} = 64$. This allows to reach almost full closure with dislocation dynamics simulations while still obeying the small strain and small slope approximations. In
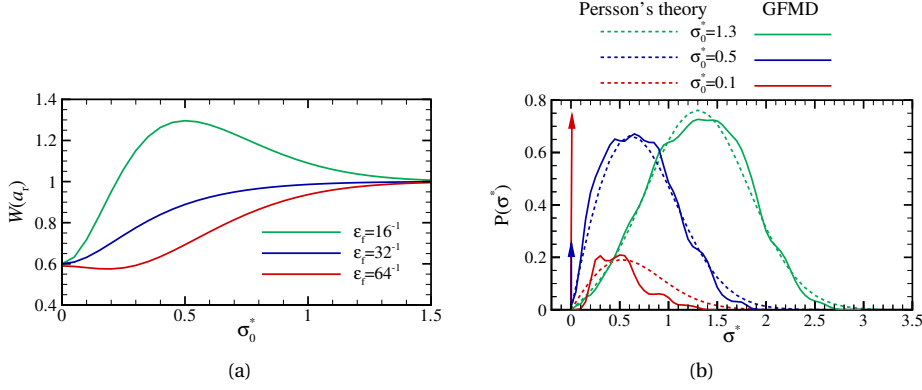
Figure 5.5: (a) The correction factor $W(a_r)$ for three different fractal discretizations ϵ_f.(b) Probability distribution of reduced contact stress σ^* for an indenter with $\epsilon_f = 16^{-1}$ at three instances of applied pressure $\sigma_0^* = 0.1$, 0.5 and 1.3.

Persson's plasticity theory, the yield strength σ_Y is an input parameter, which has been interpreted as either the tensile yield strength of the material $\sigma_Y^{\text{Tensile}}$ or the macroscopic indentation hardness, estimated by (Johnson, 1987) to be $3\sigma_Y^{\text{Tensile}}$. Through comparison with the simulations we check which of the two definitions is most appropriate and found from figure 5.6(a) that there is a much better agreement between the area–load curves when hardness is used for the definition of σ_Y.

Figure 5.6: Relative contact area a_r calculated using GFDD and modified-Persson's theory. In the latter, yield stresses $\sigma_Y = \sigma_Y^{\text{Tensile}}$ and $3\sigma_Y^{\text{Tensile}}$ were applied as an input.

Figure 5.6(b) shows, together with the total contact area, also how the elastic a_r^{elas} and plastic contact areas a_r^{plas} change with load. It is thus possible to see that the por-

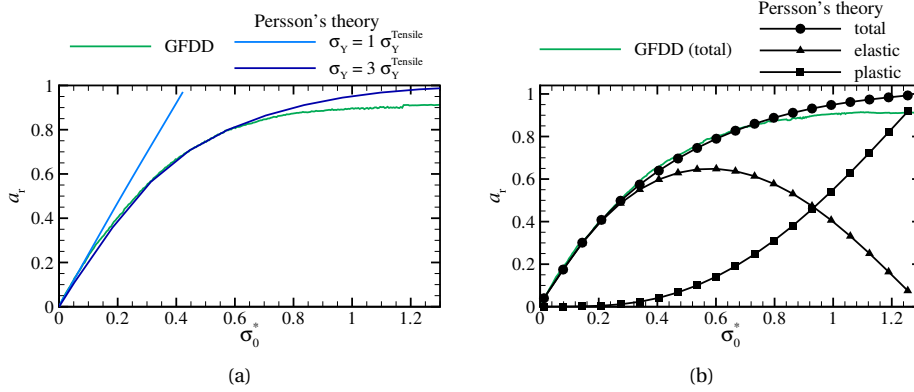tion of contact undergoing elastic deformations $a_{\mathrm{r}}^{\mathrm{elas}}$ initially increases with load σ_0^* and then decreases with increasing plasticity. The relative plastic contact area $a_{\mathrm{r}}^{\mathrm{plas}}$, instead, continues to increase with load until the external load reaches $\sigma_0^* = 1.3$. This load corresponds to the point at which the contact stress is everywhere plastic and equal to $\sigma = \sigma_{\mathrm{Y}}$. Notice that the contact in dislocation dynamics simulations never reach full closure, as can be seen from the decrease of the interfacial gap in figure 5.7(a) and a snapshot of the interface at $\sigma_0^* = 1.3$ in figure 5.7(b). The depth of the valleys formed during deformation can be as large as the rms height $\bar{h}$ of the indenter. This is in agreement with the observation of Bowden (Bowden and Tabor, 2001) according to whom full closure is impossible for rough metal surfaces due to work hardening.

(a)   (b)
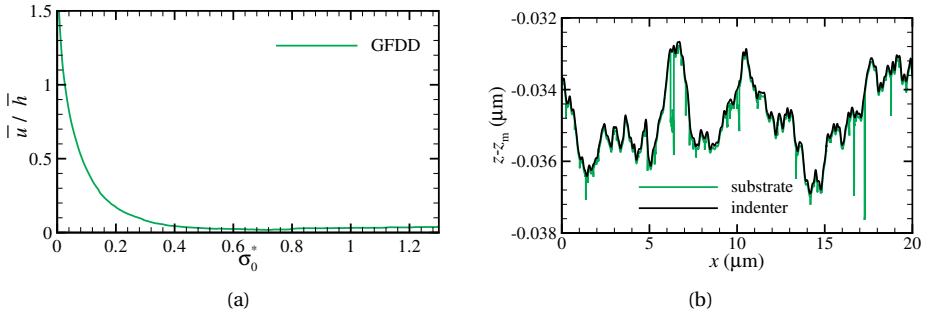
Figure 5.7: (a) The average interfacial separation $\bar{u}/\bar{h}$ are plotted against reduced applied pressure σ_0^* for the case of an indenter with $\bar{h} = 0.001~\mu$m and $\epsilon_{\mathrm{f}}^{-1} = 64$. The input yield stress to Persson's theory is $\sigma_{\mathrm{Y}} = 3\,\sigma_{\mathrm{Y}}^{\mathrm{Tensile}}$. (b) The snapshot of the contact between the indenter and the substrate at $\sigma_0^* = 1.3$.

Figure 5.8 presents the distribution of contact stress for three instances of the applied pressure, $\sigma_0^* = 0.1$, 0.5, and 1.3. The probability distribution function representing the plastic part of the contact is a delta peak at $\sigma^* = \sigma_{\mathrm{Y}}^*$. The other delta peak at $\sigma^* = 0$ represents the part of the surface which is out of contact. Hence, according to Persson's theory, the area under the probability distribution curve is the elastic fraction of the contact area $a_{\mathrm{r}}^{\mathrm{elas}}$. This is different from the distribution function obtained through GFDD simulations, where the area under the curves represents the total area in contact a_{r}: elastic and plastic contact areas are not distinguished, nor distinguishable, deformation is everywhere at the contact only 'partially plastic'. Therefore, agreement between the contact stress distribution obtained by Persson's theory and by the GFMD simulations ceases to be good when plasticity becomes relevant. The simulations predict a much broader

stress distribution, with contact stresses larger and smaller than the macroscopic hardness. The reason for this discrepancy can be partly attributed to the fact that Persson's plasticity theory does not account for material hardening. A better agreement with the simulations would be found, in our opinion, if the theory would be slightly modified by making σ_Y^* increase with plastic deformation. The plastic peak will then shift to the right during indentation and the elastic contribution would become more pronounced than it is now.
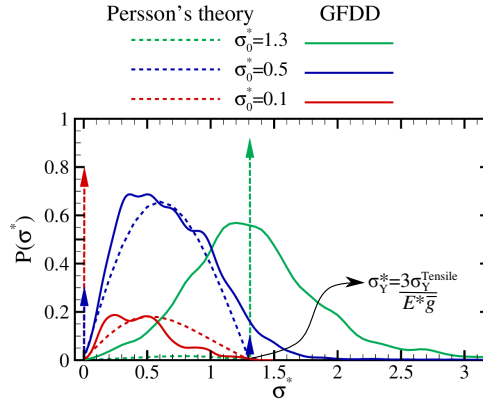
Figure 5.8: Probability distribution of contact stress σ^* at three instances of loading, $\sigma_0^* = 0.1$, 0.5, and 1.3, for an indenter with $\bar{h} = 0.001 \ \mu$m and $\epsilon_f^{-1} = 64$.

5.4.1. SIZE DEPENDENCE

It was shown by (Venugopalan and Nicola, 2019) that, although it is well known that indenters with different rms heights give rise to the same reduced pressure when indenting a metal crystal to the same reduced interference, they induce a different plastic response. The smaller the rms height the later the onset of plastic deformation. This plasticity size dependence occurs because the size of the subsurface region where the dislocation nucleation strength is exceeded scales with rms height, but the availability of dislocation sources does not scale accordingly: the spacing between dislocation sources is a material parameter which is scale independent. This is why a larger reduced pressure is required to induce nucleation in the case of a small rms height. The reduced pressure versus reduced interference for the indentation by three indenters of rms heights $\bar{h}$=0.001, 0.01 and 0.1, are shown here for completeness together with the corresponding mean contact

pressure displacement curves (see figure 5.9).
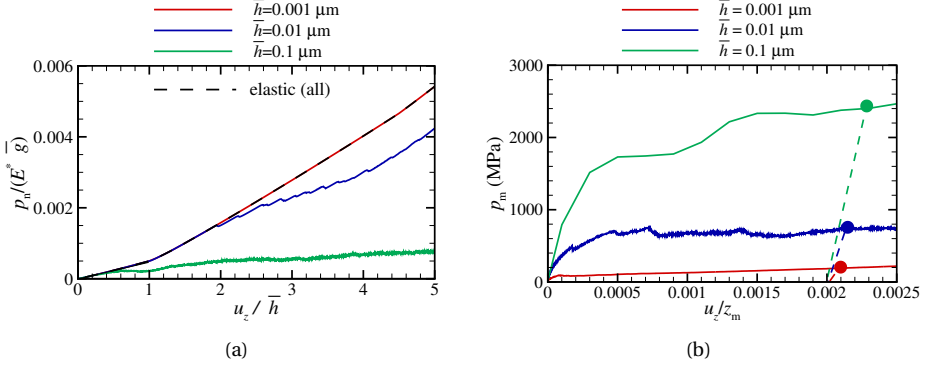
Figure 5.9: (a) Reduced pressure and (b) mean contact pressure are plotted against reduced interference for three different rms heights.

The relative contact area a_r, as calculated by GFDD and modified Persson's theory, are shown in figure 5.10 for an indenter with $\epsilon_f = 64^{-1}$. For all indenters, the input yield stress to Persson's theory is assumed to be $3\,\sigma_Y^{\text{Tensile}}$. It can be seen that under this assumption, the contact area as predicted by the theory and GFDD are very different from each other when $\bar{h} = 0.01\,\mu$m.
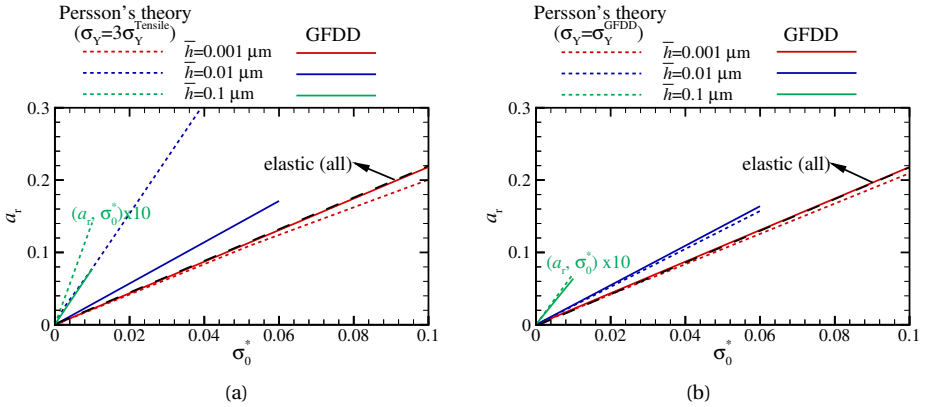
Figure 5.10: (a) Relative contact area a_r against reduced applied pressure σ_0^* for an indenter with $\epsilon_f = 64^{-1}$ and three rms heights $\bar{h}$. The input yield stress to Persson's theory is $3\,\sigma_Y^{\text{Tensile}}$. (b) The input yield stress to Persson's theory is the indentation flow strength obtained through GFDD calculations.

It is noteworthy that scaling rms height corresponds to a shift in the power spectrum of the roughness, and has no influence on the range of wavelength considered in the

problem, both large and small wavelength are the same. Already this observation is sufficient to conclude that considering a resolution-dependent yield strength in Persson's theory, $\sigma(\lambda_s)$, would not improve agreement between simulations and theory. Instead one can see in figure 5.10b that if the flow stress value obtained through dislocation dynamics simulations, σ_Y^{GFDD}=12.3MPa, is used as the input yield strength σ_Y in Persson's theory a much better agreement is found for the load–displacement curves. However, this type of fix is not sufficient to obtain agreement between the probability distributions of the contact stress, as one can see from fig. 5.11, where the probability distribution is shown for the simulations and for Persson's theory with and without correction for σ_Y. While the fix gives agreement between the areas that are not in contact, the simulations show a much larger probability to have smaller as well as larger contact stresses when compared to the theory.
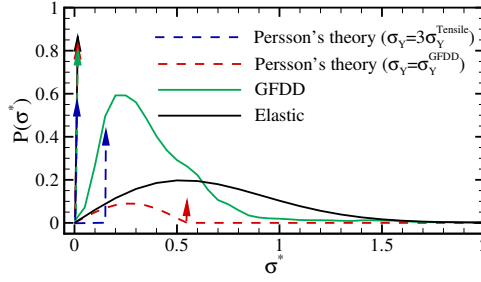
Figure 5.11: Probability distribution of contact stress σ^* for different yield strength as input to Persson's theory compared to GFDD for indentation using $\bar{h} = 0.01$ μm at $\sigma_0^* = 0.06$.

(a)

(b)

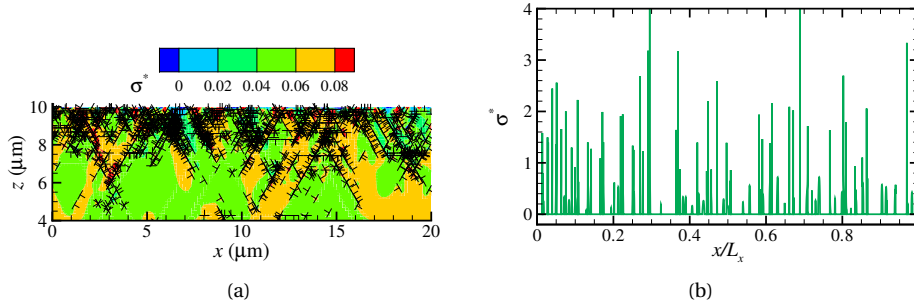Figure 5.12: (a) Dislocation distribution and stress contours $\dfrac{\sigma_{zz}}{\sigma_Y}$ and (b) surface tractions $\dfrac{t}{\sigma_Y}$ for indentation using $\bar{h} = 0.01$ μm at $\sigma_0^* = 0.06$.

5.4.2. EFFECT OF SHORT-WAVELENGTH CUT-OFF

In this section we perform simulations for different roughness resolution by changing the small wavelength, while keeping the large wavelength constant. This corresponds to changing the fractal discretization ϵ_f. It is noteworthy that changing resolution does not correspond to scaling the contact problem. Changing resolution involves extending the range between small and large wavelength, i.e. adding smaller wavelengths to the surface, and therefore results in a different boundary value problem, with a different elastic and thus plastic response. Such simulations are therefore not suitable to evidentiate a plasticity size dependence. They might however give an indication on how suitable it is to replace σ_Y in Persson's theory with $\sigma_Y(\lambda_s)$, as suggested in (Persson, 2006).
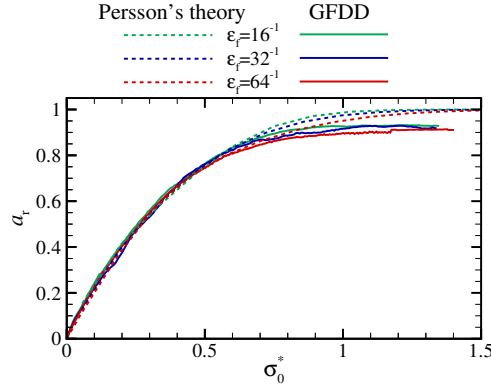
Figure 5.13: Relative contact area a_r against reduced applied pressure σ_0^* for indenters with $\bar{h} = 0.001$ μm and three fractal discretizations ϵ_f.

Figure 5.13 shows the increase of the relative contact area a_r with load for indenters with $\bar{h} = 0.001$ μm and three fractal discretizations. The curves are insensitive to a change in λ_s suggesting against the use of a resolution-dependent σ_Y. For all resolutions there is a good agreement between simulations and theory. If one instead considers indenters with $\bar{h} = 0.01$ μm the agreement is poor for all discretizations (see figure 5.14a). The agreement improves if again, instead of using $\sigma_Y = 3\,\sigma_Y^{\text{Tensile}}$ we replace it by $\sigma_Y = \sigma_Y^{\text{GFDD}}$ (see figure 5.14). Given that σ_Y^{GFDD} is resolution-dependent, we conclude that indeed a $\sigma_Y(\lambda_s)$ should be used, as suggested in (Persson, 2006). However, the use of a resolution-dependent σ_Y is not sufficient to obtain the agreement between the probability distributions, as one can see in figure 5.15(b). Also, much more important than the dependence of σ_Y on resolution appears the dependence of σ_Y on rms height.
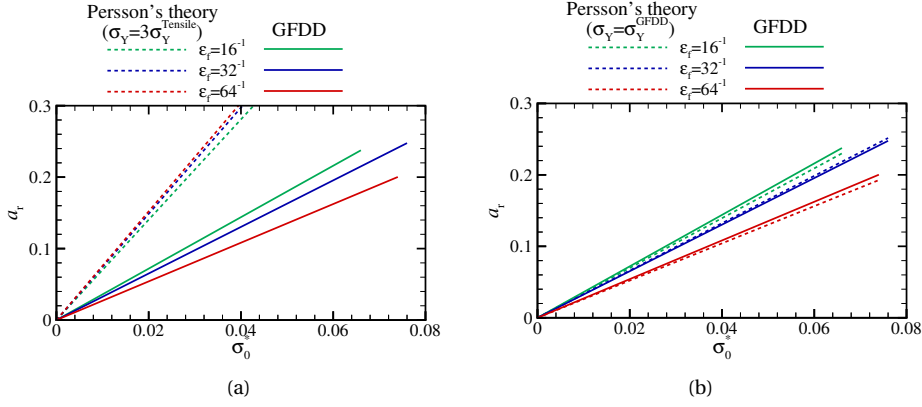
Figure 5.14: Relative contact area a_r against reduced applied pressure σ_0^* for indenters with $\bar{h} = 0.01$ μm and three fractal discretizations ϵ_f. The input yield stress for Persson's theory is taken as (a) $\sigma_Y = 3\,\sigma_Y^{Tensile}$ (b) $\sigma_Y = \sigma_Y^{GFDD}$.
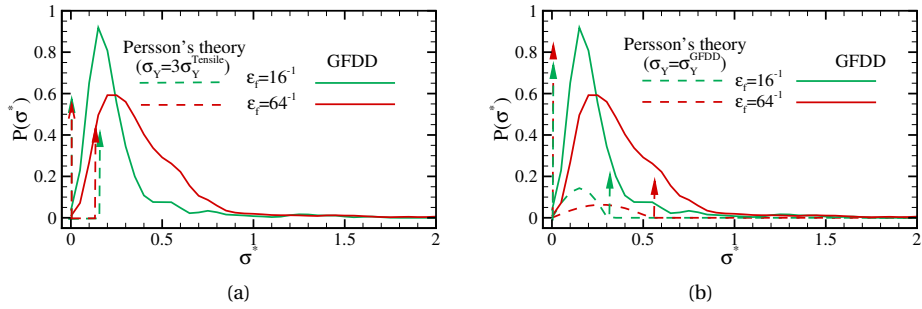
Figure 5.15: Probability distribution of contact stress σ^* for different fractal discretizations ϵ_f for indentation for $\bar{h} = 0.01$ μm at $\sigma_0^* = 0.06$. The input yield stress for Persson's theory is taken as (a) $\sigma_Y = 3\,\sigma_Y^{Tensile}$ (b) $\sigma_Y = \sigma_Y^{GFDD}$.

Here, a table is provided of the flow strength σ_Y^{GFDD} found through GFDD simulations and that allow for good agreement for similar curves in Persson's theory. [1]

Table 5.2: Normalized yield strength $\sigma_Y^{\text{GFDD}}/3\sigma_Y^{\text{Tensile}}$

rms height	$\epsilon_f = 4^{-1}$	$\epsilon_f = 8^{-1}$	$\epsilon_f = 16^{-1}$	$\epsilon_f = 32^{-1}$	$\epsilon_f = 64^{-1}$
$\bar{h} = 0.01\ \mu\text{m}$	1.4	1.7	2.0	2.7	4.1
$\bar{h} = 0.1\ \mu\text{m}$	3	4.7	9.5	10.6	13.3

5.5. CONCLUDING REMARKS

In this chapter we have shown a comparison between dislocation dynamics simulations and Persson's theory in the study of indentation of a metal flat body by a rigid indenter with self-affine roughness. Although there is good agreement between simulations and theory when the metal behaves elastically, the agreement ceases to be good when there is plasticity. The best agreement for the area–load curves is found for small values of the rms height, when the response is almost size independent. With decreasing rms height the onset of plasticity in dislocation dynamics simulations is delayed, because there are only few dislocation sources in the subsurface region where the stress concentration is sufficiently large to induce dislocation nucleation. A good agreement between the area–load curves obtained through simulations and theory is obtained if the size independent yield stress in the theory is replaced by the yield strength obtained through the simulations. The yield strength obtained through the simulations depends very strongly on rms height, and on the resolution.

The necessity of using a resolution-dependent yield stress in his plasticity theory was already explicitly mentioned by Persson. The fix is indeed important, because the plastic response depends on resolution. However, if one wants to believe the simulations (of course we are well aware that they have limitations too, one being that they are two dimensional), the fix is not sufficient. This is because it does not account for the plasticity size dependence that is observed when the system of analysis is scaled such as to become elastically equivalent. To account for this the yield stress should also become dependent on a scaling length in the problem.

---

[1] It has to be noted that for $\bar{h} = 0.001\ \mu\text{m}$, the contact approaches full closure readily and hence the response displays hardening. Consequently, the flow stress cannot be obtained from the GFDD simulations.

Another point that is important to consider is that, although we found good agreement for area–load curves, when using Persson's theory with the yield strength obtained through dislocation dynamics (i.e. a yield strength that depends on rms height and resolution) the contact stress probability distribution is still markedly different. The simulations predict a much broader contact stress distribution compared with the theory. This is because in the theory the material behaves as perfectly plastic, without any strain hardening. A possible improvement of the theory might be to use, instead of a constant yield strength, a yield strength that increases with plastic deformation. This would translate in a plastic peak in the probability distribution that moves towards larger pressures with increasing closure of the contact and a broader distribution in stresses of the elastic part of the contact.

ACKNOWLEDGEMENT

REFERENCES

Bouchaud, E., 1997. Scaling properties of cracks. Journal of Physics: Condensed Matter 9 (21), 4319.

Bouchaud, E., Lapasset, G., Planes, J., 1990. Fractal dimension of fractured surfaces: a universal value? EPL (Europhysics Letters) 13 (1), 73.

Bowden, F., Tabor, D., 2001. The Friction and Lubrication of Solids. No. v. 1 in Oxford Classic Texts in the Ph. Clarendon Press.

Campañá, C., Müser, M. H., Robbins, M. O., 2008. Elastic contact between self-affine surfaces: comparison of numerical stress and contact correlation functions with analytic predictions. Journal of Physics: Condensed Matter 20 (35), 354013.

Dapp, W., Prodanov, N., Müser, M., 2014. Systematic analysis of persson's contact me-

chanics theory of randomly rough elasticsurfaces. Journal of Physics Condensed Matter 26 (35).

Dauskardt, R., Haubensak, F., Ritchie, R., 1990. On the interpretation of the fractal character of fracture surfaces. Acta Metallurgica et Materialia 38 (2), 143–159.

Fleck, N., Muller, G., Ashby, M., Hutchinson, J., 1994. Strain gradient plasticity: Theory and experiment. Acta Metallurgica et Materialia 42 (2), 475 – 487.

Greer, J. R., Oliver, W. C., Nix, W. D., 2005. Size dependence of mechanical properties of gold at the micron scale in the absence of strain gradients. Acta Materialia 53 (6), 1821 – 1830.

Imre, A., Pajkossy, T., Nyikos, L., 1992. Electrochemical determination of the fractal dimension of fractured surfaces. Acta metallurgica et materialia 40 (8), 1819–1826.

Johnson, K., 1987. Contact Mechanics. Cambridge University Press.

Krim, J., Palasantaz, G., 1995. Experimental observations of self-affine scaling and kinetic roughening at sub-micron lengthscales. International Journal of Modern Physics B 09 (06), 599–632.

Lechenault, F., Pallares, G., George, M., Rountree, C., Bouchaud, E., Ciccotti, M., 2010. Effects of finite probe size on self-affine roughness measurements. Physical review letters 104 (2), 025502.

Lorenz, B., Persson, B., 2009a. Leak rate of seals: Comparison of theory with experiment. EPL (Europhysics Letters) 86 (4), 44006.

Lorenz, B., Persson, B. N. J., 2009b. Interfacial separation between elastic solids with randomly rough surfaces: comparison of experiment with theory. Journal of Physics: Condensed Matter 21 (1), 015003.

Ma, Q., Clarke, D. R., Apr. 1995. Size dependent hardness of silver single crystals. Journal of Materials Research 10, 853–863.

Majumdar, A., Tien, C., 1990. Fractal characterization and simulation of rough surfaces. Wear 136 (2), 313–327.

Mandelbrot, B. B., Passoja, D. E., Paullay, A. J., 1984. Fractal character of fracture surfaces of metals. Nature Publishing Group.

Manners, W., Greenwood, J., 2006. Some observations on persson's diffusion theory of elastic contact. Wear 261 (5), 600 – 610.

Nicola, L., Bower, A., Kim, K.-S., Needleman, A., Van der Giessen, E., 2007. Surface versus bulk nucleation of dislocations during contact. Journal of the Mechanics and Physics of Solids 55 (6), 1120–1144.

Nicola, L., Bower, A., Kim, K.-S., Needleman, A., Van Der Giessen, E., 2008. Multi-asperity contact: A comparison between discrete dislocation and crystal plasticity predictions. Philosophical Magazine 88 (30-32), 3713–3729.

Nicola, L., der Giessen, E. V., Needleman, A., 2003. Discrete dislocation analysis of size effects in thin films. Journal of Applied Physics 93 (10), 5920–5928.

Nicola, L., Xiang, Y., Vlassak, J., der Giessen, E. V., Needleman, A., 2006. Plastic deformation of freestanding thin films: Experiments and modeling. Journal of the Mechanics and Physics of Solids 54 (10), 2089 – 2110.

Nix, W., Gao, H., 1998. Indentation size effects in crystalline materials: A law for strain gradient plasticity. Journal of the Mechanics and Physics of Solids 46 (3), 411–425.

Persson, B., 2006. Contact mechanics for randomly rough surfaces. Surf. Sci. Rep. 61 (4), 201–227.

Persson, B. N., 2001a. Theory of rubber friction and contact mechanics. The Journal of Chemical Physics 115 (8), 3840–3861.

Persson, B. N. J., Aug 2001b. Elastoplastic contact between randomly rough surfaces. Phys. Rev. Lett. 87, 116101.

Plouraboué, F., Boehm, M., 1999. Multi-scale roughness transfer in cold metal rolling. Tribology International 32 (1), 45 – 57.

Song, H., Vakis, A., Liu, X., der Giessen, E. V., 2017. Statistical model of rough surface contact accounting for size-dependent plasticity and asperity interaction. Journal of the Mechanics and Physics of Solids 106 (Supplement C), 1 – 14.

van der Giessen, E., Needleman, A., 1995. Discrete dislocation plasticity: a simple planar model. Modelling and Simulation in Materials Science and Engineering 3 (5), 689.

Venugopalan, S., Nicola, L., 2019. Indentation of a plastically deforming metal crystal with a self-affine rigid surface: A dislocation dynamics study. Acta Materialia 165, 709 – 721.

Venugopalan, S. P., Müser, M. H., Nicola, L., 2017a. Green's function molecular dynamics meets discrete dislocation plasticity. Modelling and Simulation in Materials Science and Engineering 25 (6), 065018.

Venugopalan, S. P., Nicola, L., Müser, M. H., 2017b. Green's function molecular dynamics: including finite heights, shear, and body fields. Modelling and Simulation in Materials Science and Engineering 25 (3), 034001.

Volkert, C. A., Lilleodden, E. T., 2006. Size effects in the deformation of sub-micron au columns. Philosophical Magazine 86 (33-35), 5567–5579.

Wang, A., Müser, M. H., Jun 2017. Gauging persson theory on adhesion. Tribology Letters 65 (3), 103.

6

SUMMARY AND CONCLUSIONS

The primary objective of this work is to gain a better understanding of the plastic behavior of rough metal surfaces under contact loading. Attention in this thesis focuses on the study of self-affine asperities with wavelengths spanning several decades of length scales ranging from micrometers to nanometers, a scale at which plasticity is known to be size dependent. The self-affine rigid indenter is used to indent the plastic crystal of finite height.

In order to study contact mechanics of self-affine metal surfaces involving size - dependent plastic deformation, a new modeling technique is presented that combines discrete dislocation plasticity (DDP) with Green's function molecular dynamics (GFMD). GFMD is a boundary value method that enables one to study the elastic response of a body subjected to an external load by modeling only the surface. The stresses inside the body are derived through analytical solutions. In DDP, plasticity is modeled as the collective motions of discrete dislocations, which are modeled as line singularities in an isotropic linear elastic medium. The dislocation dynamics are governed by a set of constitutive laws.

In Chapter 2, The GFMD method is extended in several ways: shear is added to the GFMD continuum formulation and Poisson numbers as well as the heights of the de-

formed body can now be chosen at will. In addition, the full stress tensor inside the deformed body is derived. The results are validated with calculations based on the finite-element method (FEM) and full molecular dynamics simulations. For the investigated systems we observe a significant speed-up of GFMD compared to FEM. This paved way to studying complicated contact mechanical problems at relatively inexpensive compute power.

In Chapter 3, The GFMD method is further extended to study arbitrary boundary conditions at both the top and bottom surfaces of the layer. This allowed for computing the image stresses necessary for the evolution of dislocation structure. GFMD is successfully combined with DDP and the resulting method is named Green's function dislocation dynamics (GFDD). The new method is used to capture plasticity quantitatively from single to many dislocations. The results obtained using GFDD are compared with conventional DDP for a benchmark problem: periodic indentation of a single crystal by flat punches. The mean contact pressure during indentation using the two methods is found to differ less than two different realizations using the same method. In addition, GFDD is shown to scale more favorably with system size than conventional methods.

In Chapter 4, simulations are performed using GFDD to investigate the indentation of a metal single crystal by means of a self-affine rigid surface. The method provides an accurate description of plasticity by accounting for the collective glide of discrete dislocations as well as a detailed description of the self-affine roughness. The simulations keep track of the changing contact area, the roughening of the metal surface, the pressure distribution, and of sub-surface plastic deformation.

Results show that the plastic response of the metal crystal upon self-affine indentation is size-dependent. Thicker crystals indented deeper by surfaces with larger dimensions deform plastically more than smaller systems, for which dislocation nucleation is source limited.

At a given interference, the interfacial separation in case of plastic crystal is smaller than that of the corresponding elastic crystal due to material pile up from exiting dislocations. This results in the surface of the plastic crystal conforming more to the indenter and hence a better closure of the gap. Despite the smaller interfacial separation in plastic crystals, the contact area is found to be smaller in case of plastic crystal in comparison to the elastic counterpart.

The rms height is an important length in contact problems involving plasticity. Choosing a larger rms height for the indenter induces a larger deviatoric stress component in the substrate and hence strong plasticity. Although for elastic crystals the resistance to indentation increases with Hurst exponent, plasticity is marginally affected by H.

Indentation to an interference of 50 nm for various values of the fractal discretization has indicated that although the actual contact area decreases with decreasing fractal discretization, the nominal contact pressure is constant below a threshold value for λ_s. It is shown that below that value, due to elastic interaction, the fragmented contact area acts as a continuous effective contact, whose length does not change with further decreasing true contact area and which causes a constant subsurface stress distribution. We conclude that if one is interested in either nominal or mean contact pressure, for either elastic or plastic contacts, it is not worthwhile to describe the surface with wavelengths below the threshold. On the contrary, when one is interested in real contact area, contact traction distribution, or gap geometry, the surface must be described with great accuracy, including the shortest wavelength present in the self-affine surface under study.

The mean contact pressure or contact hardness at 20 nm is found to be significantly larger than in previous plasticity studies, up to 35 σ_Y, for the threshold value $\lambda_s = 625$ nm. This difference with previous work is caused partly by dislocation source limitation and partly by the fact that we here considered a finer fractal discretization.

In Chapter 5, we have shown a comparison between dislocation dynamics simulations and Persson's theory in the study of indentation of a metal flat body by a rigid indenter with self-affine roughness. Although there is good agreement between simulations and theory when the metal behaves elastically, the agreement ceases to be good when there is plasticity. The best agreement for the area–load curves is found for small values of the rms height, when the response is almost size independent. With decreasing rms height the onset of plasticity in dislocation dynamics simulations is delayed, because there are only few dislocation sources in the subsurface region where the stress concentration is sufficiently large to induce dislocation nucleation. A good agreement between the area–load curves obtained through simulations and theory is obtained if the size independent yield stress in the theory is replaced by the yield strength obtained through the simulations. The yield strength obtained through the simulations depends

very strongly on rms height, and on the resolution.

The necessity of using a resolution-dependent yield stress in his plasticity theory was already explicitly mentioned by Persson. The fix is indeed important, because the plastic response depends on resolution. However, if one wants to believe the simulations (of course we are well aware that they have limitations too, one being that they are two dimensional), the fix is not sufficient. This is because it does not account for the plasticity size dependence that is observed when the system of analysis is scaled such as to become elastically equivalent. To account for this the yield stress should also become dependent on a scaling length in the problem.

Another point that is important to consider is that, although we found good agreement for area–load curves, when using Persson's theory with the yield strength obtained through dislocation dynamics (i.e. a yield strength that depends on rms height and resolution) the contact stress probability distribution is still markedly different. The simulations predict a much broader contact stress distribution compared with the theory. This is because in the theory the material behaves as perfectly plastic, without any strain hardening. A possible improvement of the theory might be to use, instead of a constant yield strength, a yield strength that increases with plastic deformation. This would translate in a plastic peak in the probability distribution that moves towards larger pressures with increasing closure of the contact and a broader distribution in stresses of the elastic part of the contact.

SAMENVATTING EN CONCLUSIES

Het primaire doel van dit werk is om een beter begrip te krijgen van het plastische gedrag van ruwe metalen oppervlakken in mechanisch contact. De aandacht in dit proefschrift concentreert zich op de studie van zelfgelijkende oneffenheden met golflengtes verspreid over verschillende decades van lengteschalen variërend van micrometers tot nanometers, een schaal waarvan bekend is dat plasticiteit maatafhankelijk is. De zelfgelijkende stijve indringer wordt gebruikt om het plastische kristal van eindige hoogte in te duwen.

Om de contactmechanica van zelfgelijkende metaaloppervlakken met afmeting-afhankelijke plastische vervorming te bestuderen, wordt een nieuwe modelleringstechniek gepresenteerd die discrete-dislocatie-plasticiteit (DDP) combineert met Green's functie moleculaire dynamica (GFMD). GFMD is een grenswaarde methode die het mogelijk maakt om de elastische respons van een lichaam onderworpen aan een externe belasting te bestuderen door alleen het oppervlak te modelleren. De spanningen in het lichaam worden afgeleid door middel van analytische oplossingen. In DDP wordt plasticiteit gemodelleerd als de collectieve bewegingen van discrete dislocaties, die gemodelleerd zijn als lijn-singulariteiten in een isotroop lineair elastisch medium. De dislocatie dynamica wordt bepaald door een reeks constitutieve wetten.

In hoofdstuk 2, wordt de GFMD-methode op verschillende manieren uitgebreid: af-schuiving wordt toegevoegd aan de GFMD-continuumformulering en Poisson-getallen en de hoogtes van het vervormde lichaam kunnen nu naar believen worden gekozen. Bovendien wordt de volledige spanningstensor binnen het vervormde lichaam afgeleid. De resultaten worden gevalideerd met berekeningen op basis van de eindige elementen methode (EEM) en simulaties van volledige moleculaire dynamica. Voor de onderzochte systemen zien we een aanzienlijke versnelling van GFMD ten opzichte van EEM. Dit heeft de weg geplaveid om gecompliceerde mechanische contactproblemen te bestuderen met relatief goedkope rekenkracht.

In hoofdstuk 3 wordt de GFMD-methode verder uitgebreid om willekeurige rand-

voorwaarden te bestuderen aan zowel de boven- als onderkant van de laag. Dit maakt het mogelijk om de beeldspanningen te berekenen die nodig zijn voor de evolutie van de dislocatiestructuur. GFMD is succesvol gecombineerd met DDP en de resulterende methode heet Green's functie dislocatiedynamica (GFDD). De nieuwe methode wordt gebruikt om de plasticiteit kwantitatief te bepalen van enkele tot vele dislocaties. De resultaten die zijn verkregen met behulp van GFDD worden vergeleken met conventionele DDP voor een referentieprobleem: periodieke indrukking van een enkel kristal door platte stempels. De gemiddelde contactdruk tijdens het indenteren met behulp van de twee methoden blijkt minder te verschillen dan die voor twee verschillende realisaties. Bovendien is aangetoond dat GFDD gunstiger schaalt met de systeemgrootte dan de conventionele methodes.

In hoofdstuk 4 worden simulaties uitgevoerd met behulp van GFDD om de indeuking van een enkel metalen kristal door middel van een zelfgelijkend rigide oppervlak to onderzoeken. De methode biedt een nauwkeurige beschrijving van de plasticiteit door rekening te houden met het collectieve glijden van discrete dislocaties en geeft een gedetailleerde beschrijving van de zelfgelijkende ruwheid. De simulaties houden het veranderende contactoppervlak, het opruwen van het metalen oppervlak, de veranderende drukverdeling en de plastische vervorming onder het oppervlak bij.

De resultaten tonen aan dat de plastische respons van het metaalkristal na indrukken met een zelfgelijkende indenter afhankelijk is van de grootte. Dikkere kristallen die dieper ingedrukt zijn door oppervlakken met grotere afmetingen vervormen plastisch meer dan kleinere systemen, waarvoor dislocatiekiemvorming bronbeperkt is.

Bij een gegeven interferentie is de separatie aan het grensvlak in het geval van een plastische kristal kleiner dan die van het corresponderende elastische kristal als gevolg van materiaal dat opstapelt door uitgaande dislocaties. Dit resulteert erin dat het oppervlak van het plastische kristal meer overeenkomt met de indenter en dus een betere afsluiting biedt van de opening. Ondanks de kleinere separatie aan het grensvlak in plastische kristallen, blijkt het contactgebied kleiner te zijn in vergelijking met de elastische tegenhanger.

De rms-hoogte is een belangrijke lengte bij contactproblemen met plasticiteit. Het kiezen van een grotere rms-hoogte voor de indenter geeft een grotere deviatorische spanningcomponent in het substraat en derhalve sterke plasticiteit. Hoewel voor elastische

kristallen de weerstand tegen indrukken toeneemt met de Hurst exponent, wordt de plasticiteit marginaal beïnvloed door H.

Indrukken tot een interferentie van 50 nm voor verschillende waardes van de fractale discretisatie heeft aangetoond dat hoewel het feitelijke contactgebied afneemt met afnemende fractale discretisatie, de nominale contactdruk constant is onder een drempelwaarde voor λ_s. Aangetoond wordt dat onder die waarde, vanwege elastische interactie, het gefragmenteerde contactgebied fungeert als een continu effectief contact, waarvan de lengte niet verandert met een verder afnemend echt contactoppervlak en die een constante ondergrondse spanningsverdeling veroorzaakt. We concluderen dat als men geïnteresseerd is in de nominale of gemiddelde contactdruk, voor zowel elastische als plastische contacten, het niet de moeite waard is om het oppervlak met golflengten onder de drempelwaarde te beschrijven. Integendeel, wanneer iemand geïnteresseerd is in het echte contactgebied, de contact-tractieverdeling of de spleetgeometrie, het oppervlak met grote nauwkeurigheid moet worden beschreven, inclusief de kortste golflengte die aanwezig is in het zelfgelijkende oppervlak dat wordt bestudeerd.

De gemiddelde contactdruk of contacthardheid bij 20 nm blijkt aanzienlijk groter te zijn dan in eerdere plasticiteitsstudies; tot 35 σ_Y voor de drempelwaarde $\lambda_s = 625$ nm. Dit verschil met eerder werk wordt deels veroorzaakt door beperking van de dislocatiebron en deels door het feit dat we hier een fijnere fractale discretisatie beschouwden.

In hoofdstuk 5, laten we vergelijking zien tussen dislocatiedynamica-simulaties en de theorie van Persson met betrekking tot de studie van indrukking van een plat metalen lichaam door een starre indenter met zelfgelijkende ruwheid. Hoewel er een goede overeenstemming is tussen simulaties en theorie wanneer het metaal zich elastisch gedraagt, is de overeenkomst niet langer goed wanneer er sprake is van plasticiteit. De beste overeenkomst tussed de oppervlakte-belastingscurves wordt gevonden voor kleine waardes van de rms-hoogte, waarvoor de respons bijna maatonafhankelijk is. Met afnemende rms-hoogte wordt het begin van plasticiteit in dislocatiedynamica-simulaties vertraagd, omdat er slechts weinig dislocatiebronnen zijn in het gebied onder de oppervlakte waar de spanningsconcentratie voldoende groot is om dislocatiekiemvorming te induceren. Een goede overeen- komst tussen de oppervlakte-belastingscurves verkregen door simulaties en theorie wordt verkregen als de grootte-onafhankelijke vloeispanning in de theorie wordt vervangen door de vloeigrens verkregen door de simulaties. De vloeigrens

verkregen door de simulaties hangt zeer sterk af van de rms-hoogte en van de resolutie.

De noodzaak om een resolutieafhankelijke vloeispanning te gebruiken in zijn plasticiteitstheorie, werd door Persson al expliciet genoemd. De oplossing is inderdaad belangrijk, omdat de plastische respons afhangt van de resolutie. Als je echter de simulaties wilt geloven (natuurlijk zijn we ons ervan bewust dat ze ook beperkingen hebben, waaronder ervan dat ze tweedimensionaal zijn), is deze oplossing niet voldoende. Dit komt omdat het niet de afmetingsafhankelijkheid van de plastiteit verklaart die wordt waargenomen wanneer het analysesysteem zodanig wordt geschaald dat het elastisch equivalent wordt. Om dit te verklaren moet de vloeispanning ook afhankelijk worden van een schaallengte in het probleem.

Een ander punt dat belangrijk is om te overwegen is dat, hoewel we een goede overeenkomst voor oppervlakte-belastingscurves vonden, wanneer we de theorie van Persson gebruiken met de vloeigrens verkregen door dislocatiedynamica (dat wil zeggen een vloeisterkte die afhangt van de rms-hoogte en resolutie) de waarschijnlijkheidsverdeling va de contactspanning nog steeds aanzienlijk anders is. De simulaties voorspellen een veel bredere contactspanningsverdeling vergeleken met de theorie. Dit komt doordat het materiaal zich in de theorie gedraagt als perfect plastisch, zonder enige vervormingsverharding. Een mogelijke verbetering van de theorie zou kunnen zijn om in plaats van een constante vloeigrens een vloeigrens te gebruiken die toeneemt met plastische vervorming. Dit zou zich vertalen in een plastische piek in de waarschijnlijkheidsverdeling die zich naar grotere drukken verplaatst met toenemende sluiting van het contact en een bredere verdeling in spanningen van het elastische deel van het contact.

A

LATERAL-NORMAL DISPLACEMENT COUPLING

It was shown in (Venugopalan et al., 2017) that assuming an in-plane undulation of the top surface of an isotropic layer with a real-valued wavenumber q, equation (3.9) can be solved with the factorization

$$u_\alpha(x, z) = u_\alpha^0 \exp(iqx) \exp(\pm qz). \tag{A.1}$$

Substituting equation (A.1) in the equilibrium condition (3.9), it can be rewritten in Fourier space as

$$\begin{aligned} C_{11}\tilde{u}_x(q, z) - C_{44}\tilde{u}_x(q, z) - i(C_{12} + C_{44})\tilde{u}_z(q, z) &= 0 \\ C_{11}\tilde{u}_z(q, z) - C_{44}\tilde{u}_z(q, z) - i(C_{12} + C_{44})\tilde{u}_x(q, z) &= 0. \end{aligned} \tag{A.2}$$

Equation (A.2) then reduces to

$$\tilde{u}_x(q, z) = i\,\tilde{u}_z(q, z). \tag{A.3}$$

This implies that

$$\tilde{u}_x^c(q, z) - i\tilde{u}_x^s(q, z) = i\tilde{u}_z^c(q, z) + \tilde{u}_z^s(q, z). \tag{A.4}$$

This explains how the solutions of the in-plane cosine transform of the lateral u_x displacement field couples to the in-plane sine transform of the normal u_z displacement, and vice versa.

REFERENCES

Venugopalan, S. P., Nicola, L., Müser, M. H., 2017. Green's function molecular dynamics: including finite heights, shear, and body fields. Modelling and Simulation in Materials Science and Engineering 25 (3), 034001.

B

ASYMPTOTIC ANALYSIS

For the limiting case in which the height of the slab tends to infinity, $H(q, z_{\mathrm{m}})$ can be written as:

$$
\begin{aligned}
H_{11}(q z_{\mathrm{m}} \gg 1) = H_{33}(q z_{\mathrm{m}} \gg 1) &= \tfrac{2s}{1+s}, \\
-\quad H_{12}(q z_{\mathrm{m}} \gg 1) = H_{34}(q z_{\mathrm{m}} \gg 1) &= \tfrac{2s^2}{1+s}, \\
H_{13}(q z_{\mathrm{m}} \gg 1) &= 0, \\
-\quad H_{14}(q z_{\mathrm{m}} \gg 1) = H_{23}(q z_{\mathrm{m}} \gg 1) &= 0, \\
H_{22}(q z_{\mathrm{m}} \gg 1) = H_{44}(q z_{\mathrm{m}} \gg 1) &= \tfrac{2s}{1+s}, \\
H_{24}(q z_{\mathrm{m}} \gg 1) &= 0.
\end{aligned}
\tag{B.1}
$$

In the limiting case of short wave-numbers, we find

$$
\begin{aligned}
q H_{11}(q z_{\mathrm{m}} \ll 1) = q H_{33}(q z_{\mathrm{m}} \ll 1) &= \tfrac{C_{44}}{z_{\mathrm{m}}}, \\
-\quad q H_{12}(q z_{\mathrm{m}} \ll 1) = q H_{34}(q z_{\mathrm{m}} \ll 1) &= 0, \\
q H_{13}(q z_{\mathrm{m}} \ll 1) &= -\tfrac{C_{44}}{z_{\mathrm{m}}}, \\
-\quad q H_{14}(q z_{\mathrm{m}} \ll 1) = q H_{23}(q z_{\mathrm{m}} \ll 1) &= 0, \\
q H_{22}(q z_{\mathrm{m}} \ll 1) = q H_{44}(q z_{\mathrm{m}} \ll 1) &= \tfrac{C_{11}}{z_{\mathrm{m}}}, \\
q H_{24}(q z_{\mathrm{m}} \ll 1) &= -\tfrac{C_{11}}{z_{\mathrm{m}}}.
\end{aligned}
\tag{B.2}
$$

In the case of bottom undulation going to zero $\boldsymbol{u}(q, 0) \to 0$, we recover the elastic energy for a fixed bottom derived in (Venugopalan et al., 2017).

REFERENCES

Venugopalan, S. P., Nicola, L., Müser, M. H., 2017. Green's function molecular dynamics: including finite heights, shear, and body fields. Modelling and Simulation in Materials Science and Engineering 25 (3), 034001.

C

PSEUDOCODE: GREEN'S FUNCTION DISLOCATION DYNAMICS

The following notations are adopted to outline GFDD methodology.

ζ: Dislocation structure,

S_t, S_u: Part of the boundary where traction and displacement are prescribed respectively,

$\tilde{\boldsymbol{\sigma}}$, $\tilde{\boldsymbol{u}}$: Stress and displacement field due to dislocations in the solid,

$\hat{\boldsymbol{\sigma}}$, $\hat{\boldsymbol{u}}$: Stress, displacement field of the complementary problem,

$\boldsymbol{\sigma}$, $\boldsymbol{u}$: Total stress and displacement field in the solid,

$\tilde{\boldsymbol{t}}$, $\tilde{\boldsymbol{u}}$: Tractions and displacements on S_t, S_u due to dislocation fields,

$\hat{\boldsymbol{t}}$, $\hat{\boldsymbol{u}}$: Tractions and displacements on S_t, S_u for complementary problem,

$\boldsymbol{t}$, $\boldsymbol{u}$: Prescribed tractions and displacements on S_t, S_u for the total problem,

where $\boldsymbol{\sigma} = \sigma_{ij}\boldsymbol{e}_{ij}$, $\boldsymbol{t} = t_i\boldsymbol{e}_i$ and $\boldsymbol{u} = u_i\boldsymbol{e}_i$ with $\boldsymbol{e}_{ij} = \boldsymbol{e}_i \otimes \boldsymbol{e}_j$ where $\boldsymbol{e}_i$ and $\boldsymbol{e}_j$ are the unit basis vectors in $\mathbb{R}^2$.

The quantities available at time t_n are: $\zeta_n, \hat{\boldsymbol{\sigma}}_n, \hat{\boldsymbol{u}}_n, \tilde{\boldsymbol{\sigma}}_n$ and $\tilde{\boldsymbol{u}}_n$.

Objective of GFDD simulation is to find: $\zeta_{n+1}, \tilde{\boldsymbol{\sigma}}_{n+1}, \tilde{\boldsymbol{u}}_{n+1}, \hat{\boldsymbol{\sigma}}_{n+1}$ and $\hat{\boldsymbol{u}}_{n+1}$ at time t_{n+1}.

Step1: Let the prescribed traction on S_t increase as $\boldsymbol{t} = K\boldsymbol{t}^0$, where K is a function of time and $\boldsymbol{t}^0$ be a specified reference traction field. Also, let the prescribed displacement on portion S_u vary with time in a similar manner so that $\boldsymbol{u} = K\boldsymbol{u}^0$, where $\boldsymbol{u}^0$ be a specified reference displacement field. Thus, at time t_{n+1}: $K_{n+1} = K(t_{n+1})$.

Step2: Update the dislocation structure, $\zeta_{n+1} = f(\zeta_n, \tilde{\boldsymbol{\sigma}}_n)$. The steps involved in this process are summarized below.

– Find stresses on dislocation due to $\tilde{\boldsymbol{\sigma}}$ and $\hat{\boldsymbol{\sigma}}$; Peach-Koehler forces on dislocations, velocity of dislocations.

– Check for release of dislocations pinned to obstacles.

– Move dislocations to new positions.

– Annihilation of dislocations.

– Pinning of dislocations to obstacles.

– Nucleation of dislocations at sources

Step3:

– Get tractions $\tilde{\boldsymbol{t}}_{n+1}$ acting on portion S_t of boundary arising because of dislocations:

$$\tilde{\boldsymbol{t}}_{n+1} = \tilde{\boldsymbol{\sigma}}_{n+1} \boldsymbol{n}, \qquad (C.1)$$

where $\boldsymbol{n}$ is the unit normal vector to the boundary.

– Get the updated specified traction for the complementary problem at t_{n+1}:

$$\hat{\boldsymbol{t}}_{n+1} = K_{n+1} \boldsymbol{t}^0 - \tilde{\boldsymbol{t}}_{n+1}. \qquad (C.2)$$

Step4:

– Find displacements $\tilde{\boldsymbol{u}}_{n+1}$ on portion S_u of boundary due to dislocations.

– Get the updated specified displacement for the complementary problem at t_{n+1}:

$$\hat{\boldsymbol{u}}_{n+1} = K_{n+1} \boldsymbol{u}^0 - \tilde{\boldsymbol{u}}_{n+1}. \qquad (C.3)$$

Step5: Start solving the complementary problem using GFMD.

– Set up a rigid top punch represented by $h^{\text{top}}(\boldsymbol{r})$.

– The elastic bottom solid with arbitrary surface profile $h^{\text{bot}}(\boldsymbol{r})$ is represented using nx equispaced (super-)atoms.

– The center of mass of the system is critically damped or slightly under-damped.

– Loop over time. Set the number of iterations n_{it} such that it scales with $\sqrt{\left(\frac{z_m}{L_x}\right) nx}$.

  – Transform displacements $\hat{\boldsymbol{u}}_{n+1}$ on portion S_u of the boundary into Fourier space represented as $\bar{u}_i^{\text{now}}(\boldsymbol{q})$.

  – Transform tractions $\tilde{\boldsymbol{t}}_{n+1}$ on portion S_t of the boundary into Fourier space represented as $\bar{t}_i(\boldsymbol{q})$.

  – Calculate elastic restoring forces, $\bar{F}_i(\boldsymbol{q}) = -(\nabla_{u_i} v_{\text{el}}) \bar{u}_i^{\text{now}}(\boldsymbol{q})$.

  – Correct the traction due to dislocations, $\bar{F}_i(\boldsymbol{q}) \leftarrow \bar{F}_i(\boldsymbol{q}) + \bar{t}_i(\boldsymbol{q})$.

- Add external pressure, $\bar{F}_i(0) \leftarrow \bar{F}_i(0) + P_i^{\text{ext}}$.

- Add damping forces, $\bar{F}_i(\boldsymbol{q}) \leftarrow \bar{F}_i(\boldsymbol{q}) + \eta\{\bar{u}_i^{\text{now}}(\boldsymbol{q}) - \bar{u}_i^{\text{old}}(\boldsymbol{q})\}$.

- Use Verlet to solve equation of motion, $\bar{u}_i^{\text{new}}(\boldsymbol{q}) = 2\bar{u}_i^{\text{now}}(\boldsymbol{q}) - \bar{u}_i^{\text{old}}(\boldsymbol{q}) + \bar{F}_i(\boldsymbol{q})\mathrm{d}t^2$.

- Transform displacements into real space.

- Implement the boundary condition at the punch-substrate interface:

    i If the interface is frictionless then skip this step.

    ii If the interface is full sticking then implement hard wall condition written as $\bar{u}_i^{\text{new}}(\boldsymbol{r}) \leftarrow \max\{\bar{u}_i^{\text{new}}(\boldsymbol{r}), -h^{\text{top}}(\boldsymbol{r})\}$.

- Assign $\bar{u}_i^{\text{old}}(\boldsymbol{r}) \leftarrow \bar{u}_i^{\text{now}}(\boldsymbol{r})$ & $\bar{u}_i^{\text{now}}(\boldsymbol{r}) \leftarrow \bar{u}_i^{\text{new}}(\boldsymbol{r})$.

– Output the displacement $\bar{u}_i(\boldsymbol{r})$ corresponding to the equilibrated surface at the end of MD iterations.

Step6: The displacement field of the equilibrated surface obtained using GFMD from the previous step is used to calculate the body fields. We had derived the closed-form expressions for calculating body fields earlier in B.

Step7:

– If required, output total stresses, strains and displacements:

$$\boldsymbol{\sigma}_{\text{n+1}} = \hat{\boldsymbol{\sigma}}_{\text{n+1}} + \tilde{\boldsymbol{\sigma}}_{\text{n+1}}, \tag{C.4}$$

$$\boldsymbol{\epsilon}_{\text{n+1}} = \hat{\boldsymbol{\epsilon}}_{\text{n+1}} + \tilde{\boldsymbol{\epsilon}}_{\text{n+1}}. \tag{C.5}$$

$$\boldsymbol{u}_{\text{n+1}} = \hat{\boldsymbol{u}}_{\text{n+1}} + \tilde{\boldsymbol{u}}_{\text{n+1}}. \tag{C.6}$$

Curriculum Vitæ

Syam PARAYIL VENUGOPALAN

27-10-1988   Born in Palakkad, Kerala, India.

AWARDS

2013   J.C. Bose Fellowship, Indian Institute of Science Bangalore, India (Grant no. DSTO977)

2013   M.E silver medalist, Indian Institute of Science Bangalore, India

2011   Ministry of Human Resource Development scholarship, India

2011   Graduate Aptitude Test in Engineering: All India Rank 22

2010   B.Tech silver medalist with honors and distinction, University of Calicut with 30+ engineering colleges

EDUCATION & WORK EXPERIENCE

2018–Present   Research Scientist at ASML Veldhoven, Netherlands
Physical modeling of plasma etching for semiconductor fabrication

2014–2018   PhD. in Computational Material Science
Faculty of Mechanical, Maritime and Materials Engineering
Delft University of Technology, The Netherlands
PhD Thesis: Plastic deformation of self-affine rough metal surfaces under contact loading
Promotor: Prof. dr. L. Nicola

Spring 2017   Course Instructor
Finite Element Method, Mechanical Behavior of Materials

2016–2017   Daily Supervisor for two Masters Theses
Masters Thesis: Contact between rough surfaces: A Green's function molecular dynamics approach, Steven Jan van Dokkum
Masters Thesis: Three-Dimensional Green's function molecular dynamics for solids with generic elastic properties, Yaswanth Murugesan

2013–2014   Senior Research Fellow, JC Bose Fellowship,
Computational Solid Mechanics lab,
Indian Institute of Science, Bangalore, India

2011–2013   M.E. in Mechanical Engineering
Indian Institute of Science, Bangalore, India

2010–2011   Lecturer in Mechanical Engineering
University of Calicut, India

2006–2010   B.Tech in Mechanical Engineering
University of Calicut, India

LIST OF PUBLICATIONS

- **Syam P Venugopalan, Lucia Nicola and Martin H Müser**, *Green's function molecular dynamics: including finite heights, shear, and body fields*, Modelling and Simulation in Materials Science and Engineering **25**, 034001 (2017).

- **Syam P Venugopalan, Martin H Müser and Lucia Nicola**, *Green's function molecular dynamics meets discrete dislocation plasticity*, Modelling and Simulation in Materials Science and Engineering **25**, 065018 (2017).

- **Syam P Venugopalan and Lucia Nicola**, *Indentation of a plastically deforming metal crystal with a self-affine rigid surface*, Acta Materialia **165**, 709-721 (2019).

- **Syam P Venugopalan, Nilgoon Irani and Lucia Nicola**, *Plastic contact of self-affine surfaces: Persson's theory versus discrete dislocation plasticity*, submitted.

- **Yaswanth Murugesan, Syam P Venugopalan, Martin H Müser and Lucia Nicola**, *Green's function molecular dynamics to calculate the effect of contact roughness on sub-surface stresses*, to be submitted.

LIST OF CONFERENCES

- **Syam P Venugopalan and Lucia Nicola**, *Contact deformation of self-affine metal surfaces: A Green's function dislocation dynamics approach*, International conference on computational contact mechanics, Lecce, Italy (2017).

- **Syam P Venugopalan and Lucia Nicola**, *Green's function molecular dynamics meets discrete dislocation plasticity*, Physics at Veldhoven, Netherlands (2017).

- **Syam P Venugopalan and Lucia Nicola**, *Modelling randomly rough 1D+1D contact involving finite height elasto-plastic solids*, Future energy conference, Eindhoven, Netherlands (2017).

- **Syam P Venugopalan and Lucia Nicola**, *Novel dislocation dynamics model to study contact deformation of self-affine metal surfaces*, Materials Research Society, Phoenix, Arizona (2017).

- **Syam P Venugopalan and Lucia Nicola**, *Green's function molecular dynamics meets discrete dislocation plasticity*, Dislocations conference, Purdue University, Indiana (2016).

- **Syam P Venugopalan and Lucia Nicola**, *Green's function molecular dynamics meets discrete dislocation plasticity*, European Community on Computational Methods in Applied Sciences and Engineering, Barcelona, Spain (2016).

- **Syam P Venugopalan and Lucia Nicola**, *Plastic deformation of metallic surfaces under contact loading*, Materials Research Society, Boston, Massachussetts (2015).

LIST OF COURSES AND WORKSHOPS

Selected few

- **Introduction to Programming on the GPU with CUDA**, *Computational Science and Engineering*, Delft University of Technology (2017).

- **Data science: Programming with R course**, *Harvard University online course*, (2017).

- **Micro/nano-scale models for tribology workshop**, *Lorentz Research Centre*, Leiden University, Netherlands (2017).

- **Introduction to mathematical thinking**, *Stanford University online course*, (2017).

- **Dislocations course**, *Delft University of Technology*, Netherlands (2016).

- **Long-time scale atomistic simulations in material science**, *Materials Research Society*, Boston, Massachussetts (2015).

- **Modeling materials**, *Engineering of Advanced Materials (EAM) Center of Excellence, Friedrich-Alexander University*, Erlangen-Nürnberg, Germany (2015).

- **Cloud computing with Wolfram Language**, *CANdiensten B.V.*, Amsterdam, Netherlands (2015).

- **Programming in Mathematica**, *CANdiensten B.V.*, Amsterdam, Netherlands (2015).

ACKNOWLEDGEMENTS

It feels like it was just yesterday that I came to Netherlands to start my PhD at TU Delft. Four years flew by in the blink of an eye and here I am writing the acknowledgement of my thesis. I would like to express my thanks to the group of people that made this possible. To begin with, I would like to thank my grandmother Suseelamma and my mother Latha Menon for all the pain and sacrifices they underwent to make me the first person in the family to graduate high school. Little did they imagine that I would go on to submit my PhD thesis. I thank my father Parayil Venugopalan for spending the prime of his life away from the family to serve the country and support the family. Without the three of you, I would not have reached where I am today.

My sincere thanks to Suresh and Sreeni uncle who ignited a logical approach to problem solving in me at a young age. Many thanks to my high school teachers Sri Savari Muthu who promoted my interest in Mathematics, Sri Chandramohan and Smt Lakshmi who nurtured my interest in Science, Prof. P. R. Suresh and Prof D. Prakash who played a crucial role during my Bachelor's degree and finally my Master's supervisor Prof. R. Narasimhan who introduced me to research at IISc Bangalore.

I thank my PhD supervisor and promotor, Prof. Lucia Nicola for giving me an opportunity to work as a PhD scholar at TU Delft. I appreciate her highly critical and perfectionist approach to research. I would also like to thank Prof. Martin Müser for his valuable inputs during the beginning years of my PhD. His contributions were significant for our first paper which was later selected as one of the "Highlights of 2017" of the MSMSE journal.

I express my gratitude to the doctoral defense examination committee consisting of Prof. Marc Fivel, Prof. Andréas Almqvist, Prof. Jilt Sietsma, Prof. Ian Richardson and Dr. Can Ayas. I appreciate your gesture of accepting the invitation and taking time off your schedule to read my thesis and provide valuable feedbacks.

The most memorable moments from my PhD are the various opportunities I got to

meet and personally interact with eminent researchers around the world. I value the discussions I had with Prof. B.N.J. Persson, Prof. Martin Müser, Prof. Erik van der Giessen, Prof. James Greenwood, Prof. Lars Pastewka, Prof. Wei Cai, Prof. Jaffar El-Awady, Prof. Jean-François Molinari, Prof. Andreas Almqvist, Prof. Ellad Tadmor, Prof. Ron Miller, Prof. Marco Paggi and Prof. Derek Warner.

I would also take this opportunity to mention few people who inspired me to keep on striving during the course of my PhD. My music teacher Padmashree Sangeetha Kalacharya Shri Rudrapatnam Thyagarajan from whom I learned the highly meticulous approach towards one's profession. Dr. Jyotsna Srikanth, from whom I learned the art of multitasking. She is a renowned violinist, enterpreneur, producer, medical doctor and on top of all, a mother of two. Dr. Kamala Unnikrishnan from whom I learned that there is no age limit to following one's passion/interest.

If there is one person I need not formally thank it is my wife, but I would rather express my gratitude ;-). Ranjani has been of immense support in the crucial decisions of my life. I am extremely lucky to continue getting her selfless love and support. I also thank her father Dr. Shamasundar Shivaramaiah who is a seasoned enterpreneur and researcher who continues to inspire the young researcher in me. Her mother Geetha Malini is a true inspiration when it comes to organizational skills and multitasking professions. She has been instrumental in promoting my extra-curricular activities involving classical music and philosophy. I wish Seshi Paati had made it to the day I graduate. They all continue to be an aura of positive energy.

I acknowledge the boundless love and care that I received from my brothers Saru and Baju.

A special thanks to Max Risselada and Jenneken Berrends who ensured our stay at Delft is comfortable. Over the years, we have become family.

I can tell for sure that I had the best moments of my life with my fun gang involving Anju, Prazz the dude, Ranju and G! Also, Zombie who replaced the dude later. I will miss you guys for sure.

Thank you, Dr. Prasanth Venugopal and Manjapra Varieth Devina Syamnath for agreeing to be paranymphs on the occasion of my PhD defense. If only I could have more paranymphs I would have been glad to have Arvind Nagarajan and Dr. Venkatesh Seshan on board.

I feel particularly indebted to Sriram and Lakshmi who have helped me during my busy and stressful times during the final years of PhD. Thanks a lot for the amazing food and joyful discussions we shared.

I also acknowledge the addicting Carnatic music sessions I had with the "Café Carnatique" comprising of Dr. Sriram Shankar Rajadurai, Anand Sundaresan, Lakshmi Ashok, Jeyakrishna Sridhar and Ranjani.

I would like to thank my friends who made my stay at Delft memorable: Arun Muraleedharan, Amy and Freddy, Baptiste Synquin, Chandrakantha and Dharm-jeet Gavel, Dr. Gautham Ram Chandramouli and Kamakshi Parwani, Giridharan Krishnamurthy, Jaikishen Rajendran, Lakshminarayanan Nandakumar, Manu Chakkingal, Nandini Muthusubramaniam, Nirupa Raghavan and Bharadwaj Rangarajan, Pramoda and Dr. Yadati Narasimha Karthik, Rama Doshi and Dr. Shivraj Karewar, Dr. Shruthi Krishnan and Dr. Maqsood Ameen, Dr. Vasudevan Lakshminarayanan.

I thank my officemate Dr. Astrid Elzas for the valuable discussions we had over the past four years, also a special thanks for correcting the Dutch summary in this thesis. I also thank other colleagues with whom I had fun discussions: Dr. Fengwei Sun, Jayasree Pan, Dr. Linda Boatema, Max Holicki, Narasimhan Viswanathan, Neha Verma, Dr. Peter Klaver, Raghvendra Pratap Singh, Tarun Katiyar and most importantly my colleague and my former master student Yaswanth Murugesan who I successfully motivated to pursue PhD.

I express my sincere gratitude to Wolfram, Scopus and Google, without you guys my PhD would have taken another decade to complete.

കർമണ്യേവാധികാരസ്തേ മാ ഫലേഷു കദാചന |

മാ കർമഫലഹേതുർഭൂർമാ തേ സങ്ഗഃ അസ്തു അകർമണി ||

कर्मण्येवाधिकारस्ते मा फलेषु कदाचन ।

मा कर्मफलहेतुर्भूर्मा ते संगः अस्तु अकर्मणि ।।

You only have the right to work but never to its fruits |

Let not the fruits of action be your motive, nor let your attachment be to inaction ||

Bhagavad Gita